eXPRESS Polymer Letters Vol.2, No.6 (2008) 391
Available online at www.expresspolymlett.com
DOI: 10.3144/expresspolymlett.2008.46

Editorial corner – a personal view
Polymer systems for solid pharmaceuticals

*Gy. Marosi**

Organic Chemistry and Technology Department of Budapest University of Technology and Economics,
H-1111 Budapest, Műegyetem rkp. 3, Hungary

Macromolecular components of pharmaceuticals represent a segment of small quantity but high value within the polymer market. The knowledge built in these systems acts as driving force for other polymer fields. Their conventional roles, as the coating and bonding, have been extended recently due to new challenges. These challenges include the needs for stabilization and solubilisation of new drug types (the stability and water solubility of which are mostly not satisfactory). Need exists also for influencing the morphology of drugs, for controlling the site and kinetics of their release (e.g. targeted drug delivery) and for meeting the mechanical requirements. The currently increasing productivity means further challenges in many respects such as for film forming materials, for processing machines and for analytical control. On the other hand, the development is strongly limited by the extremely stringent regulation in the field of pharmaceuticals. Under the tension between the increasing challenges and the limited possibilities new concepts and strategies emerged. Composite structure of the corpus (core) of the tablets and of the coating materials, using medically accepted nanofillers of well designed interphases, provide improved strength, transport and drying features. Embedding of the drug molecules in solid macromolecular solutions, amphiphilic polymer micelles (or dendrimers), nanoparticles of mucoadhesive, responsive, targeted surface etc. provide them with enhanced stability, solubility and bioavailability. Controlling the T_g of the polymers, by means of blending or immobilization, increases the chance for controlling the polymorphic stability of the embedded drugs. Rapid development of the extrusion, (and injection molding) techniques can be expected but the current difficulties of cleaning and validation has to be solved. Supercritical methods will develop rapidly as well. Concerning the analyses introduction of new dissolution medium of better similarity to the gastrointestinal fluid is expected, which will influence the polymers to be used. The need for improved control of the composition, structure and molecular mobility of solid pharmaceuticals will enhance the importance of the micro-spectroscopic and Thermally Stimulated Current (TSC) methods, which may help in prediction of the changes of the stability.

Prof. Dr. György Marosi
Member of International Advisory Board

*Corresponding author, e-mail: gmarosi@mail.bme.hu

eXPRESS Polymer Letters Vol.2, No.6 (2008) 392–397
Available online at www.expresspolymlett.com
DOI: 10.3144/expresspolymlett.2008.47

On the influence of nucleation on the toughness of iPP/EPR blends with different rubber molecular architectures

C. Grein, M. Gahleitner*

Borealis Polyolefine GmbH, St. Peter Strasse 25, A-4021 Linz, Austria

Received 26 February 2008; accepted in revised form 6 April 2008

Abstract. The influence of α- and β-nucleating agents on the fracture performance of two different 32 wt% rubber modified isotactic Polypropylene (iPP) reactor blends is discussed as a function of the phase morphology of the investigated systems. Nucleation for systems with a large inter-particle distance was found to have only a limited impact on the temperature at which the ductile-brittle transition occurs, negative for α-nucleated blends, almost negligible for β-nucleated resins. For blends exhibiting a small inter-particular distance between their ethylene-propylene rubber (EPR) phase, toughness was promoted slightly by α-nucleation and to a large extent by β-nucleation as compared to a non-nucleated reference. These findings raise the importance of mechanistic synergies between the rubbery phase and the matrix to maximize the fracture resistance of blends.

Keywords: *polymer blends and alloys, PP/EPR blends, fracture, damage mechanism, nucleation*

1. Introduction

Mechanical properties of semi-crystalline polymers like polypropylene (PP) are mostly determined by their crystalline structure and consequently massively affected by nucleation. For single-phase systems, mostly for isotactic PP homopolymers (iPP), the effect of selective nucleation both of the α-phase [1, 2] and of the β-phase [3, 4] has been studied extensively already. The molecular weight of the respective polymers was found to be the dominating factor for mechanical consequences of nucleation in this case and is valid for a wide range of processing modes from injection molded specimens to vibration welded parts [5].

The respective influence of nucleating agents (α or β) on the mechanical performances of heterophasic systems composed of an iPP matrix and an ethylene-propylene rubber (EPR) is still controversial, consequence of a lack of published experimental data. Whereas several studies have reported positive effects of nucleation on the fracture resistance of iPP/EPR blends [6–12], other contributions showed limited (for β-nucleation) [4, 13–16] or even negative (for α-nucleating agents) ones [4, 17, 18]. The goal of the present investigation was to identify potential coupling effect between the matrix crystalline structure induced by nucleation and the morphology of the rubbery phase in order to clarify this apparent contradiction. Two iPP/EPR reactor blends containing about 32 wt% of dispersed rubber phase were investigated. Their phase morphology was controlled by varying the molecular weight of the in-reactor made elastomer (EPR). One material contained a rubber with low molecular weight, expressed by an intrinsic viscosity (IV) of 1.9 dl/g, the other one had an IV of 4.2 dl/g. The focus was set on the determination of ductile-brittle transitions since standard characterisation methods were found to be insufficient to discriminate the studied grades sufficiently.

*Corresponding author, e-mail: christelle.grein@borealisgroup.com

2. Experimental

2.1. Materials

Two reactor-made iPP/EPR blends produced with a high yield 4th generation Ziegler-Natta-catalyst in a pilot facility from Borealis using multiple reactors were studied. Both grades contained 32 wt% of xylene cold soluble (XCS, approximated to be the EPR content), had a propylene-rich rubber (C3-XCS of about 55 wt%) and exhibited a matrix MFR of about 60 g/10 min. The rubbery phase of material 1, PP-1.9, had an intrinsic viscosity (IV) of 1.9 dl/g, the dispersed phase of its counterpart, PP-4.2, an IV of 4.2 dl/g.

The materials were nucleated with 0.1% of NA11 (Sodium 2,2'-methylene bis-(4,6-di-tert. butylphenyl) phosphate) as α-nucleating agent manufactured by Asahi Denka (resp. distributed by Adeka Palmarole) and 0.1% of proprietary calcium pimelate (CaPim) as β-nucleating agent [19]. Non-nucleated references were also studied. Compounds were made on a TSE24 twin-screw extruder and stabilised with a conventional additive package. The efficiency of the nucleation effect was controlled by DSC (Differential Scanning Calorimetry) using the information of the first cooling and second heating scan of a 10/–10/10°C/min scanning program between 23 and 210°C. Both α-nucleated iPP/EPR blends had thus a crystallisation temperature around 130°C accounting for fully α-nucleated systems; both β-nucleated grades exhibited a crystallisation temperature of about 124°C and a β-phase as from DSC of more than 80% Although we are aware that this DSC-method is not the best one to determine the β-content of iPP blends [20, 21], our experience suggests that the investigated samples are almost completely β-nucleated.

2.2. Experimental techniques

The melt flow rate (MFR) of the investigated grades was measured in accordance to ISO 1133 at a load of 2.16 kg using a temperature of 230°C. Xylene cold soluble (XCS) content was determined according to ISO 6427. The C3 content of the dispersed phase, C3(XCS), was measured according to EN 17025 with FTIR (Fourier Transformations Infrared Spectroscopy) calibrated with ^{13}C-NMR (Nuclear Magnetic Resonance). The intrinsic viscosity (IV) of XCS fraction was assessed by ISO 1628 in decahydronaphthalin at 135°C.

For an overall thermomechanical profile, dynamic mechanical analysis (DMTA) was performed in accordance with ISO 6721 with 50×10×1 mm^3 compression moulded samples, as a function of temperature at 1 Hz with a heating rate of 2 K/min under forced oscillation in a torsion mode (ε = 0.04%) with an RDS II (Rheometrics).

Charpy notched impact strengths (NIS) were measured at 23 and –20°C according to ISO 179/1 eA (test speed of about 3 m/s), flexural elastic moduli were recorded at 23°C according to ISO 178 on 80×10×4 mm^3 specimens at a test speed of 50 mm/min. All the materials were injection moulded under the same standard conditions in line with EN ISO 1873-2. The parts were not conditioned prior to testing, which was done at least 96 h after moulding.

Ductile-brittle transitions were determined on a Charpy Instrumented Pendulum. The energy of the pendulum was fixed and valued 50 J. For data acquisition and data reduction software developed by Borealis was applied. Force-displacement curves were recorded and analysed.

The work to break, G_{tot}, was calculated from Equation (1):

$$G_{tot} = \frac{U_{tot}}{B(W-a)} \tag{1}$$

where U_{tot} is the energy to break of the SENB (Single Edge Notched Bending) specimen, B is the thickness of the sample, W is the width of the sample, a is the crack length of the sample.

While the test speed was maintained constant (1.5 m/s), the temperature T was varied in between –60 and 100°C, in steps of 10 K far from the ductile-brittle transition and steps of 2°C near to it. The transitions were taken to be the inflexion points in the curves $G_{tot} = f(T)$. In this case, the lower the temperature at which the ductile-brittle transition (T_{db}) occurred, the tougher is the material.

Note moreover that the indicated G_{tot} values in the ductile range have to be considered with caution. Since the samples didn't break, only the broken sample width (W_{broken}) involved in the fracture process ($W_{broken} < W$) should have been taken into account in the calculations. The G_{tot} are thus underestimated all the more as the test temperature

increased (W_{broken} decreasing with increasing this latter).

Transmission electron micrographs of PP-1.9 and PP-4.2 were performed on 100 nm ultrathin cuts after staining the specimen with ruthenium tetroxide [22]. The specimens were prepared from the core section of the injection moulded bars.

3. Results and discussion

The dynamic mechanical response of the different systems with an IV of 4.2 dl/g is given in Figure 1; the trends observed are the same for the PP-1.9 blends. While the peak of the rubbery phase is independent of the nucleation, appearing at about –50°C, the glass transition temperature of the iPP matrix is affected to a non negligible extent by the nucleation modified crystalline phase.

Hence, the T_g of the neat system is around 0°C, the T_g of the α-nucleated blend is around 4°C and that of the β-nucleated Impact PP at about 8°C. For this latter, one may notice the specific shape of this relaxation with its sharp coupling with the $T_{\alpha c}$ relaxation at 50°C – which has often been ascribe to promote toughness [23]. For the α-nucleated blend, an increase of 4°C in the T_g – at otherwise similar shape – compared to the neat system is expected to lead to more embrittlment, an expectation which does not hold for all the grades studied as will be shown later on.

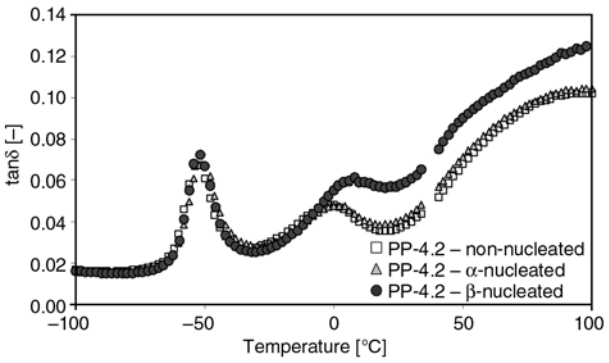

Figure 1. DMTA curves of non-nucleated, α-nucleated and β-nucleated PP-4.2

The particle size of the investigated blends – as highlighted in Figure 2 – is dependent of the intrinsic viscosity of their elastomer phase. As expected PP-1.9 exhibited smaller EPR inclusions than its homologue which had an IV of 4.2. As a consequence, the inter-particle distance (*ID*) of PP-1.9 was smaller to than that of PP-4.2. An estimation of *ID* – assuming the rubber particles to be arranged in a cubic lattice – can be obtained using Equation (2) [24]:

$$ID = d\left[\left(\frac{\pi}{6\Phi}\right)^{\frac{1}{3}} - 1\right] \quad (2)$$

where d is the average particle diameter and Φ is the rubber volume fraction.

Given that PP-1.9 has roughly an inclusion diameter of 400 nm and PP-4.2 roughly one of 1600 nm one obtains *ID*(PP-1.9) ~ 290 nm and *ID*(PP-4.2) ~ 1150 nm, matrix ligaments in between particles are thus approximately 4 times larger in PP-4.2 than in PP-1.9. These calculations have been made for non-nucleated systems. Assumed in the following is that the phase morphology and thus the interparticular distance will not be affected by a nucleation using NA11 or calcium pimelate.

The melt flow rates (MFR), notched impact strengths (NIS) at 23 and –20°C and the *E*-moduli at 23°C are given in Table 1. While the stiffness values prove – in addition to the DSC results – that both nucleation modes were effective, the fracture resistance values are more tricky to interpret because those recorded at 23°C always account for a ductile mode of failure, while those carried out at –20°C stand for a brittle failure mode. The NIS results tend to suggest that the low IV grades show disadvantages in the toughness compared to their higher IV homologues at room temperature as well

Table 1. Melt flow rates (MFR), notched impact strengths (NIS) at 23 and –20°C and *E*-moduli at 23°C of PP-1.9 and PP-4.2 (non-nucleated, α-nucleated, β-nucleated)

	MFR [g/10 min]	NIS(23°C) [kJ/m²]	NIS(–20°C) [kJ/m²]	E_{flex} [MPa]
PP-1.9	21.2	26.3 ± 3.1	5.3 ± 0.3	742 ± 10
PP-1.9 + 0.1% NA11	21.2	33.0 ± 0.9	6.3 ± 0.3	940 ± 11
PP-1.9 + 0.1% CaPim	21.5	43.9 ± 1.4	6.7 ± 0.3	591 ± 5
PP-4.2	6.6	72.7 ± 1.7	14.1 ± 0.7	682 ± 6
PP-4.2 + 0.1% NA11	6.6	44.7 ± 16	12.7 ± 0.6	816 ± 6
PP-4.2 + 0.1% CaPim	6.8	69.8 ± 1.2	16.4 ± 0.8	594 ± 2

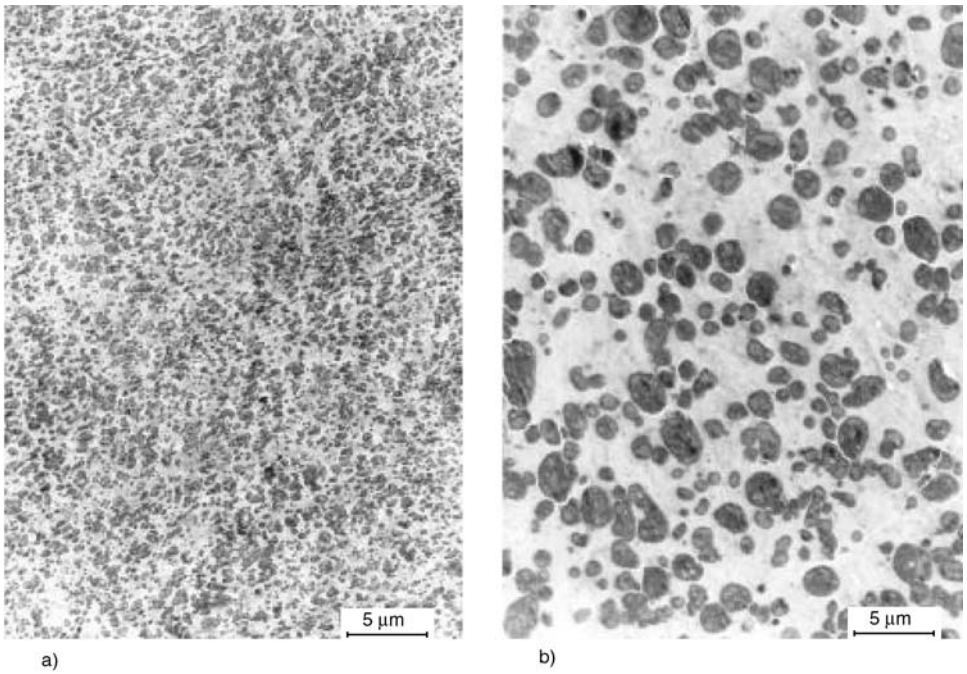

Figure 2. 42.8×31.4 µm micrographs of PP-1.9 (a) and PP-4.2 (b). RuO_4 stained thin cuts; transmission electron micrographs.

at refrigerator temperature for all the different nucleation configurations. The relativity of this interpretation will be show subsequently.

Indeed, the values obtained under standard conditions often do not reflect (and can thus not predict) the behaviour of a material over the entire relevant loading range. This feature was once more confirmed with our experiments. Figures 3 and 4 provide a deeper insight into the mechanical performance of the studied grades and demonstrate that differences between non-nucleated and nucleated grades are more pronounced for the blend with a low IV.

This conclusion is particularly true for the β-nucleated grades where at ductile-brittle transition shift of about 26°C towards lower temperature is observed with the PP-1.9 series between the neat grades and the β-nucleated resins. A synergistic combination of a small ligament length and intrinsic high ductility of the β-phase is here obvious. In fact, matrix shearing – which is believed to be the predominant damage form once the deformation initiated – is used to its full potential when the stress-fields of the particles are close enough and can overlap and is promoted by the intrinsic high mobility of the β-phase, a direct consequence of its specific microstructure in terms of lower packing density and favourable lamellar arrangement [25–27]. A confirmation of the crucial role of the

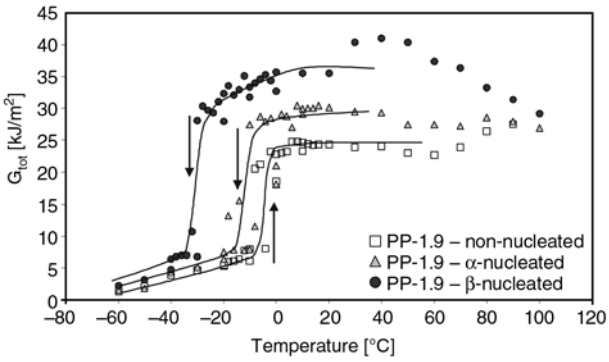

Figure 3. Work to break, G_{tot}, plotted against temperature. Instrumented Charpy Pendulum. Test speed: 1.5 m/s. iPP/EPR blends with rubber IV of 1.9 dl/g. The arrows represent the temperatures at which the ductile-brittle transitions occurred.

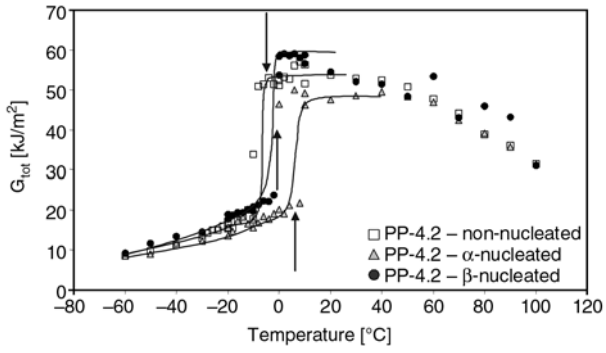

Figure 4. Work to break, G_{tot}, plotted against temperature. Instrumented Charpy Pendulum. Test speed: 1.5 m/s. iPP/EPR blends with rubber IV of 4.2 dl/g. The arrows represent the temperatures at which the ductile-brittle transitions occurred.

distance between particles is provided by the β-modified PP-4.2 for which the fracture resistance behaviour is similar to the non-nucleated system. Here, the matrix ligament length is seemingly too wide to allow an effective stress transfer from the rubbery phase to the matrix and thus an effective use of the ductility of the β-phase.

Comparing the α-nucleated grades among them is also instructive from a mechanistic point of view. For the low IV series, the non-nucleated material is outperformed by the α-nucleated one. As no hint about an induced change of the particle size of both systems was given, such a result suggests that superstructure effects (like a smaller spherulitic size) dominate the α-nucleation inherent embrittlement induced by a higher matrix crystallinity. Opposite conclusions are valid for the PP-4.2 grades.

Table 2 summarizes the temperatures at which the ductile-brittle occur for the different materials; the best combination is obtained with the β-nucleated PP-1.9 system – a fact which could hardly be foreseen with conventional notched impact strengths performed at given temperature and test speed (see Table 1). The relative performance of the grades within a nucleation group is representative for the interplay between the impact of the molecular weight of the rubbery phase and the resulting phase morphology.

Hence, for the non-nucleated systems no significant difference is observed between the ductile-brittle transitions of PP-1.9 and PP-4.2. Remembering that in an earlier study for iPP/EPR blends with 20 wt% of rubber the grade with the highest IV(XCS) outperformed by far its counterpart [28], one might conclude that the fracture behaviour of PP-4.2 is controlled primarily by the size of its particles while PP-1.9 is dominated by inter-particle factors. In other world, the initiation of the damage mechanisms (e.g. particle cavitation) is eased in PP-4.2 thanks to its bigger size while the propagation of the deformation forms (e.g. matrix shearing and crazing) is best for PP-1.9. Both contributions seem to counterbalance their respective influence leading to a T_{db} around –5°C for both systems.

Table 2. Temperature at which the ductile-brittle transitions occurred, T_{db}, and work at fracture, G_{tot}, at 23 and –20°C for the investigated grades

	T_{db} [°C]	G_{tot}(23°C) [kJ/m²]	G_{tot}(–20°C) [kJ/m²]
PP-1.9	–4	24.3	5.3
PP-1.9 + 0.1% NA11	–8	30.0	7.5
PP-1.9 + 0.1% CaPim	–30	36.0	33.6
PP-4.2	–6	53.5	16.5
PP-4.2 + 0.1% NA11	0	48.0	15.7
PP-4.2 + 0.1% CaPim	–4	53.0	19.0

For the α-nucleated systems, the inter-particle distance controls the fracture performance and it does – to an even larger extent – for the β-nucleated grades, with significantly lower ductile-brittle transition for the low IV series.

Such results have decisive implications in the polymer design of iPP/EPR blends:

– considering toughness as unique variable, it is extremely valuable to add β-nucleating agents to iPP/EPR blends with 32 w% rubber and low IV, since the ductile-brittle transition is shifted by almost 30°C towards lower temperature compared to a non-nucleated material;

– α-nucleating agents can constitute a tool to improve both toughness and stiffness for grades with 32 wt% rubber and low IV. However, the differences between IV = 1.9 and 4.2 (in terms of T_{db}) are much less pronounced than with β-nucleation. Adjustment of rubber IV to design α-nucleated iPP/EPR blends will therefore rather be governed by (i) the level of fracture resistance needed in both brittle and ductile ranges (compare G_{tot} at –30 and +30°C for both grades) and (ii) total MFR required.

4. Conclusions

The influence of α- and β-nucleation on the toughness of two Impact PP copolymers (32 wt% EPR) with different IV (1.9 and 4.2 dl/g) was investigated. An assessment of ductile-brittle transitions over a wide temperature range rather than of punctual values as given by standard testing methods was used for this purpose.

The effect of nucleation was shown to be dependent on the inter-particle distance of the systems: While the fracture resistance was improved with low rubber IV in terms of ductile-brittle transition (i.e. shifts the T_{db} of the blend to lower temperatures), a negative to negligible influence for the grade with higher molecular weight (IV) was found.

α-nucleation as well as β-nucleation therefore constitute powerful tools to optimise the toughness performance of iPP/EPR blends. Their selective use can be tailored for different applications.

References

[1] Gahleitner M., Wolfschwenger J., Bachner C., Bernreitner K., Neissl W.: Crystallinity and mechanical properties of PP-homopolymers as influenced by molecular structure and nucleation. Journal of Applied Polymer Science, **61**, 649–657 (1996).

[2] Pukánszky B., Mudra I., Staniek P.: Relation of crystalline structure and mechanical properties of nucleated polypropylene. Journal of Vinyl Additive Technology, **3**, 53–58 (1997).

[3] Karger-Kocsis J., Mouzakis D. E., Ehrenstein G. W., Varga J.: Instrumented tensile and falling weight impact response of injection-molded α- and β-phase polypropylene homopolymers with various melt flow indices. Journal of Applied Polymer Science, **73**, 1205–1214 (1999).

[4] Chen H. B., Karger-Kocsis J., Wu J. S., Varga J.: Fracture toughness of α- and β-phase polypropylene homopolymers and random- and block-copolymers. Polymer, **43**, 6505–6514 (2002).

[5] Varga J., Ehrenstein G. W., Schlarb A. K.: Vibration welding of alpha and beta polypropylenes: Mechanical properties and structure. Express Polymer Letters, **2**, 148–156 (2008).

[6] Kotek J., Scudla J., Slouf M., Raab M.: Combined effet of specific nucleation and rubber dispersion on morphology and mechanical behavior of isotactic polypropylene. Journal of Applied Polymer Science, **103**, 3539–3546 (2007).

[7] Cao J., Zhao Z. Y., Du R. N., Zhang Q., Fu Q.: Effect of β nucleating agent on mechanical properties of PP/POE blends. Plastics, Rubber and Composites, **36**, 320–325 (2007).

[8] Bernreitner K., Hauer A., Gubo R.: Polyolefin composition with improved properties. EU patent, EP 1344793 (2003).

[9] Kasahara T., Kajiya T., Akiyoshi T.: Propylene-ethylene block copolymer composition. EU patent, EP 0137482 (1985).

[10] Schwager H., Hungenberg K-D.: Nucleated propylene polymers. EU patent EP 518121 (1992).

[11] Torgersen U., De Mink P., Bernreitner K.: Flat film for thermoforming. WO 2004055101 (2003).

[12] Bai H., Wang Y., Song B., Li Y., Liu L.: Effect of nucleating agent on the brittle-ductile transition behavior of polypropylene/ethylene-octene copolymer blends. Journal of Polymer Science, Part B: Polymer Physics, **46**, 577–588 (2008).

[13] Grein C., Plummer C. J. G., Kausch H-H., Germain Y., Béguelin P.: Influence of β-nucleation on the mechanical properties of isotactic polypropylene and rubber modified polypropylene. Polymer, **43**, 3279–3293 (2002).

[14] Varga J., Schulek-Tóth F.: Crystallization, melting and spherulitic structure of β-nucleated propylene random copolymers. Journal of Thermal Analysis and Calorimetry, **47**, 941–955 (1996).

[15] Varga J.: β-modification of polypropylene and its two-components systems. Journal of Thermal Analysis and Calorimetry, **35**, 1891–1912 (1989).

[16] Varga J., Garzó G.: The properties of polymer blends of the β-modification of polypropylene and an elastomer. Die Angewandte Macromoleculare Chemie, **180**, 15–33 (1990).

[17] Zhang R., Zheng H., Lou X., Ma D.: Crystallization characteristics of polypropylene and low ethylen content polypropylene copolymer with and without nucleating agents. Journal of Applied Polymer Science, **51**, 51–56 (1994).

[18] Fanegas N., Gómez M. A., Jiménez I., Marco C., Garcia-Martínez J. M., Ellis G.: Optimizing the balance between impact strength and stiffness in polypropylene/elastomer blends by incorporation of a nucleating agent. Polymer Engineering and Science, **48**, 80–87 (2008).

[19] Menyhárd A., Varga J., Molnár G.: Comparison of different β-nucleators for isotactic polypropylene, characterisation by DSC and temperature-modulated DSC (TMDSC) measurements. Journal of Thermal Analysis and Calorimetry, **83**, 625–630 (2006).

[20] Varga J.: β-modification of isotactic polypropylene: Preparation, structure, processing, properties and applications. Journal of Macromolecular Science, Part B: Phys, **41**, 1121–1171 (2002).

[21] Turner Jones A,. Aizlewood A. M., Beckett D. R.: Crystalline forms of isotactic polypropylene. Die Makromolekulare Chemie, **75**, 134–158 (1964).

[22] Pölt P., Ingolic E., Gahleitner M., Bernreitner K., Geymayer W.: Characterization of modified polypropylene by scanning electron microscopy. Journal of Applied Polymer Science, **78**, 1152–1161 (2000).

[23] Labour T., Gauthier C., Séguéla R., Vigier G., Bomal Y., Orange G.: Influence of the crystalline phase on the mechanical properties of unfilled and $CaCO_3$-filled polypropylene, I. Structural and mechanical characterization. Polymer, **42**, 7127–7135 (2001).

[24] Wu S.: A generalized criterion for rubber toughening: The critical matrix ligament thickness. Journal of Applied Polymer Science, **35**, 549–561 (1988).

[25] Grein C.: Toughness of neat, rubber modified and filled β-nucleated polypropylene: From fundamentals to applications. Advances in Polymer Science, **188**, 43–104 (2005).

[26] Varga J., Ehrenstein G. W.: High temperature hedritic crystallisation of β-modification isotactic polypropylene. Colloid Polymer Science, **275**, 511–519 (1997).

[27] Trifonova-Van Haeringen D., Varga J., Ehrenstein G. W., Vancso G. J.: Features of the hedritic morphology of β-isotactic polypropylene studied by atomic force microscopy. Journal of Polymer Science, Part B: Polymer Physic, **38**, 672–681 (2000).

[28] Grein C., Bernreitner K., Hauer A., Gahleitner M., Neißl W.: Impact modified isotatic polypropylene with controlled rubber intrinsic viscosities: Some new aspects about morphology and fracture. Journal of Applied Polymer Science, **87**, 1702–1712 (2003).

eXPRESS Polymer Letters Vol.2, No.6 (2008) 398–403
Available online at www.expresspolymlett.com
DOI: 10.3144/expresspolymlett.2008.48

Adhesion property of epoxidized natural rubber (ENR)-based adhesives containing calcium carbonate

B. T. Poh[*], *P. G. Lee, S. C. Chuah*

School of Industrial Technology Universiti Sains Malaysia, 11800 Penang, Malaysia

Received 29 February 2008; accepted in revised form 10 April 2008

Abstract. The adhesion property (i.e. viscosity, loop tack and peel strength) of epoxidized natural rubber (ENR 25 and ENR 50 grade)-based pressure-sensitive adhesive was studied in the presence of calcium carbonate. The range of calcium carbonate loaded was from 10 to 50 parts per hundred parts of rubber (phr). Coumarone-indene resin was used as the tackifier and its concentration was fixed at 80 phr. Toluene was chosen as the solvent throughout the investigation. The substrates (PET film/paper) were coated with the adhesive using a SHEEN hand coater at a coating thickness of 60 μm. Viscosity of the adhesive was measured by a HAAKE Rotary Viscometer whereas loop tack and peel strength were determined by a Llyod Adhesion Tester operating at 30 cm/min. Results show that viscosity of ENR-based adhesives increases gradually with increase in calcium carbonate loading due to the concentration effect of the filler. However, for loop tack and peel strength, it passes through a maximum at 30 phr calcium carbonate, an observation which is attributed to the optimum wettability of adhesive on the substrate at this adhesive composition. ENR 25-based adhesive consistently exhibits higher adhesion property than ENR 50 for all calcium carbonate loadings studied.

Keywords: *adhesion, calcium carbonate, coatings, rubber*

1. Introduction

Recently, we have carried out a systematic study of the viscosity, tack, peel and shear strength of natural rubber (SMR L, SMR 10 and SMR 20)-based pressure-sensitive adhesives [1–3]. The study shows that viscosity and tack of the adhesive increases with an increase in coumarone-indene resin loading. For the peel strength, it generally indicates an increasing trend with resin loading, an observation which is associated to the increasing wettability of adhesive on the substrate as tackifier is increased. However, shear strength decreases gradually with increasing resin content. Our recent study on the adhesion properties of SBR/SMR L-based adhesives indicates that the viscosity of adhesive decreases with increasing % SBR whereas loop tack passes through a maximum value at 20% SBR composition [4]. Leong *et al*. [5] on the other hand have reported the viscoelastic properties of natural rubber pressure-sensitive adhesive using acrylic resin as a tackifier. Higher loss tangent at higher frequencies is obtained for good pressure-sensitive adhesives. With respect to the adhesive prepared from epoxidized natural rubber, systematic investigation on its adhesion property is scarce. We have reported that peel strength of ENR-based adhesive passes through a maximum value at 40 phr coumarone-indene resin [6]. Also, a gradual drop of shear strength with increasing tackifier loading is also observed. Recently, we have carried out a study on the effect of zinc oxide on the viscosity, tack and peel strength of ENR 25-based pressure-sensitive adhesives [7]. It is shown that viscosity and loop tack of adhesive increases with

[*]Corresponding author, e-mail: btpoh@usm.my

increasing zinc oxide concentration. However, peel strength passes through a maximum value at 30–40 phr of zinc oxide depending on the content of tackifier used. In order to understand better the dependence of adhesion property of adhesives on filler loading, we have extended a systematic investigation on the effect of calcium carbonate on the viscosity, tack and peel strength of pressure-sensitive adhesives prepared from two grades of ENR, i.e. ENR 25 and ENR 50.

2. Experimental

2.1. Materials

Two grades of epoxidized natural rubber, ENR 25 and ENR 50, having 25 and 50 mol% of epoxidation respectively were used as the elastomers for the preparation of the pressure-sensitive adhesives. The rubbers were supplied by Rubber Research Institute of Malaysia (RRIM). Precipitated calcium carbonate with mean particle size of 10 μm was used as the filler. It was not surface-treated. The tackifier used was coumarone-indene resin with an average molecular weight of 2000 and softening point of 80°C. Toluene was used as the solvent throughout the study. These were commercial grade materials and used as supplied.

2.2. Preparation of adhesive

ENR 25 and ENR 50 were masticated on a two-roll mill for 10 minutes. 5 g of the masticated rubber was then dissolved in 20 ml of toluene. The rubber solution was left overnight to ensure complete dissolution. 4 g of pulverized coumarone-indene resin corresponding to 80 phr resin was added to the rubber solution with constant stirring. Then, five different weights of calcium carbonate powder, i.e., 0.5, 1, 1.5, 2 and 2.5 g corresponding to 10, 20, 30, 40 and 50 phr of filler were added separately to the rubber solution containing coumarone-indene resin. For comparison purposes, one control sample without calcium carbonate was used to prepare the adhesive.

2.3. Measurement

2.3.1. Viscosity

A HAAKE Rotary Viscometer (Model PK 100) was used to determine the viscosity of the adhesives. Spindle head (PK1;1°) and the platform were wiped with acetone. The platform was then raised up to touch the spindle head. The gap between spindle head and platform was adjusted to zero before testing. A few drops of adhesive were put at the middle of platform which was then elevated to squeeze the adhesive. Excessive adhesive around the spindle head was wiped off with acetone. Testing was carried out for one minute or ten rounds of spinning at 30°C. The average of five readings was taken as the average viscosity of the adhesive.

2.3.2. Tack

A polyethylene terephthalate (PET) substrate with dimension of 4 cm×25 cm was used to determine the loop tack of the adhesive. It was coated at the centre (4 cm×4 cm) by a SHEEN Hand Coater at a coating thickness of 60 μm. The coated PET was air dried at 30°C for 24 hours to eliminate the toluene in the adhesive. A loop was formed from the PET film and the outer surface with adhesive area was gently brought into contact with a glass plate. The debonding force from the glass plate was measured at 30°C by a Lloyd Adhesion Tester (Model LRXPlus with NEXYGEN software) operating at a testing rate of 30 cm/min. The three highest peaks from the test were used to compute the average debonding force. The loop tack was defined as the debonding force per area of contact with the glass plate [N/m^2].

2.3.3. Peel strength

Polyethylene terephthalate (PET) film and release paper were used as the base stock and face stock respectively in the peel adhesion tests. In order to confirm the consistency of the results, three different modes of peel tests were conducted, viz. T-Peel Test, 90° Peel Test and 180° Peel Test. For the T- and 90° Peel Tests, the dimensions of both substrates were 20 cm×4 cm. However, for the 180° Peel Test, the dimensions of PET film was 25 cm×4 cm, whereas that of release paper was of 12 cm×6 cm. For all peel tests, a SHEEN Hand Coater was used to coat the adhesive from the end of the PET film at a coating area and thickness of 10 cm×4 cm and 60 μm respectively. The release paper was then placed on the coated PET film. The sample was air dried at 30°C for 24 hours to eliminate the toluene. The peel test was carried out at 30°C using a Lloyd

Adhesion Tester operating at 30 cm/min. As in the tack test, the average peeling force was determined from the three highest peaks of the load-propagation graph. Peel strength is defined as the average load per width of the bondline required to separate progressively a flexible member from a rigid member or another flexible member (ASTM D 907).

3. Results and discussion

The effects of calcium carbonate on the viscosity, tack and peel strength of ENR 25 and ENR 50-based pressure-sensitive adhesives are discussed below.

3.1. Viscosity

Figure 1 shows the dependence of viscosity of adhesive on calcium carbonate concentration. For both adhesives, viscosity increases gradually with increase in calcium carbonate loading. This observation is attributed to the thickening effect of calcium carbonate which acts as a filler in the adhesive formulation [8]. The higher the concentration of the filler, the greater is the thickening effect as reflected by the increase in viscosity. For all the loadings of filler, ENR 25 consistently indicates higher viscosity compared to that of ENR 50. The phenomenon may be explained by the stronger interaction (i.e. H-bonding) between ENR 25 and calcium carbonate filler. ENR 25 which has a lower T_g (i.e. –45°C) interacts better with the filler due to its greater flexibility compared to ENR 50 (T_g = –20°C). The difference in viscosity between ENR 25 and ENR 50-based adhesives (Z_v) with calcium carbonate loading is shown in Figure 2. Z_v value increases rapidly from 0 to 10 phr of filler loading and levels off after 10 phr filler suggesting that the rate of increasing ENR 25-filler interaction

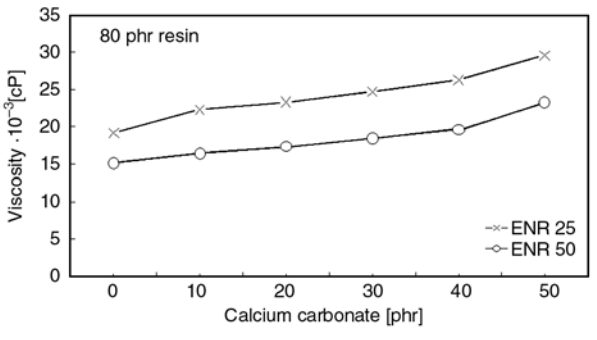

Figure 1. Variation of viscosity with calcium carbonate loading

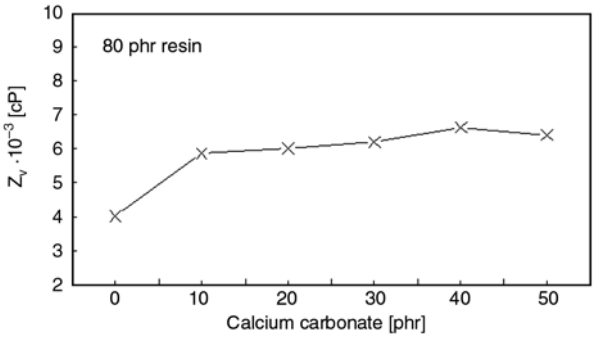

Figure 2. Variation of difference in viscosity (Z_v) with calcium carbonate loading

is faster than that of ENR 25 at the initial loading of calcium carbonate. However, after 10 phr of filler loading, rubber-filler interaction becomes nearly constant as shown by the plateau Z_v value with further filler loading.

3.2. Tack

The dependence of loop tack on the calcium carbonate loading for ENR 25 and ENR 50 is shown in Figure 3. Tack may be defined as the property of a material which enables it to form a bond of measurable strength immediately upon contact with another surface, usually with low applied pressure [8]. It gives an indication of how quickly an adhesive can wet and make intimate contact with a surface of a substrate. Result indicates that loop tack passes through a maximum value at 30 phr calcium carbonate loading for both rubbers studied. The increasing tack with increasing filler loading is attributed to the increasing wettability of adhesive on the substrate. At the maximum tack value, the adhesive conforms to the irregularities of the substrate, i.e. low surface energy condition is observed [9] at 30 phr calcium carbonate content. Further increase in the filler content will cause a dilution

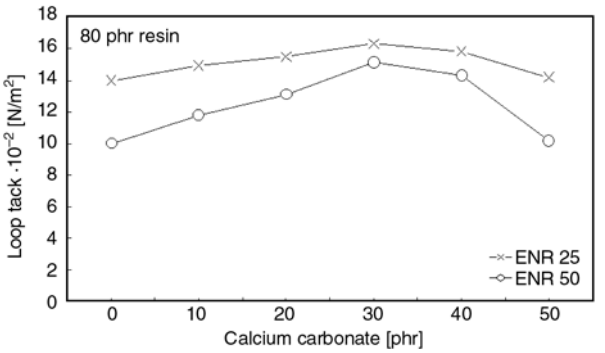

Figure 3. Variation of loop tack with calcium carbonate loading

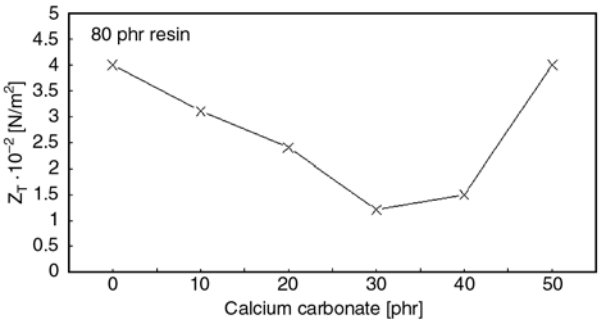

Figure 4. Variation of difference in loop tack (Z_T) with calcium carbonate loading

effect which decreases the miscibility and wettability of adhesive as indicated by the lowering of tack after 30 phr calcium carbonate loading. As in the case of viscosity, ENR 25-based adhesive consistently exhibits higher tack value compared to ENR 50 for all loadings of calcium carbonate. The difference in tack (Z_T) between ENR 25 and ENR 50-based adhesives is shown in Figure 4. Z_T decreases with calcium carbonate loading until a minimum is reached at 30 phr filler. After that it increases with further addition of the filler. This observation is attributed to the varying degree of interaction between ENR 25-calcium carbonate and ENR 50-calcium carbonate which affects the tack property of the respective adhesives. At 30 phr calcium carbonate loading, the difference in wettability between ENR 25 and ENR 50-based adhesive is minimal as reflected by the lowest Z_T value. However, increasing filler content widens the respective tack values due to the greater drop of miscibility and wettability of ENR 50-based adhesive.

3.3. Peel strength

The effect of calcium carbonate on peel strength of ENR-based adhesive is shown in Figures 5–7 for

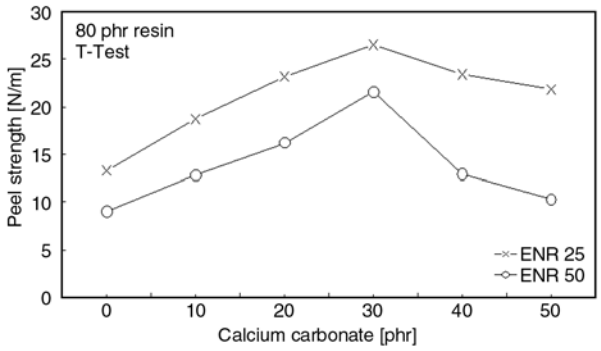

Figure 5. Peel strength (T-Test) versus calcium carbonate loading

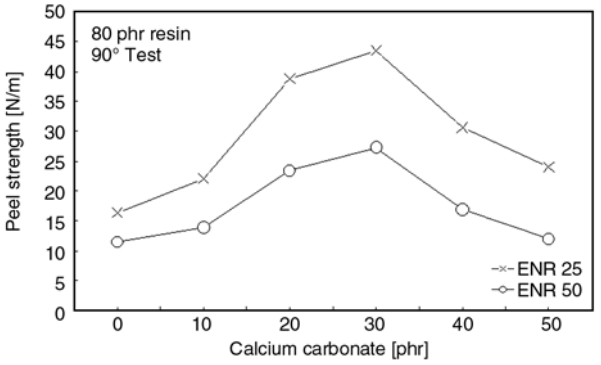

Figure 6. Peel strength (90° Test) versus calcium carbonate loading

the T-, 90° and 180° Tests respectively at 80 phr tackifier concentration. For all the three modes of testing, peel strength increases with increasing calcium carbonate loading up to 30 phr filler content and drops with further filler loading. This phenomenon is due to the continuous lowering of surface tension by calcium carbonate and hence better wettability of adhesive on the substrate is observed. As in the case of tack, wettability reaches a maximum value at 30 phr calcium carbonate loading for both rubbers studied. The increase in wettability enhances mechanical interlocking and anchorage of the adhesive in pores and irregularities in the adherent [10, 11]. After the optimum filler loading, peel strength decreases with further addition of filler because of the dilution effect of filler, thus reduces the miscibility and wettability of adhesive as exhibited by the drop in peel strength. From this study, ENR 25 consistently indicates higher peel strength than ENR 50, an observation which is similar to that reported in our earlier study of ENR in the absence of filler [6]. Figure 8 compares the peel strength of ENR 25 and ENR 50-based adhesives for various modes of peel tests. In all the tests, it is observed that ENR 25 gives higher peel strength than ENR

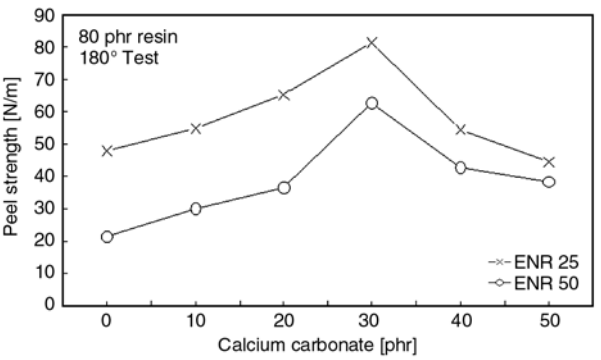

Figure 7. Peel strength (180° Test) versus calcium carbonate loading

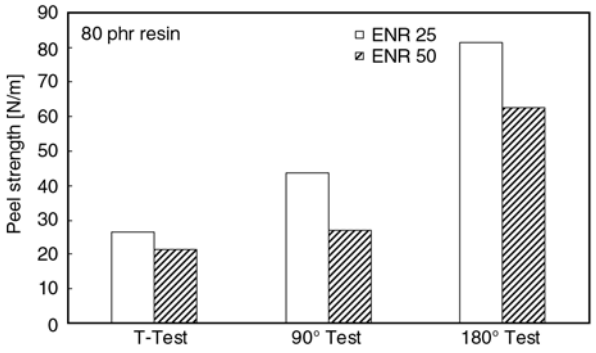

Figure 8. Comparison of peel strength between ENR 25 and ENR 50 at 30 phr calcium carbonate

50. This observation is attributed to the greater flexibility of ENR 25 due to its lower T_g value compared to ENR 50 as discussed earlier. This means that ENR 25-based adhesive will wet better than that of adhesive prepared from ENR 50. ENR 25 also undergoes more strain-induced crystallization [12–16] to enhance its resistance to rupture under an applied force so that the adhesive layer itself cannot easily be ruptured [8]. Figure 8 also shows that the peel strength obtained from the 180° Peel Test is much higher than the other two modes of testing. This is due to the angle of testing, an observation which is consistent with our previous report on the study of peel strength of SMR 10-based pressure-sensitive adhesive [1]. A higher peel force is needed in the 180° peel test which means that the rubber chains will undergo more strain-induced crystallization than the other two peel tests and hence, a higher peel strength is obtained. In all cases, the failure mode is essentially adhesive in nature.

4. Conclusions

The following conclusions can be drawn from this study:

1. Viscosity of ENR-based adhesives increases gradually with increase in calcium carbonate loading, an observation which is attributed to the thickening effect of calcium carbonate which acts as a filler in the adhesive system. ENR 25 consistently shows higher viscosity compared to that of ENR 50 indicating that interaction between ENR 25 and calcium carbonate is stronger compared to ENR 50.
2. Loop tack passes through a maximum value at 30 phr calcium carbonate loading for both rubbers studied. This observation is associated with the increasing wettability with increasing filler loading. However, further increase in the filler loading will decrease the miscibility and wettability of adhesive due to the dilution effect of the filler.
3. Peel strength increases with increasing calcium carbonate loading up to 30 phr filler content and drops with further filler loading, a phenomenon similar to that of tack test, i.e. varying degree of miscibility and wettability of adhesive with filler loading is observed. The increase in wettability enhances mechanical interlocking and anchorage of the adhesive in pores and irregularities in the substrate. ENR 25-based adhesive shows higher peel strength than that of ENR 50, an observation which is attributed to the greater flexibility of ENR 25 compared to ENR 50 due to the lower T_g in the former.

Acknowledgements

The authors acknowledge the research grant (FRGS) provided by Universiti Sains Malaysia that has resulted in this article.

References

[1] Poh B. T., Chang Y. Y.: Viscosity and peel strength of SMR 10-based pressure-sensitive adhesives. Polymer-Plastics Technology and Engineering, **45**, 1251–1256 (2006).
[2] Poh B. T., Chee C. L.: Effect of coumarone-indene resin on adhesion property of SMR 20-based pressure-sensitive adhesives. International Journal of Polymeric Materials, **56**, 247–255 (2007).
[3] Poh B. T., Kwo H. K.: Shear strength of SMR-based pressure-sensitive adhesives. Polymer-Plastics Technology and Engineering, **46**, 1021–1024 (2007).
[4] Poh B. T., Ong L. N.: Adhesion properties of styrene-butadiene rubber (SBR)/Standard Malaysian Rubber (SMR L)-based adhesives in the presence of phenol formaldehyde resin. Express Polymer Letters, **1**, 654–659 (2007).
[5] Leong Y. C., Lee L. M. S., Gan S. N.: The viscoelastic properties of natural rubber pressure-sensitive adhesive using acrylic resin as a tackifier. Journal of Applied Polymer Science, **88**, 2118–2123 (2003).
[6] Poh B. T., Kwo H. K.: Peel and shear strength of pressure-sensitive adhesives prepared from epoxidized natural rubber. Journal of Applied Polymer Science, **105**, 680–684 (2007).

[7] Poh B. T., Chow S. K.: Effect of zinc oxide on the viscosity, tack and peel strength of ENR 25-based pressure-sensitive adhesives. Journal of Applied Polymer Science, **106**, 333–337 (2007).
[8] Skeist I.: Handbook of adhesives. Van Nostrand Reinhold, New York (1990).
[9] Satas D.: Handbook of pressure-sensitive adhesive technology. Van Nostrand Reinhold, New York (1982).
[10] Gierenz G., Karmann W.: Adhesives and adhesive tapes. Wiley-VCH, New York (2001).
[11] Lee L. H.: Adhesive bonding. Plenum Press, New York (1991).
[12] Poh B. T., Khok G. K.: Tensile property of epoxidized natural rubber/natural rubber blends. Polymer-Plastics Technology and Engineering, **39**, 151–161 (2000).
[13] Davies C. K. L., Wolfe S. V., Gelling I. R., Thomas A. G.: Strain crystallization in random copolymers produced by epoxidation of *cis* 1.4 polyisoprene. Polymer, **24**, 107–113 (1983).
[14] Sadequl A. M., Poh B. T., Ishiaku U. S.: Effect of filler loading on the mechanical properties of epoxidized natural rubber (ENR 25) compared with natural rubber (SMR L). International Journal of Polymeric Materials, **43**, 261–278 (1999).
[15] Poh B. T., Ismail H., Quah E. H., Chin P. L.: Cure and mechanical properties of filled SMR L/ENR 25 and SMR L/SBR blends. Journal of Applied Polymer Science, **81**, 47–52 (2001).
[16] Poh B. T., Ismail H., Quah E. H.: Fatigue, resilience and hardness properties of unfilled SMR L/ENR 25 and SMR L/SBR blends. Polymer Testing, **20**, 389–394 (2001).

eXPRESS Polymer Letters Vol.2, No.6 (2008) 404–412
Available online at www.expresspolymlett.com
DOI: 10.3144/expresspolymlett.2008.49

Deformation mechanism under essential work of fracture process in polycyclo-olefin materials

*T. Kuno, Y. Yamagishi, T. Kawamura, K. Nitta**

Division of Material Sciences, Graduate School of Natural Sciences and Technology, Kanazawa University, Kanazawa, 920-1192 Japan

Received 8 February 2008; accepted in revised form 11 April 2008

Abstract. The fracture toughness of a glassy polycyclo-olefin (PCO) was investigated by the essential work of fracture (EWF) method using a double-edge notched specimens. It was shown that the PCO follows the EWF concept in the temperature range between room temperature and glass transition temperature T_g where the ligament yielding appear at a maximum point on the stress-displacement curves and subsequently the necking and tearing processes take place in the post yielding region. The essential work of fracture required for the ligament yielding drops as the temperature approaches T_g. The non-essential work of fracture attributed to tearing process after yielding is consumed to expand the plastic region and causes molecular chains to orient to the stretching direction.

Keywords: *fracture and fatigue, essential work of fracture (EWF), polycyclo-olefin, crack opening displacement, rheo-optics*

1. Introduction

Polycyclo-olefin (PCO) is a novel type of glassy polymers and received special attention in optical applications because of its environmental friendly and excellent heat- and chemical-resistances in addition to considerably low bifringence and high transparency. According to our previous studies on its tensile properties [1], PCO materials exhibited a high ductility near their glass transition temperatures T_g at which the PCOs are carefully compression molded to produce transparent sheets and films. The mechanical data in the vicinity of T_g are very useful to optimize the molding conditions.

The essential work of fracture (EWF) method developed by Broberg [2] has been conveniently used for the examination of fracture properties of ductile thin films. When a double edged notch specimen is loaded under uniaxial tension, the fracture is dissipated in two distinct zones such as fracture process zone (or essential zone) and plastic zone (or non-essential zone). The total work of fracture W_f is expressed as the sum between the two parameters of the essential work W_e and the non-essential work W_p, as shown by Equation (1) [2–6]:

$$W_f = W_e + W_p \tag{1}$$

The first term is related to the instability of the crack tip and represents the energy required to fracture the polymer in its process zone which is surface-related whereas the second term is associated with the plastic work, which is proportional to the plastic zone volume, and represents the energy consumed by various deformation mechanisms in the surrounding outer plastic zone [7–9]. When the typical load-displacement curve of double-notched specimen shows a maximum point at which the ligament region is fully yielded and the yielding region is necked after maximum, then may be parti-

*Corresponding author, e-mail: nitta@t.kanazawa-u.ac.jp

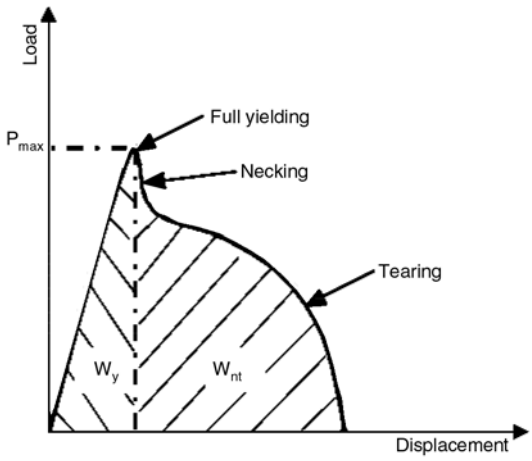

Figure 1. Schematic explanation of the definition of W_y and W_{nt}

tioned into two components as illustrated in Figure 1. Consequently, we have Equation (2):

$$W_f = W_y + W_{nt} \tag{2}$$

where W_y is the mechanical energy required for yielding of the ligament region and W_{nt} is the energy required for necking and subsequent tearing.

The EWF method has been widely applied to various commodity plastics such as poly(ethylene terephthalate), polyethylene, polypropylene, and their blends. It has been proven theoretically and confirmed experimentally that the essential work of fracture corresponds to the critical J-integral value which is the reliable method for characterizing the fracture toughness of ductile polymeric materials [10, 11]. The present work applies the concept of EWF for characterizing ductile fracture of PCO films as a function of temperature.

2. Analytical methods for essential work of fracture

The energy required for fracture W_e can be considered to be a pure crack resistance parameter. As a result, the value of W_e is essentially a surface energy and is proportional to the ligament length L for a given specimen thickness t. The plastic work W_p is a volume energy, which involves microvoiding and shear yielding and it is proportional to the volume L^2t. Dividing Equation (1) by the ligament section Lt, we have Equation (3):

$$w_f = \frac{W_f}{Lt} = w_e + \beta w_p L \tag{3}$$

where β is a shape factor associated with the volume of the plastic deformation zone, and w_p is the specific non-essential work of fracture, which is the plastic work per unit volume of the plastic deformation zone, and the specific essential work w_e is the failure work per unit surface area.

Equation (3) indicates that w_f is a linear function of ligament length L where the specific essential work of fracture w_e is given by the positive intercept at $L = 0$ of the linear regression interpolating the data and the specific non-essential work of fracture βw_p is given by the slope of the regression line. The main objective of the EWF method is to determine w_e as a toughness parameter.

The specific essential work of fracture w_e can be considered as a material constant under plane stress conditions for a given thickness t, as suggested from Equation (3). Furthermore, it is significant to consider partitioning of w_e since the total fracture work can be partitioned into two components of the ligament yielding and tearing work according to Equation (2) [12–14]. Consequently, the following equations have the form (see Equations (4) and (5)):

$$w_e = w_{ey} + w_{ent} \tag{4}$$

$$\beta w_p = \beta_y w_{py} + \beta_{nt} w_{pnt} \tag{5}$$

where w_{ey} is the specific essential yielding-related work of fracture, which is considered to be a more reliable parameter as compared to w_e to follow the extrinsic effects of the physical aging, the loading of plasticizer, and the water content [15–18], w_{ent} is the specific essential tearing work, w_{py} is the volumetric energy dissipated during yielding, and w_{pnt} is the dissipated work during tearing, and β_y and β_{nt} are geometric factors related to the shape of the plastic zone during the yielding and tearing stages, respectively.

3. Experimental

3.1. Materials

Polycyclo-olefin (Commercial grade: ZEONOR 1600) was used in this study. The PCO samples

were compression molded to sheets of about 100 μm thickness for 10 minutes under 270°C and 20 MPa. The rectangular sheets were notched to produce double-edge-notched tension (DENT) specimens with various ligament lengths by way of forming double edge notch transverse to the elongation direction by a sharp razor.

3.2. Standard EWF fracture tests

The DENT specimens with 20 mm width were tested to complete failure in an Instron 4466 tensile machine equipped maximum 100 N load cell and an isothermal chamber. The tests were performed at a fixed elongation rate of 1 mm/min between 15 and 163°C. The initial distance between cramps was 10 mm. We performed the EWF fracture measurements using more than 6 pieces with different ligament lengths ranging from 2.5 to 15 mm for each temperature. The mechanical energies W_y and W_{nt} were evaluated from the integration of the resulting load-displacement curves (see Figure 1).

3.3. Rheo-optical EWF fracture tests

Rheo-optical techniques [19] afford information on the elongation time dependence not only of the stress but also of optical quantities associated directly with the structure. In this study, infrared dichroism was measured simultaneously with stress during EWF tests at a constant rate of elongation.

For the purpose, a hand-made tensile tester was set in a Fourier-transformation infrared spectroscopic analyzer (FT-IR: MIR-8000 of ORIEL Co.) in such a way as to allow infrared polarized beam go through a DENT specimen mounted on the tensile tester. The tensile tester was specially designed for upper and lower clamps to symmetrically move from the central point in the ligament zone of the film so that the IR beam spot (3 mm diameter) remains at the initial position during whole stretching [20]. The rheo-optical EWF tests were performed under a constant elongation rate of 1 mm/min. In addition, the sample chamber of the stretching machine was equipped with an adiabatic temperature cell to maintain the temperature control at ±0.5°C. The smaller DENT specimens with a width of 15 mm were used for the rheo-optical measurements because of the space limitation of the sample chamber.

To determine the orientation function of molecular chain axes, we used the dichroic ratio D which can be determined by $A_{\parallel}/A_{\perp}$ where $A_{\parallel}$ and $A_{\perp}$ denote the absorbances measured for the radiation whose electric vectors are parallel and perpendicular to the stretching direction, respectively. The orientation function of molecular chain f is related to the dichroic ratio by Equation (6) [21, 22]:

$$f = \frac{2}{3\cos^2\phi - 1}\frac{D-1}{D+2} \tag{6}$$

where the ϕ is the angle between the direction of the transition moment of the absorption band and the main chain axis.

The intensities of 1480 cm^{-1} absorption bands were measured as a function of elongation time or displacement every 1–2 s. The band is associated with CH_2 scissoring vibration. The transition moment is considered to be 90 degrees direction against the main chain, $\phi = \pi/2$. The CH_2 scissoring of PCO was confirmed with the functional method of density using the calculation software of Gaussian Co. on the basis of a norbornene molecular model.

3.4. Sample characterization

The dynamic mechanical properties, the storage modulus E' and the loss modulus E'', were investigated in the tensile mode using the dynamic mechanical analyzer (DVE-V4 of Rheology Co.). The rectangular specimens with 7 mm width, 30 mm length, and 100 μm thickness were used for the measurements. The testing condition is the strain amplitude of 0.1%, the frequency 10 Hz,

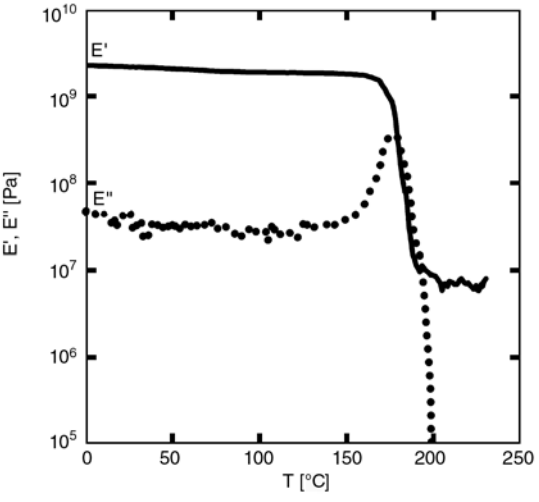

Figure 2. Dynamic mechanical spectra of PCO measured at 10 Hz

heating rate 2°C/min and the temperature range of 0–230°C. The dynamic mechanical spectrum was exemplified in Figure 2. A sharp relaxation peak in E'' curve, ascribed to the glass transition T_g, appears at 175°C and the storage modulus E' sharply reduces around the temperature.

The uniaxial tensile tests of the PCO sample were carried out using the notched-type specimens at the same temperature as the standard EWF tests. Details of the tensile measurements are referred in our previous paper [1].

4. Results and discussion

Figure 3 exemplifies the load-displacement curves from the EWF measurements at 102°C for the DENT samples having different ligament lengths. The curves have a clear maximum point and show a prominent load drop over the maximum point. The peak in the curve corresponds to the yielding around the ligament area. The sample specimen is subsequently necked and the failure is caused by ductile tearing of the ligament region after yielding. The rise in temperature reduces the overall maximum load and increases the elongation at break.

The important feature of the load-displacement curves for DENT specimens as a function of ligament length is their geometrical similarity. We directly confirmed that the width of the ductile deformation region in the samples after EWF tests was within the ligament length for the samples tested below 157°C. In addition, the linearity of the L dependence of W_f is established except for the values at 157°C within the squared multiple correlation coefficient (R^2) more than 0.95 as shown in Figures 5. These results suggest that the experimental conditions in this study satisfy the basic requirement for the applicability of the EWF analysis [6, 14]. Below room temperature, the failure of the PCO specimen occurs in a brittle manner in which the craze and/or cracks was formed at the root of the notch. Figure 4 shows the load-displacement curves measured at 15°C, showing that the specimens were broken prior to necking being independent of the ligament length. In the temperature range from 50 to 157°C, it was confirmed that the yielding of the ligament region occurs at maximum load at which two line plastic zones generated on the crack tips meet each other. The subsequent neck starts on the crack tips and rapidly reaches the whole ligament region, leading to a prominent load drop and then the crack starts to propagate across the necked zone until ultimate fracture occurs.

As shown in Figure 1, the specific work of fracture w_f, is the sum of their yielding component w_y and the necking component w_{nt}. Figures 5a and 5b show both components plotted against the ligament length L where the values of w_y and w_{nt} were calculated by integration of the area under the force-elongation curves. We confirmed the linear relationship between the fracture works and the ligament length L.

The specific essential work of fracture parameters and the specific non-essential work can be determined from the linear interpolation of these plots. The intercept values at $L = 0$ and slopes provide the essential work parameters and the non-essential work parameters, respectively, which were plotted

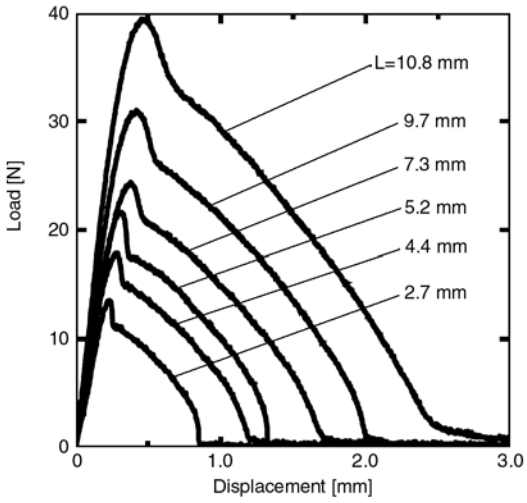

Figure 3. Force-displacement curves of the results of EWF test at 102°C

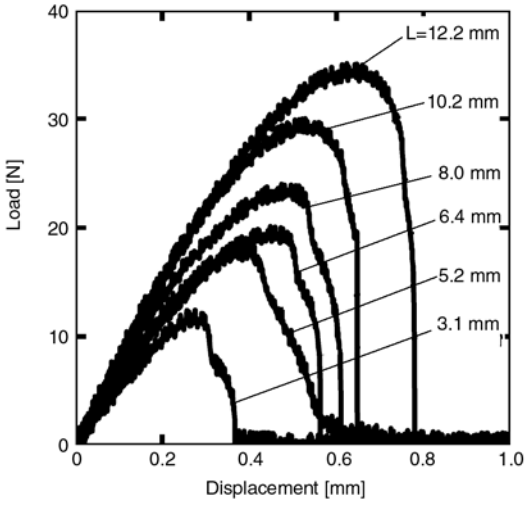

Figure 4. Force-displacement curves of the results of EWF test at 15°C

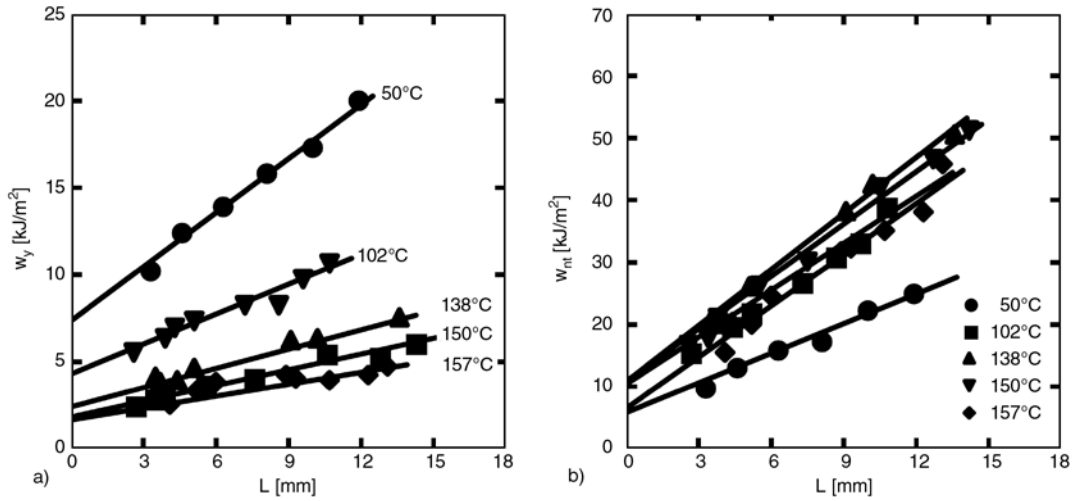

Figure 5. The dependence of w_y (a) and w_{nt} (b) on the ligament length at various temperatures

as a function of temperature in Figures 6a and 6b. The specific work of fracture w_e is almost independent of temperature in the lower temperatures but decreases as the temperature approaches T_g. Its component w_{ey} monotonically decreases with increasing temperature over the entire experimental temperature range whilst w_{ent} shows a maximum and rapidly drops at near T_g. Similar results for PEEK samples were reported by Arkhireyeva *et al.* [14], demonstrating that the w_{ey} values can be regarded as the specific essential work of fracture for crack initiation. Consequently, the variation of w_e with temperature for PCO was found to be almost caused by the temperature dependence of crack initiation.

The values of specific non-essential work of fracture βw_p, $\beta_y w_{py}$ and $\beta_{nt} w_{pnt}$ can be estimated from the slopes of the straight lines showed in Figures 5a and 5b. It was found that the values of βw_p and $\beta_{nt} w_{pnt}$ increase with increasing temperature below T_g and sharply drop at near T_g. On the other hand, the absolute values of the component $\beta_y w_{py}$ were found to monotonously decrease with increasing the temperature. It should be noted here that the values of $\beta_{nt} w_{pnt}$ are much greater than those of $\beta_y w_{py}$, indicating that almost non-essential work of fracture βw_p is due to $\beta_{nt} w_{pnt}$ and the plastic zone development is mainly associated with the necking-tearing part of the fracture process.

The displacement at fracture δ_b can be divided into the yield displacement δ_y and tearing component δ_{nt} giving by $\delta_b = \delta_y + \delta_{nt}$. The values of δ_b, δ_y and δ_{nt} are plotted against ligament length L in Figures 7a–7c. It was also found that the displace-

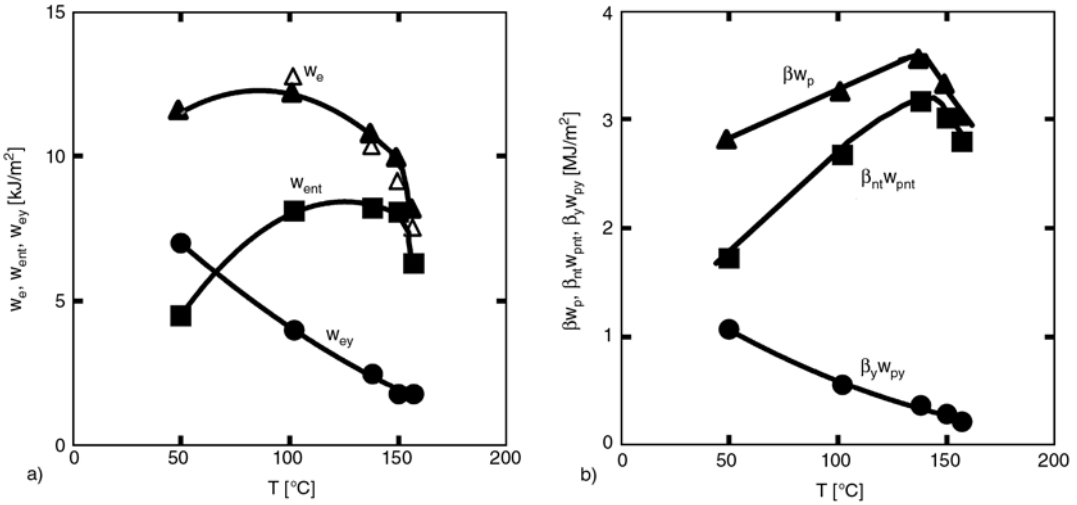

Figure 6. The temperature dependence of the essential work parameters (a) and the non-essential work parameters (b). The close symbols represent the parameters estimated directly from EWF tests and the open ones represent the parameters estimated from COD.

ments δ_b, δ_y, and δ_{nt} represent the liner relationships with L at any temperature. The displacement δ_b increases with increasing the temperature and the yield displacement δ_y is slightly dependent on temperature as compared to the tearing displacement δ_{nt}, indicating that the temperature sensitivity of the ultimate displacement δ_b is due to the temperature dependence of the tearing behavior. It is interesting to note that δ_{nt} and δ_y expolarate to a fixed value (0.18 mm) when $L \rightarrow 0$. Thus, we have the following empirical relations (see Equations (7) and (8)):

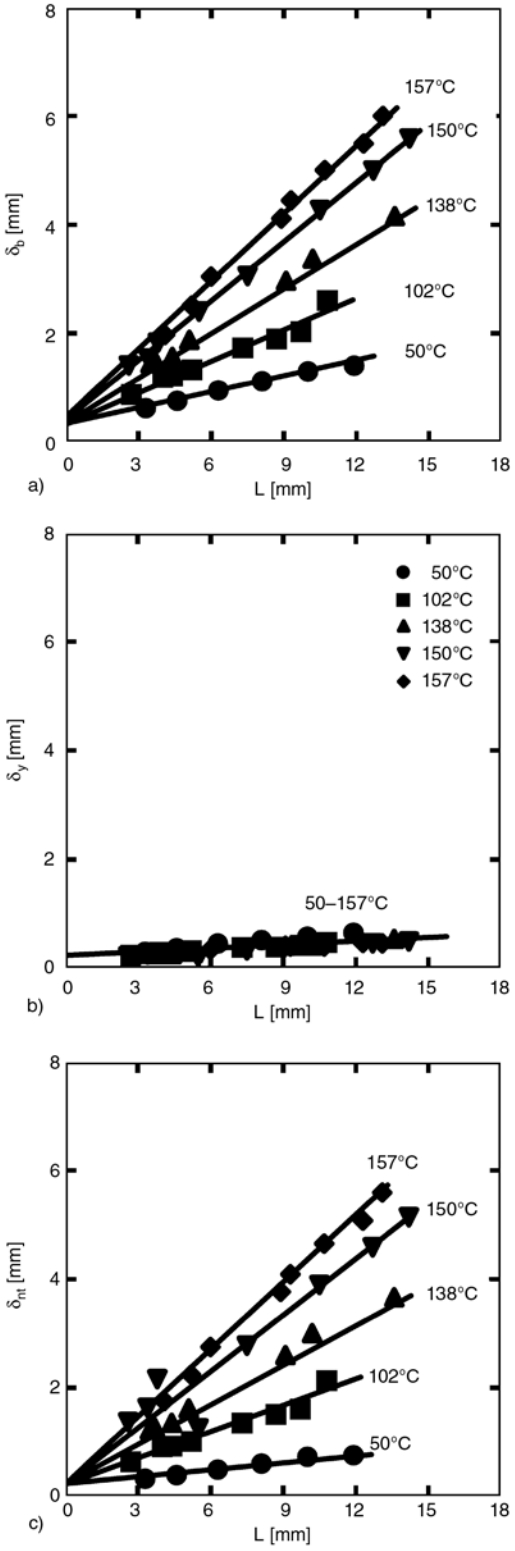

Figure 7. The dependence of displacement parameters on the ligament length at various temperatures. (a): total displacement δ_b, (b): displacement of yielding region δ_y and (c): displacement of necking-tearing region δ_{nt}

$$\delta_{nt} = \delta_{ent} + \alpha(T)L \tag{7}$$

$$\delta_y = \delta_{ey} + \alpha_y L \tag{8}$$

The intercept value $\delta_e = \delta_{ent} + \delta_{ey} = 0.36$ mm at $L = 0$ has been identified as being equivalent to the critical crack opening displacement [23]. As seen in Figures 7, we have $\delta_{ent} = \delta_{ey} = 0.18$ mm which were independent of temperature over the wide range from 50°C to near T_g, suggesting that the critical crack opening displacement is a material constant for PCO.

According to Arkhireyeva *et al.* [14], the values of w_e, w_{ent} and w_{ey} are directly related to the values of δ_e, δ_{ent} and δ_{ey}, respectively, according to Equations (9)–(11):

$$w_e = \lambda \sigma_Y \delta_e \tag{9}$$

$$w_{ey} = \lambda \sigma_Y \delta_{ey} \tag{10}$$

$$w_{ent} = \lambda \sigma_Y \delta_{ent} \tag{11}$$

where σ_Y is the yield stress and λ is the shape factor of the stress-stain curves below the yield point. The value of λ is assumed to be 0.67, which is attributed to the parabolic curve. The values of w_e, w_{ey} and w_{ent} estimated from COD were listed in Table 1 together with the values estimated directly from the EWF tests and the yield stress determined by the uniaxial tensile tests. The sample exhibited brittle behavior accompanied by no clear yield point at 50°C. The values of w_e determined from COD are coincident with the values from EWF tests at all the temperatures measured (shown in Figure 6a) though the values of w_{ey} determined form COD were overestimated and the values of w_{ent} were underestimated. The similar results for PEEK samples were reported by Arkhireyeva *et al*. [14].

Table 1. The yield stress (σ_Y), the specific essential work (w_e) and its components of the pre- and post-yield region (w_y and w_{ent}, respectively) estimated form EWF and COD

Temp. [°C]	σ_Y [MPa]	w_e [kJ·m^{-2}]		w_{ey} [kJ·m^{-2}]		w_{ent} [kJ·m^{-2}]	
		EWF	COD	EWF	COD	EWF	COD
50	–	12.0	–	7.0	–	4.5	–
102	53	12.0	13.0	4.0	6.3	8.1	6.3
138	42	11.0	10.0	2.5	5.1	8.2	5.1
150	38	9.9	9.1	1.8	4.5	8.1	4.5
157	31	8.1	7.5	1.8	3.7	6.3	3.7

Furthermore, we examined the temperature dependence of the slope $\alpha(T)$ of the δ_{nt}-L relation. As shown in Figure 8, the inverse of $\ln\alpha(T)$ was found to be proportional to the inverse of T_g–T. Thus, the temperature dependence of the slope $\alpha(T)$ becomes according to Equation (12):

$$\ln\alpha(T) = \frac{-c_1(T - T_g)}{c_2 + T - T_g} \tag{12}$$

where $c_1 = 3.82$ and $c_2 = -61.8$ K. It is very interesting to note that the empirical equation is the WLF type. Consequently, the empirical relation Equation (12) makes it possible to estimate the displacements at yield and break at any temperature.

The polarized IR spectra were measured simultaneously with the tensile stress as a function of tensile time or displacement. Smaller DENT specimens with 15 mm width were used for the measurements and the distance between two clamps was 15 mm. Figure 9 compares the work of fracture between EWF and rheo-EWF tests. As seen in this figure, it was confirmed that the fracture data obtained from rheo-EWF tests are almost consistent with those of the EWF tests. The data of orientation function measured simultaneously with EWF tests are shown in Figure 10 where both the load and the value of orientation function f are plotted against displacement at 110 and 170°C. The orientation function f was around zero up to the tearing start point and linearly increased with increasing the elongation. In the yielding in the ligament region almost no molecular chains orient to the stretching direction, indicating that large scale molecular mobility of molecular chains is not activated until ligament full-yielding. This suggests that the agglomeration of chain molecules act as a deformation unit and the work for yielding is consumed by the release of the agglomeration of chain molecules. On the other hands, the necking or tearing process induce the molecular orientation and the increase in molecular orientation function will be due to the expansion of necked region in the plastic zone. The plastic work for expanding the necking

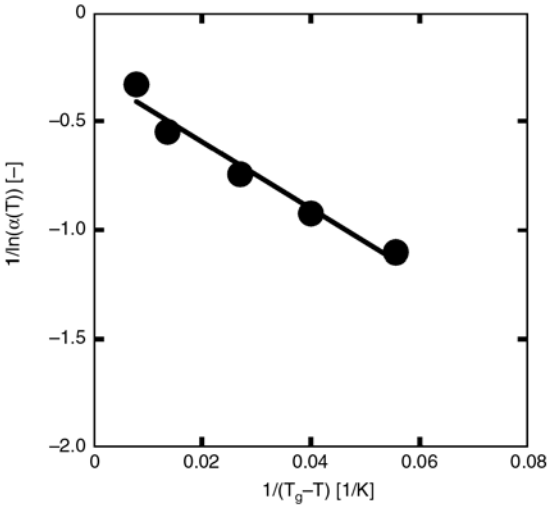

Figure 8. WLF plot of $\alpha(T)$ against T_g–T. $\alpha(T)$ represents the slope of displacement of necking-tearing region (δ_{nt}) against the ligament length

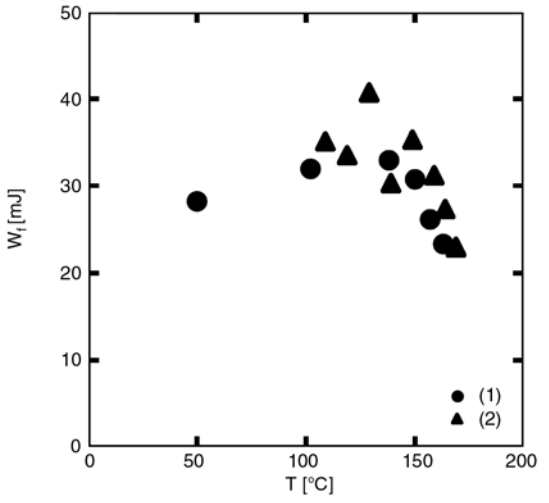

Figure 9. The temperature dependence of total work (W_f) for 2 samples with different size. (1): the sample for the EWF tests and (2): the sample for the rheo-optical EWF tests

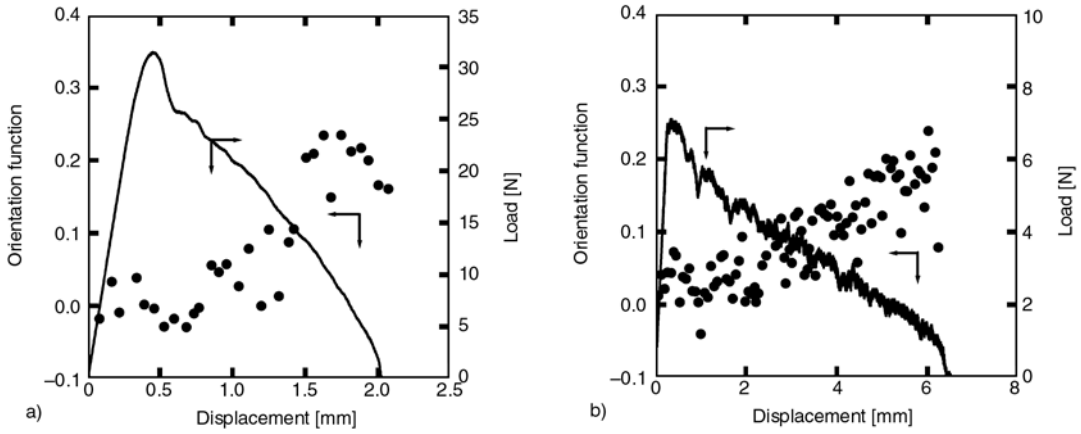

Figure 10. The load vs. displacement curves with simultaneous orientation function measurements of the DENT specimens at 110°C (a) and 170°C (b)

and/or tearing positively corresponds to the elongation sensitivity of molecular orientation, indicating that the work for the plastic deformation is consumed almost by the expansion of the molecular orientated (micro-necked) portions to the plastic plane.

5. Conclusions

The fracture toughness of polyolefin of a glassy polycyclo-olefin (PCO) was investigated between room temperature and near T_g by the essential work of fracture method using double-edge notched tensile specimens.

It was shown that the PCO follows the EWF concept in the temperature range between 50 and 157°C where the ligament yielding appear at a maximum point on the stress-displacement curves and subsequently the necking and tearing processes take place in the post yielding region. The essential work of fracture, w_e required for the ligament yielding drops as the temperature approaches T_g. The non-essential work of fracture, w_p attributed to tearing process after yielding is consumed to expand the plastic region and causes molecular chains to orient to the stretching direction.

A linear relationship was confirmed between the total specific work of fracture and ligament length over the entirely experimental temperature range. It was found that although specific essential work of fracture decreases with increasing temperature and the specific non-essential work of fracture increased with increasing temperature but dropped at near T_g. A linear relationship was also found for yielding and necking/tearing components of the total specific work of fracture as a function of ligament length. These specific essential work components were found to be dependent of temperature whilst the yielding component decreased with temperature. The contribution of necking/tearing component was substantially greater than that of the yielding component. Similarly, the displacement at fracture δ_b can be divided into the yield displacement and tearing component and the displacements were proportional to the ligament length. In addition, it was found that the temperature dependence of the displacement at break follows the WLF type of equation.

According to polarized FT-IR data measured simultaneously with EWF tests, the molecular orientation started in the post-yielding, indicating that the work for the plastic deformation is consumed almost by the expansion of the molecular orientated (micro-necked) portions to the plastic plane.

References

[1] Kuno T., Kawamura T., Nitta K.: Mechanical properties of polycyclo-olefins in the vicinity of the glass transition temperature. Polymer Bulletin, **59**, 847–854 (2008).

[2] Broberg K. B.: On stable crack growth. Journal of the Mechanics and Physics of Solids, **23**, 215–237 (1975).

[3] Cotterell B., Reddel J. K.: The essential work of plane stress ductile fracture. International Journal of Fracture, **13**, 267–277 (1977).

[4] Ward I. E., Sweeney J.: An introduction to the mechanical properties of solid polymers. Wiley and Sons, West Sussex (2004).

[5] Haward R. N., Young R. J.: The physics of glassy polymers. Chapman & Hall, London (1997).

[6] Wu J., Mai Y-W.: The essential fracture work concept for toughness measurement of ductile polymers. Polymer Engineering and Science, **36**, 2275–2288 (1996).

[7] Karger-Kocsis J., Czigány T., Moskala E. J.: Deformation rate dependence of the essential and non-essential work of fracture parameters in an amorphous copolyester. Polymer, **39**, 3939–3944 (1998).

[8] Arkhireyeva A., Hashemi S.: Effect of temperature on fracture properties of an amorphous poly(ethylene terephthalate) (PET) film. Journal of Materials Science, **37**, 3675–3683 (2002).

[9] Ferrer-Balas D., Maspoch M. L., Martinez A. B., Santana O. O.: On the essential work of fracture method: Energy partitioning of the fracture process in iPP films. Polymer Bulletin, **42**, 101–108 (1999).

[10] Mai Y-W., Cotterell B., Horlyck R., Vigna G.: The essential work of plane stress ductile fracture of linear polyethylenes. Polymer Engineering and Science, **27**, 804–809 (1987).

[11] Mai Y-W., Powell P.: Essential work of fracture and J-integral measurements for ductile polymers. Journal of Polymer Science, Part B: Polymer Physics, **29**, 785–793 (1991).

[12] Hashemi S.: Temperature dependence of work of fracture parameters in polybutylene terephthalate (PBT). Polymer Engineering and Science, **40**, 1435–1446 (2000).

[13] Bárány T., Karger-Kocsis J., Czigány T.: Effect of hygrothermal aging on the essential work of fracture response of amorphous poly(ethylene terephthalate) sheets. Polymer Degradation and Stability, **82**, 271–278 (2003).

[14] Arkhireyeva A., Hashemi S.: Effect of temperature on work of fracture parameters in poly(ether-ether ketone) (PEEK) film. Engineering Fracture Mechanics, **71**, 789–804 (2004).

[15] Karger-Kocsis J., Bárány T., Moskala E. J.: Plane stress fracture toughness of physically aged plasticized PETG as assessed by the essential work of fracture (EWF) method. Polymer, **44**, 5691–5699 (2003).

[16] Bárány T., Ronkay F., Karger-Kocsis J., Czigány T.: In-plane and out-of-plane fracture toughness of physically aged polyesters as assessed by the essential work of fracture (EWF) method. International Journal of Fracture, **135**, 251–265 (2005).

[17] Bárány T., Földes E., Czigány T.: Effect of thermal and hygrothermal aging on the plane stress fracture toughness of poly(ethylene terephthalate) sheets. Express Polymer Letters, **1**, 180–187 (2007).

[18] Karger-Kocsis J., Moskala E. J.: Toughness response of amorphous (co)polyesters using the essential work of fracture approach. ANTEC Papers, **60**, 1751–1755 (2002).

[19] Ke B.: New methods of polymer characterization. Wiley, New York (1968).

[20] Nitta K., Okamoto K., Yamaguchi M.: Mechanical properties of binary blends of polypropylene with ethylene-α-olefin copolymer. Polymer, **39**, 53–58 (1998).

[21] Zbindem R.: Infrared spectroscopy of high polymers. Academic Press, New York (1964).

[22] Onogi S., Asada T., Tanaka A.: Rheo-optical studies of high polymers. XIV. Study of the deformation mechanism in polymer blends of polypropylene with ethylene-propylene rubber. Journal of Polymer Science Part A-2: Polymer Physics, **7**, 171–182 (1969).

[23] Mouzakis D. E., Karger-Kocsis J., Moskala E. J.: Interrelation between energy partitioned work of fracture parameters and the crack tip opening displacement in amorphous polyester films. Journal of Materials Science Letters, **19**, 1615–1619 (2000).

eXPRESS Polymer Letters Vol.2, No.6 (2008) 413–422
Available online at www.expresspolymlett.com
DOI: 10.3144/expresspolymlett.2008.50

The effects of acetylation on properties of flax fibre and its polypropylene composites

A. K. Bledzki[1*], *A. A. Mamun*[1], *M. Lucka-Gabor*[1], *V. S. Gutowski*[2]

[1]Institut für Werkstofftechnik, Kunststoff- und Recyclingtechnik University of Kassel, Mönchebergstr. 3, D-34109 Kassel, Germany
[2]CSIRO Manufacturing & Infrastructure Technology, Novel Materials & Processes, PO Box 56, Highett Melbourne, Victoria 3190, Australia

Received 19 February 2008; accepted in revised form 13 April 2008

Abstract. Flax fibre was modified with acetylation. The influence of the acetylation on the structure and properties of flax fibre were investigated as well as modified flax fibre reinforced polypropylene composites were also prepared. The catalyst was used to accelerate acetylation reaction rate. Flax fibre was characterised after modification. Surface morphology, moisture absorption property, components content, degree of polymerisation, crystallinity of cellulose and thermal stability of flax fibres were studied. Due to acetylation, the flax fibre surface morphology and moisture resistance properties improved remarkably. Flax fibre (modified and unmodified) reinforced polypropylene composites were fabricated with 30 wt% fibre loading. The mechanical properties were investigated for those composites. Tensile and flexural strengths of composites were found to increase with increasing degree of acetylation up to 18% and then decreased. Charpy impact strengths of composites were found to decrease with increasing degree of acetylation. Owing to addition of coupling agent (maleated polypropylene -MAH), the tensile and flexural strength properties were found to increase in between 20 to 35% depending on degree of acetylation.

Keywords: *reinforcements, flax fibre, acetylation, fibre characterisation, mechanical properties*

1. Introduction

A better understanding of the chemical composition and surface adhesive bonding of natural fibre is necessary for developing natural fibre-reinforced composites. The composition of natural fibres includes cellulose, hemicellulose, lignin, pectin, fat, waxes and water soluble substances [1–3]. The composition may differ with the growing condition and test methods even for the same kind of fiber [4]. Cellulose is a semicrystalline polysaccharide with a large amount of hydroxyl group in cellulose, giving hydrophilic nature to natural fibre when used to reinforce hydrophobic matrices; the result is a very poor interface and poor resistance to moisture absorption [5]. Hemicellulose is strongly bound to cellulose fibrils presumably by hydrogen bonds. Hemicellulosic polymers are branched, fully amorphous and have a significantly lower molecular weight than cellulose. Because of its open structure containing many hydroxyl and acetyl groups, hemicellulose is partly soluble in water and hygroscopic [6]. Lignins are amorphous, highly complex, mainly aromatic, polymers of phenylpropane [7] units but have the least water sorption of the natural fibre components [6].

The natural fibre exhibits a high hydrophilicity due to attraction or interaction between the hydroxyl groups of fibre components and water molecules. The interactions between fibre and water originate from the non-crystalline region and extend to the

*Corresponding author, e-mail: kutech@uni-kassel.de

crystalline region. The uptake of water by hygroscopic substance such as cellulose and hemicellulose is a hydration process involving accessible hydroxyl groups. Water molecule absorbed by cellulose molecule form cellulose hydrate and the reaction is exothermic, which provide the driving force for further absorption [8, 9]. The high moisture sensitivity of lignocellulosic fibre causes the dimensional instability and limits the use of fibre as reinforcement in composite materials. Low interfacial properties between fibre and polymer matrix often reduce their potential as reinforcing agents due to the hydrophilic nature of natural fibres; chemical modifications are considered to optimize the interface of fibres. Generally, chemical coupling agents are molecules possessing two functions. The first function is to react with hydroxyl groups of cellulose and the second is to react with functional groups of the matrix [10].

The moisture absorbed by the fibres can be reduced by chemical modifications of fibres such as acetylation, methylation, cyanoethylation, benzoylation, permanganate treatment, acrylation etc. [11–15].

Acetylation of natural fibres is a well-known esterification method causing plasticization of cellulosic fibres. Polymer hydroxyl groups of the cell wall with acetyl groups, modify the properties of these polymers so that they become hydrophobic which could stabilize the cell wall against moisture, improving dimensional stability and environmental degradation [16].

In addition, acetylation is one of the most studied reactions of lignocellulosic materials. Cellulose acetate was discovered in 1865, and partially acetylated cellulose products were commercialised as acetate rayon fibres and cellulose acetate plastics in the early 1900s. The first attempt of acetylating wood flour and sawdust took place in 1928. The principle of the method is to react the hydroxyl groups (–OH) of the fibre constituents with acetyl groups (CH_3CO–). The reaction is known to proceed to full esterification of all the three hydroxyls of anhydro-D-glucose when it is carried out in a homogeneous phase (i.e. when cellulose is dissolved), but in the case of fibres and wood where the reaction is heterogeneous. So it is thought to esterify all hydroxyl groups of the fibre. Hence, a highly non-uniform product may be obtained. In these cases, it is necessary to use catalyst speeding up acetylation process. There are large number of catalysts that have been used in the past, including sulphuric acid, pyridine, potassium and sodium acetate, gamma-rays, etc. However, the use of catalysts poses many problems. Strong mineral acids or acid salts are known to cause hydrolysis of cellulose resulting in damage of the fibre structure [17]. So, selection and optimization of catalyst is important for the acetylation of lignocellulosic fibre. The hydroxyl groups that react are those of the minor constituents of the fibre, i.e. lignin, hemicelluloses, and those of amorphous cellulose. That is because the hydroxyl groups in crystalline regions with close packing and strong interlock bonding are completely inaccessible [18].

Reduction of about 50% of moisture uptake for acetylated jute fibres and of up to 65% for acetylated pine fibres has been reported in the literature [10].

Seena *et al.* investigated the effect of acetylation in banana fibre reinforced phenol formaldehyde composites and reported that the tensile strength, tensile modulus and impact strength are found to improve compared to non treated banana fibre composites [12].

Liu *et al.* studied the effect of acetylation in natural fibre composites (cotton, rayon, wood with polystyrene as matrix) and they showed, by using the micro-debonding test that acetylated fibres had increased interfacial shear strength. Furthermore, they reported that acetylation increased the surface free energy of the fibres [19].

Zafeiropoulos *et al.* investigated aectylation of flax, hemp and wood fibre and resulted in a removal of non-crystalline constituents of the fibres, altered the characteristics of the surface topography, changed the fibre surface free energy and improved the stress transfer efficiency at the interface [17, 20].

In the present work a detailed investigation has been carried out on the effect of acetylation on the flax fibre properties in terms of fibre composition, fibre surface, degree of crystallinity, degree of polymerisation, moisture absorption and thermal stability, as well as, a detailed investigation has been investigated on the effect of acetylation of flax fibre on the flax fibre reinforced polypropylene composites properties.

2. Experimental

2.1. Materials

Green flax fibre (6–8 mm) was obtained from Mühlmeier GmbH, Germany.

Acetic anhydride, toluene, perchloric acid, sodium hydroxide, hydrochloric acid, ethanol, sulphuric acid, acetic acid, sodium chlorite, acetone, iodine, potassium iodine, sodium sulphate, sodium thiosulphate were collected from Merck KgaA, Darmstadt, Germany. All chemicals were analytical grade.

A commercially available maleic anhydride-polypropylene copolymer (Licomont AR 504 FG) with an acid number of 37–43 mg KOH/g was used as a coupling agent. It was obtained from Clariant Corporation, Frankfurt, Germany. Its softening point was 153°C and density was 0.89–0.93 gm/cm^3. It accounted for 5% of the weight percentage of fibre.

2.2. Methods

2.2.1. Acetylation process

The flax fibres were soaked in demineralised water for an hour, filtered and placed in a round bottom flask, containing acetylating solution. Acetylating solution consist of 250 ml toluene, 125 ml acetic anhydride and a small amount of catalyst perchloric acid (60%). The process temperature of acetylation was 60°C and duration was 1 to 3 hour. After modification, the fibre was washed periodically with distilled water until acid free. Finally modified flax fibres were air dried for certain time before investigation.

2.2.2. Modified fibre characterisation

Degree of acetylation

The acetyl groups' content was measured by saponification methods. Modified flax fibre was saponified by 0.5N sodium hydroxide solution. After saponification, the excess alkali was titrated by 0.5N hydrochloric acid. Similar method has been considered for untreated flax fibre and the degree of acetylation calculated from the difference.

Extractibles content

The air dried sample of 5 g was weighed in an extraction thimble and placed in Soxhlet extraction unit. A mixture of ethanol and toluene was used as solvent and extraction process continued for a period of five hours. After extraction the sample was rinsed with ethanol and hot water and dried up to constant weight at the temperature of 60°C. The extractibles were calculated as a percentage of the oven dried test sample and the method has been repeated for each sample.

Lignin content

Two grams of extracted sample were placed in a flask and 15 ml of 72% sulphuric acid was added. The mixture was stirred frequently for two and half hours at 25°C and 200 ml of distilled water were added to the mixture. Then the mixture was boiled for next two hours and cooled. After 24 hours, the lignin was transferred to the crucible and washed with hot water repeatedly until becoming acid free. The collected lignin was dried at 105°C and cooled down in desiccator and weighed. The drying and weighing were repeated until constant weight.

Holocelluloses content

Three grams of air dried flax fibre were weighed and placed in an Erlenmeyer flask and then, 160 ml of distilled water, 0.5 ml of glacial acetic acid and 1.5 g of sodium chloride were added successively. The flask was placed in water bath and heated up to 75°C for an hour and then additional 0.5 ml of glacial acetic acid and 1.5 g of sodium chloride were added. The additions of acetic acid and sodium chloride were repeated two times hourly. The flask was placed in an ice bath and cooled down below 10°C. The holocellulose was filtered and washed with acetone, ethanol and water respectively and at the end, sample was dried in oven at 105°C before weighed.

α-cellulose content

Two grams of holocellulose were placed in a beaker and 10 ml of sodium hydroxide solution (17.5%) was added. The fibres were stirred up by glass rod so that they could be soaked with sodium

hydroxide solution vigorously. Then sodium hydroxide solution was added to the mixture periodically (once every five minutes) for half an hour and the mixture temperature was kept at 20°C. About 33 ml of distilled water was added in the beaker and kept it for an hour. The holocellulose residue was filtered and transferred to the crucible and washed with 100 ml of sodium hydroxide (8.3%), 200 ml of distilled water, 15 ml of acetic acid (10%) and again water successively. The crucible with α-celluloses was dried and weighed.

Hemicellulose content

The content of hemicelluloses of flax fibre was calculated from Equation (1):

$$\text{Hemicelluloses} = \text{Holocellulose} - \alpha\text{-celluloses} \quad (1)$$

Degree of polymerisation of cellulose

The molecular weight of cellulose was measured by capillary viscometry according to the Cuoxam method. It was observed that the cellulose was not completely soluble in cuoxam solution. Before measurement, the solution was filtered and viscosity was measured. This method was performed at room temperature and this method is valid for the viscosity range of $0.1 < \eta < 2.0$. Temperature and damage correction factors have been considered during calculation. The average molecular weights (DP = degree of polymerisation) were calculated by using Equation (2):

$$DP = \eta/[1 + (0.28 \cdot \alpha)] \cdot (1000/6.1C) \quad (2)$$

where η is the specific viscosity, C is the concentration of cellulose materials in cuoxam solution.

Degree of crystallisation of cellulose

The crystallinity of cellulose was determined according to iodine absorption method. Treated flax fibres (0.3 g) were taken in a beaker and 2 ml of iodine solution (10 g iodine and 80 g potassium iodide in 100 ml of demineralised water) and 100 ml of saturated sodium sulphate solution were added. The temperature was adjusted to 20°C before adding sodium sulphate solution and then the beaker was kept in the dark place for an hour. The remaining iodine in solution was determined by titration with 0.03 M sodium thiosulphate (starch as indicator).

Thermo gravimetric analysis (TGA)

The thermal gravimetric analysis of treated and untreated flax fibres were conducted by thermal gravimetric analyser (TGA-Model TG 50), supplied by TA Instrument. 20 mg sample of each type of fibre has been taken for analysis. The samples were heated up; steadily at a rate of 20 K/min from 25 to 500°C in nitrogen medium. To get perfection, analysis has been done two times for each sample.

Scanning electron microscope

The morphology of treated and untreated flax fibres were investigated using scanning electron microscope (SEM), MV2300, CamSan Electron Optics. Flax fibres were fixed on metal surface with special adhesive and sputter coated with gold before investigation.

2.2.3. Processing of Composites by mixer-injection moulding

Treated or untreated flax fibres with polypropylene were mixed by high speed cascade mixer (Henschel heat-cooling mixer system, type HM40-KM120). Flax fibres were dried at 80°C in an air circulating oven for 24 hours (moisture content < 1%) before mixing. The flax fibre at 30% proportion and polypropylene was placed into hot mixer and heated to the melting temperature of polypropylene (173°C) and then hot agglomerate granules were transferred to the cool mixer where hot agglomerate granules were cooled down to room temperature by the cold water. Then cold agglomerate granules were dried again (80°C, 24 hours) before the sample preparation by injection moulding process. Test samples were prepared from dried agglomerate by injection moulding process at temperature zone 150–180°C, mould temperature of 80°C with an injection pressure of 20 kN/mm^2.

2.2.4. Characterization of composites

Tensile, flexural and impact tests were carried out for characterization of composites. Tensile and flexural tests were performed at a test speed of

2 mm/min according to EN ISO 527 and EN ISO 178 using a Zwick UPM 1446 machine. All tests were performed at room temperature (23°C) and at a relative humidity of 50%. Charpy impact test was carried out using 10 notched samples according to EN ISO 179 using Zwick Charpy impact machine. In each case a standard deviation < 5% (drop weight) was used to calculate the Charpy impact strength.

3. Results and discussion

3.1. Acetylation process

3.1.1. Effects of catalyst

The flax fibres modification was conducted with varying percentage of catalyst at 60°C temperature. The acetylation process was studied with and without catalyst. It was observed that the acetylation reaction rate increased in the presence of catalyst and without catalyst the reaction kinetic of acetylation process was slower and dependent on fibre moisture content which is illustrated in Figure 1 [17]. It was found that by addition of 0.026% catalyst in acetylation process, the reaction rate increased and it was nearly triple after one hour. The degree of acetylation of flax fibre could reach up to 40–45% in the presence of 0.052% catalyst in three hours duration. With a catalyst content of more than 0.052% it is difficult to control acetylation process because the kinetic of reaction is very fast and suddenly damages the fibre.

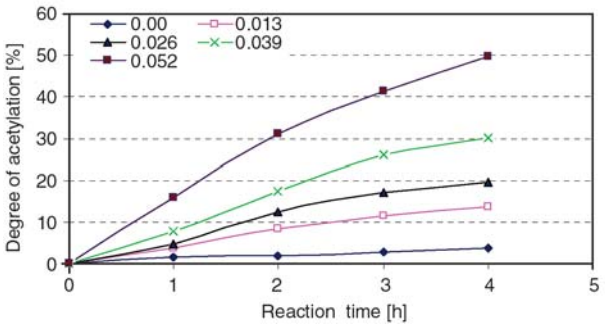

Figure 1. Influence of catalyst concentration on degree of acetylation

3.2. Fibre characterisation

3.2.1. Moisture absorption

The influence of degree of acetylation of flax fibre on the moisture absorption properties were illustrated in Figure 2 and Figure 3 respectively at different relative humidity (65, 95%). At the RH of 65%, the 3.6, 12, 18 and 34% degree of acetylated flax fibre respectively showed about 21, 32, 40 and 50% lower moisture absorption properties than untreated flax fibre. At 95% RH, the 3.6, 12, 18 and 34% degree of acetylated flax fibre showed about 14, 18, 27 and 42% lower moisture absorption properties than untreated flax fibre respectively. It was observed that the moisture absorption properties decreased proportionally with increase of acetyl content of fibre which is because of reduction of hydrophilicity of the fibre.

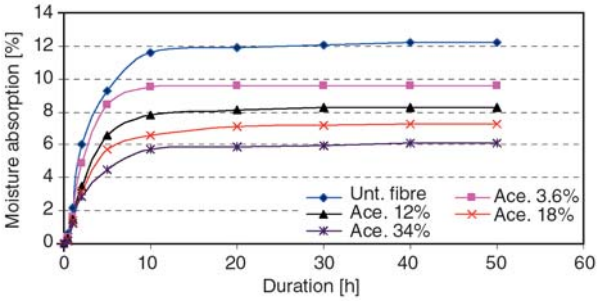

Figure 2. Influence of acetylation of flax fibre on moisture absorption property at 65% relative humidity

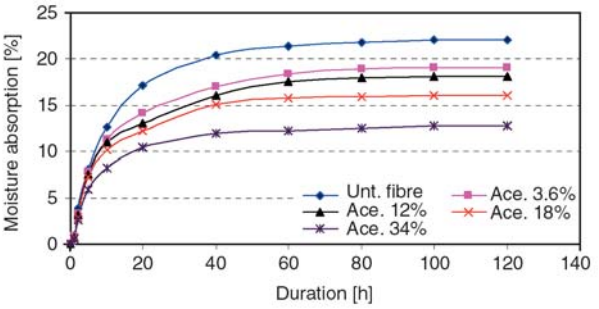

Figure 3. Influence of acetylation of flax fibre on moisture absorption property at 95% relative humidity

3.2.2. Fibre components

The influence of acetylation on the composition of the fibres is shown in the Figure 4. It was observed that the cellulose contents increased gradually until 12% degree of acetylation which is due to the extraction of lignin and extractibles from fibre and after that the cellulose contents decreased slowly which is because of degradation of cellulose, increased amorphous content and acetylated hemicellulose deposition on the fibre surface [20]. It was also observed that the lignin contents decreased steadily until 34% acetylation which is because of solubility of lignin and the extractives content

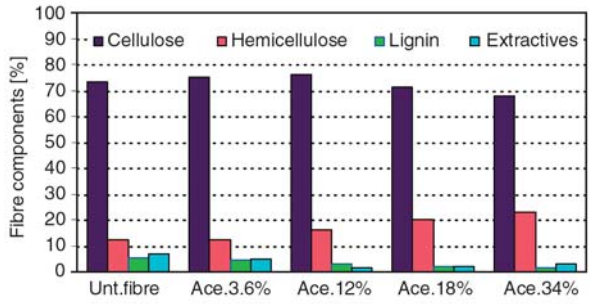

Figure 4. Influence of acetylation of flax fibre on the content of fibre components

decreased till 12% acetylation and then increased slowly which is because of cellulose degradation. On the other hand hemicellulose contents were found to increase with increasing degree of acetylation.

3.2.3. Degree of polymerisation and crystallinity of cellulose

The effects of the acetylation on the degree of polymerisation and crystallinity of cellulose illustrated in Figure 5. It was observed that the degree of polymerisation slowly decreased with increasing degree of acetylation till 18%. It is because of increase amorphous (low molecular weight acetylhemicellulose) content. After 18% acetyl content the degree of polymerisation decreased sharply which because of vigorous degradation of cellulose.

From the Figure 5 it is also observed that the degree of crystallinity a little bit increased initially with respect to degree of acetylation which is because of removal of lignin and extractibles. After that the degree of crystallinity of cellulose decreased with respect to degree of acetylation which is because of deposition of acetylated amorphous components on cellulose surface [20].

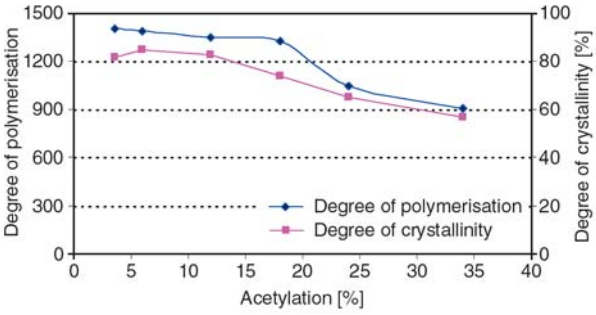

Figure 5. Influence of acetylation of flax fibre on the degree of polymerisation and degree of crystallinity of cellulose

3.2.4. Thermal stability

The effect of acetylation of flax fibre on the thermal properties is shown in Table 1. It was observed that the thermal stability improved with increasing degree of acetylation. It was also observed that the degradation temperature of untreated flax is 319°C. The flax fibre with 34% acetyl content showed best thermal stability, and the degradation temperature was found to increase to 360°C compared to untreated fibre. The increase of thermal stability of acetylated fibre was because of washing out of wax, lignin and hemicellulose from the fibre surface. Simultaneously it was also observed that with increasing degree of acetylation a little portion of acetylated hemicellulose deposited on to the fibre surface in presence of catalyst. Fibre chemical compositions determination is the evidence.

3.2.5. Morphology

Surface morphology of treated and untreated fibres is shown in Figure 6. In the Figure 6a, 6b, it was observed that the untreated fibre surface is rough, exhibiting waxy and protruding parts. The surface morphology of treated fibre viewed in Figure 6c, 6d. On the acetylation treatments the wax and cuticle in the surface is removed by the interaction with acetyl and surface becomes smother. The fibrillation is also found to occur as the binding materials removed and some micropores appear in the treated fibres. It was also observed from Figure 6e, 6f that the higher degree of acetylation the fibrillation increased but fibre damage and crack were also observed.

3.3. Mechanical properties of composites

3.3.1. Tensile properties

Figure 7 shows the degree of acetylation of flax fibre on tensile properties of composites. Tensile

Table 1. Thermal stable temperature of treated and untreated flax fibre

	Untreated	Degree of acetylation [%]				
		3.6	6	12	18	34
Stable temperature [°C]	319	326	329	334	341	360

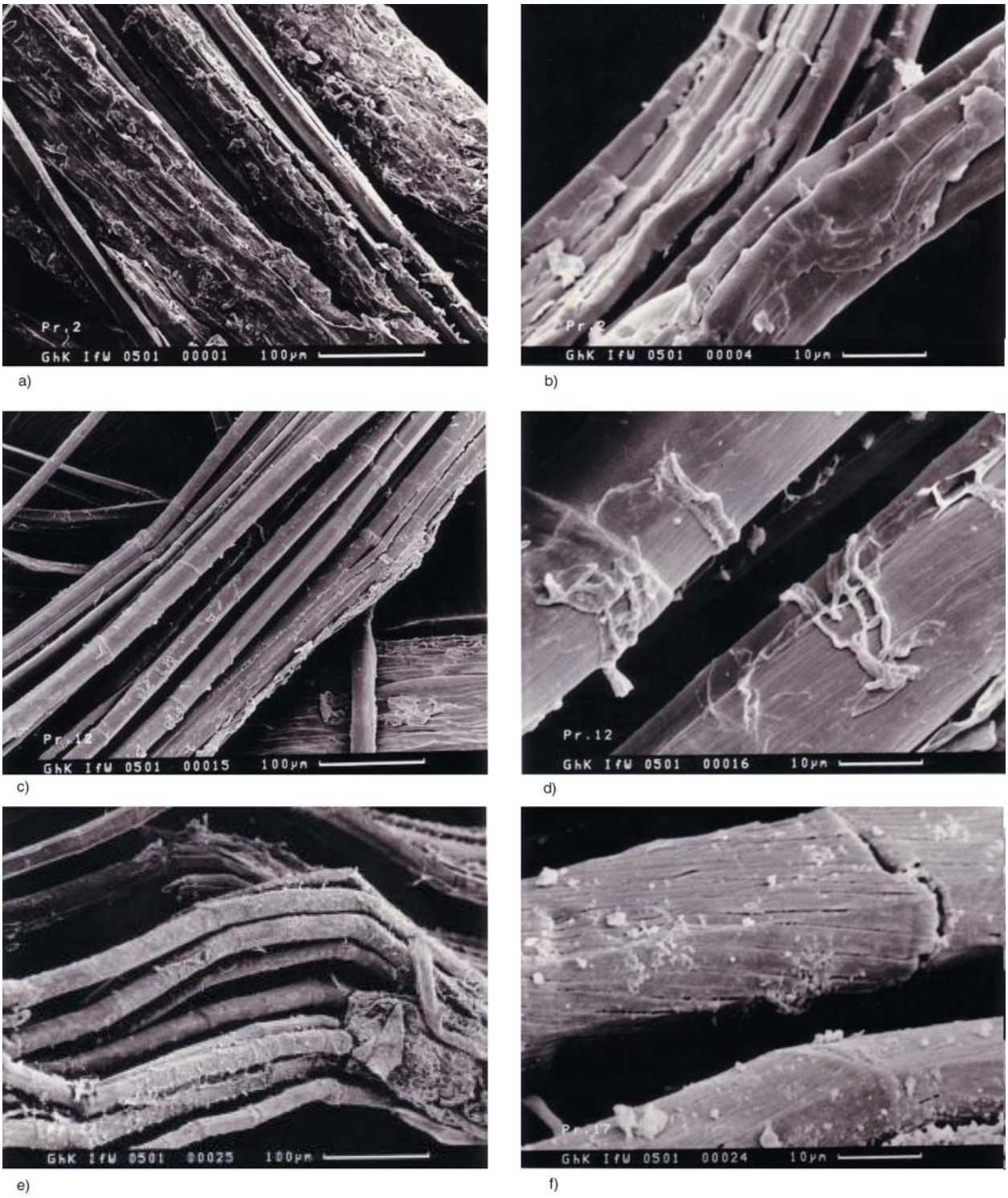

Figure 6. SEM photograph of flax fibre; (6a, 6b) untreated flax fibre surface, (6c, 6d) acetylated flax fibre at degree of acetylation 18% and (6e, 6f) fibre damage at high degree of acetylation

strength of composites were found to increase with increasing degree of acetylation up to 18% and then decreased with further increasing degree of acetylation. The increase in tensile strength could be due to the removal of lignin and extractibles, slight increase in cellulose content and a little portion of hemicellulose converting to acetylated hemicellulose. After 18 % acetylation of flax fibre, the composites tensile strength was found to be decrease swiftly. It could be due to the degradation of cellulose and to the introduction of internal cracks in the fibres. It was also noted that the acetylation of flax fibre removed waxy material from fibre surface, increased fibre-matrix interfacial strength and

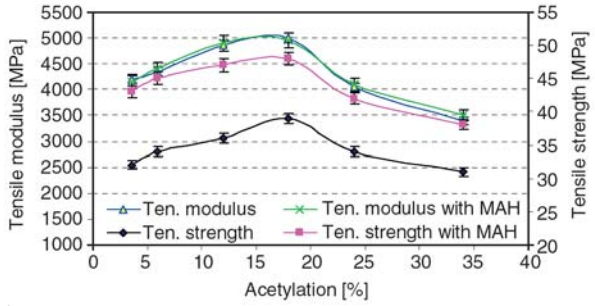

Figure 7. Influence of acetylation of flax fibre on tensile properties of composites

increased surface free energy which are favourable for better properties of composites. With the addition of MAH, the same tendency was observed and the tensile strength of 20 to 35% improvements was observed respect to degree of acetylation. This is due to the formation of ester bonds between fibre and polypropylene.

3.3.2. Flexural properties

Flexural strength is the ability of the material to withstand bending forces applied perpendicular to its longitudinal axis. The stresses induced due to the flexural load are combination of compressive and tensile stresses. For polymeric materials that break easily under flexural load, the specimen is deflected until rupture occurs in outer fibres. The effects of acetylation of flax on the flexural properties are given in Figure 8. The flexural strengths are found to be deliberately increased up to 18% degree of acetylation after that decreased rapidly with increasing degree of acetylation. The flexural modulus was also found to slightly increase up to 18% acetylation and then the property decreased slowly with increasing degree of acetylation. The improvement of flexural properties of treated fibre composites is likely to be due to removal of outer surface; increase cellulose content and effective surface area, increase interfacial adhesion and physical and chemical changes induced by fibre treatment. There is also fibrillation and diameter reduction of flax fibre due to acetylation that may have influence on modulus properties of composites. With increasing degree of acetylation the crack and damage of fibres were observed which may reduce the composites properties after certain range of acetylation. MAH has a positive influence on the flexural strengths and increased 20% maximum because of improvement of interfacial interaction. MAH has also some influence on the flexural modulus but the increase of flexural modulus was not prominent taking into account standard deviation.

3.3.3. Charpy impact properties

The impact strength of a composite is influenced by many factors, including the toughness properties of the reinforcement, the nature of interfacial region and frictional work involved in pulling out the fibre from the matrix. The nature of the interface region is of extreme importance in determining the toughness of the composite.

The notched Charpy impact strength of flax fibre-PP composites with respect to degree of acetytion are presented in Figure 9. The Charpy impact test is a standardized high strain-rate test which determines the amount of energy absorbed by a material during fracture. This absorbed energy is a measure of a given material's toughness and acts as a tool to study brittle-ductile transition [21].

Ray *et al.* [22] observed that, in composites having weak interfacial bonding, the crack propagates along the fibre-matrix interface causing debonding. This leads to significant increase in the energy-absorbing capacity of the composites as a result of

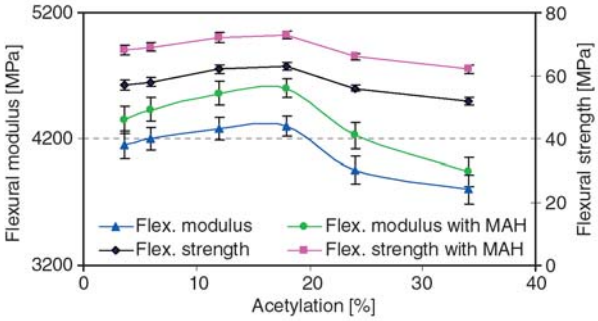

Figure 8. Influence of acetylation of flax fibre on flexural properties of composites

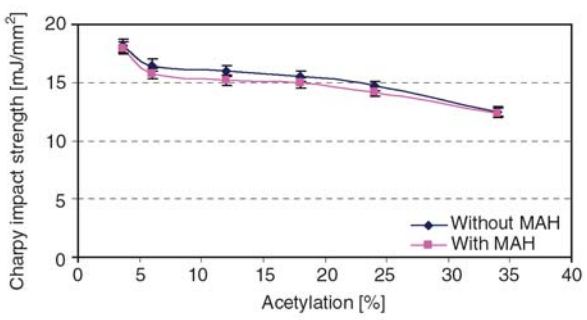

Figure 9. Influence of acetylation of flax fibre on charpy impact strength of composites

the large new surfaces produced and frictional work resulting from differential displacement between matrix and fibre, which increases the impact fatigue resistance of the composites.

It was observed from diagram that the notched Charpy impact strength decreases slowly with increasing acetylation degree which is due to strong interface and decrease in toughness of composite [12]. No significant effect was observed by addition of MAH-PP, moreover impact properties were found to decrease a little bit. This could be explained by brittleness increase of matrix material and local internal deformation in composite material.

4. Conclusions

This study inspected the effect of acetylation of flax fibre on fibre properties and its reinforced polypropylene composites properties.

The following conclusions could be drawn:

- Small amount of catalyst content has a significant effect on reaction rate and degree of acetylation.
- Acetylation of flax fibres resists up to 50% moisture absorption properties depending on degree of acetylation.
- Flax fibre morphology and components have been changed due to acetylation.
- Thermal stability increased till certain range due to acetylation.
- Highest tensile and flexural strength were scrutinized at 18% degree of acetylated flax fibre composites and about 25% improvement on strength properties was observed compare to untreated fibre composites.
- With the addition of MAH, the improvement of tensile strength of composites was observed 20 to 35% considering degree of acetylation.

References

[1] Li X., Tabil L. G., Panigrahi S.: Chemical treatments of natural fiber for use in natural fiber-reinforced composites: A review. Journal of Polymers and the Environment, **15**, 25–33 (2007).

[2] Turmanova S. C., Genieva S. D., Dimitrova A. S., Vlaev L. T.: Non-isothermal degradation kinetics of filled with rise husk ash polypropene composites. Express Polymer Letters, **2**,133–146 (2008).

[3] Mohanty A. K., Misra M., Drzal L. T.: Surface modifications of natural fibers and performance of the resulting biocomposites. Composite Interfaces, **8**, 313–343 (2001).

[4] Bledzki A. K., Sperber V. E., Faruk O.: Natural and wood fibre reinforcement in polymers. Rapra Technology, Chesterfield (2002).

[5] Alvarez V. A., Ruscekaite R. A., Vazquez A. J.: Mechanical properties and water absorption behaviour of composites made from a biodegradable matrix and alkaline treated sisal fibres. Journal of Composite Materials, **37**, 1575–1588 (2003).

[6] Frederick T. W., Norman W.: Natural fibers plastics and composites. Kluwer Academic Publishers, New York (2004).

[7] Rowell R. M., Young R. A., Rowell J. K.: Paper and composites from agro-based resources. CRC press, Boca Raton (1996).

[8] Akin D. E., Gamble G. R., Morrison W. H., Rigsby L. L.: Chemical and structure analysis of fibre and core tissues from flax. Journal of the Science of Food and Agriculture, **72**, 155–165 (1996).

[9] Pizzi A., Eaton A.: The structure of cellulose by conformational analysis. Part 5. Cellulose II water sorption isotherm. Journal of Macromolecular Science, Part A: Pure and Applied Chemistry, **24**, 1065–1084 (1987).

[10] Bledzki A. K., Gassan J.: Composites reinforced with cellulose based fibres. Progress in Polymer Science, **24**, 221–274 (1999).

[11] Sreekala M. S., Thomas S.: Effect of fibre surface modification on water-sorption characteristics of oil palm fibres. Composites Science and Technology, **63**, 861–869 (2003).

[12] Seena J., Koshy P., Thomas S.: The role of interfacial interactions on the mechanical properties of banana fibre reinforced phenol formaldehyde composites. Composite Interfaces, **12**, 581–600 (2005).

[13] Mishra S. B., Luyt A. S.: Effect of organic peroxides on the morphological, thermal and tensile properties of EVA-organoclay nanocomposites. Express Polymer Letters, **2**, 256–264 (2008).

[14] Joseph K., Paul A., Thomas S.: Effect of surface treatments on the electrical properties of low-density polyethylene composites reinforced with short sisal fibres. Composites Science and Technology, **57**, 67–79 (1997).

[15] Mishra S., Misra M., Tripathy S. S., Nayak S. K., Mohanty A. K.: Graft copolymerization of acrylonitrile on chemically modified sisal fibres. Macromolecular Materials and Engineering, **286**, 107–113 (2001).

[16] Lee S. M.: International encyclopaedia of composites, Vol. 4. VHC, New York (1991).

[17] Zafeiropoulos N. E., Williams D. R., Baillie C. A., Matthews F. L.: Development and investigation of surface treatments. Composites, Part A: Applied Science and Manufacturing, **33**, 1083–1093 (2002).

[18] Sjorstrom E.: Wood chemistry: Fundamentals and applications. Academic Press, New York (1981).

[19] Liu F. P., Wolcott M. P., Gardner D. J., Rials G. T.: Characterization of the interface between cellulose fibers and a thermoplastic matrix. Journal of Composite Interfaces, **2**, 419–432 (1994).

[20] Tserki V., Zafeiropoulos N. E., Simon F., Panayiotou C.: A study of the effect of acetylation and propionylation surface treatments on natural fibres. Composites, Part A: Applied Science and Manufacturing, **36**, 1110–1118 (2005).

[21] Bledzki A. K., Mamun A. A., Faruk O.: Abaca fibre reinforced PP composites and comparison with jute and flax fibre composites considering fibre contents. Express Polymer Letters, **1**, 755–762 (2007).

[22] Ray D., Sarkar B. K., Rana A. K., Bose N. R.: The mechanical properties of vinylester resin matrix composites. Composites, Part A: Applied Science and Manufacturing, **32**, 119–127 (2001).

eXPRESS Polymer Letters Vol.2, No.6 (2008) 423–428
Available online at www.expresspolymlett.com
DOI: 10.3144/expresspolymlett.2008.51

Sisal cellulose acetates obtained from heterogeneous reactions

*M. Peres de Paula, T. M. Lacerda, E. Frollini**

Instituto de Química de São Carlos, Universidade de São Paulo; Av. Trabalhador Sãocarlense - 400, CP 780, 13560-970 - São Carlos, São Paulo, Brazil

Received 18 February 2008; accepted in revised form 15 April 2008

Abstract. In the present work, cellulose obtained from sisal, which is a source of rapid growth, was used. Cellulose acetates were produced in heterogeneous medium, using acetic anhydride as esterifying agent and iodine as catalyst, to check if the procedure described in the literature for commercial cellulose also is adequate to sisal cellulose. The results indicated that iodine is an excellent catalyst to obtain sisal cellulose acetates, but the reaction is so fast as described in the literature when, instead of sisal, lower average molar weight cellulose (microcrystalline) is used. The crystallinity index (I_c) of sisal cellulose acetates diminished compared to sisal cellulose, but there was no direct correlation between their degree of substitution (DS) and I_c. Probably acetyl groups were introduced more homogeneously along the short chains of microcrystalline cellulose, when compared to sisal cellulose, and then for microcrystalline cellulose acetates the I_c decreases as DS increases. Using the linear correlation that was found between degree of substitution (DS) and time reaction is possible to control the DS of sisal cellulose acetates, considering a large interval of degrees of substitution (0.3–2.8).

Keywords: *biopolymers, sisal cellulose, cellulose acetates, iodine, catalyst*

1. Introduction

Cellulose can be extracted from several natural sources, as for instance wood, cotton, sisal, sugar cane bagasse and bamboo. In the present study, sisal was used as cellulose source because of its short cultivation period (annual harvest), in contrast to trees from which wood, the main and current source of cellulose, is obtained [1–4]; and also on account of its high cellulose content [2, 3].

The production of cellulose derivatives has extensive interest worldwide, mainly because of its abundance in nature, its biodegradability and its lower environmental impact in comparison with polymers obtained from fossil sources [5]. Among the aspects that demand continuous basic research, the production of cellulose acetate can be cited for its vast industrial application such as textile (clothing and fabrics), high absorbency products (diapers, cigarette filters and other filters), thermoplastics products (films and plastic instruments), nourishing (food packaging), cosmetic and pharmaceutical (extended capsule/tablet release agents and encapsulating agent), medicinal (hypoallergenic surgical products) and others.

Cellulose esterification process basically uses acid anhydrides or acyl chlorides as acetylating agents. Efforts are constantly directed to finding conditions that minimize the time and temperature of reactions and/or lead to better controlling stoichiometry, amid other parameters of reactions. In previous works, our interest addressed the reactions of cellulose in homogeneous medium, involving celluloses from several plant sources (linters, cotton, sisal and

*Corresponding author, e-mail: elisabete@iqsc.usp.br

sugarcane bagasse) [2–4, 6–10] mainly aiming at obtaining acetates.

Cellulose derivatives, as esters, are largely industrially produced in heterogeneous medium. Cellulose esterification process basically uses anhydrides acids or acyl chlorides as acetylating agents. Efforts are continually directed to finding conditions that minimize the time and temperature of reactions and/or lead to better controlling the desired stoichiometry, amid other reaction parameters.

The present paper concerns the preparation of cellulose acetates in heterogeneous medium using iodine as catalyst. The procedure was based on that reported by Biswas *et al.* [11, 12] which is related to acetylation of commercial cellulose, considering short periods of time and using iodine as catalyst. Figure 1 illustrates the mechanism proposed for cellulose acetylation, using iodine as catalyst.

The reaction is supported by the fact that iodine shows great efficiency in catalyzing the esterification of primary and secondary alcohols, as recently demonstrated [13, 14]. This catalyst is resistant to humidity, with no adverse environmental impact and can be recycled.

The purpose of the present study was to evaluate the influence of cellulose properties, such as the average molar mass and crystallinity on the efficiency of this acetylation reaction. Besides sisal cellulose microcrystalline cellulose was used for comparison reasons.

2. Experimental

2.1. Materials

The sisal cellulose was generously provided by Lwarcell (Lençóis Paulista, SP, Brazil) and Avicel PH-101 microcrystalline cellulose, by FMC, Inc. (São Paulo, Brazil).

2.2. Cellulose characterization

The average degree of polymerization (DP) was determined by viscometry, using an Ostwald viscometer, as described elsewhere [9].

Crystallinity index (I_c) was determined by X-ray diffraction, using a VEB CARL ZEISS-JENA URD-6 Universal Diffractometer operating at 40 kV/20 mA and λ (CuK_α) = 1.5406 Å. The crystallinity index was calculated using the Buschle-Diller and Zeronian equation, as described elsewhere [15].

2.3. Cellulose mercerization

Sisal was mercerized in 20% NaOH solution (w/w) at 0°C for 1 h, under stirring, as described in previous work [9].

2.4. Celluloses acetylation

The procedure was based on that described by Biswas and coworkers [12]. 0.5 g of cellulose (sisal or microcrystalline) was suspended in 8.5 ml of acetic anhydride in a glass reactor equipped with mechanic stirring, and reflux condenser. The mixture was heated to 100°C and then 0.05g of iodine was added. At this point, the mixture color turns to dark brown. The intervals of reaction time were varied. At the end of the reaction, the mixture was cooled at room temperature and then 2 ml of saturated solution of sodium thiosulfate was added, in order to neutralize the iodine action. This procedure makes the mixture change to colorless. Thus, 50 ml of ethanol was added and the mixture was stirred for 20 min. The cellulose acetates obtained remained suspended in this medium. Afterward, the mixture was filtered and thoroughly washed with water, dried at room temperature and then at 60°C under vacuum, until constant weight.

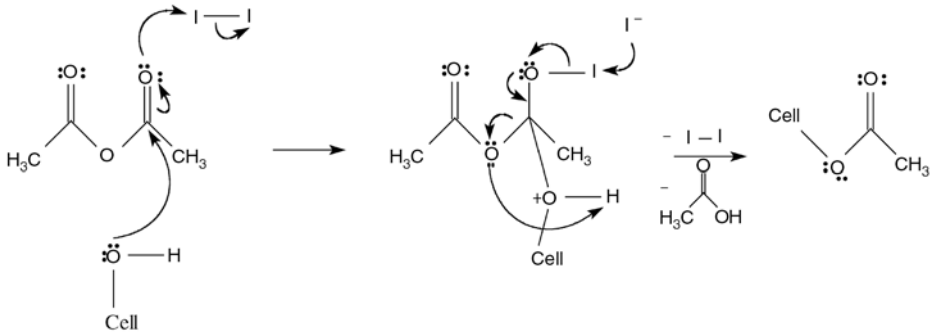

Figure 1. Mechanism of cellulose (Cell–OH) acetylation using iodine as catalyst (based on Biswas *et al.* [11])

2.5. Cellulose acetates characterization

Degree of substitution: the degree of substitution (DS) of cellulose acetates was determined by proton NMR, as described elsewhere [2, 7]. Spectra were recovered with a Brucker AC-200 spectrometer running at 200 MHz and 80°C. The number of scans was about 390. Samples were dissolved in DMSO-d_6 in 5 mm diameter NMR tubes (10 mg/ml). A drop of trifluoracetic acid was added to the sample solution in order to shift the signal of residual water and hydroxyl protons to a lower field outside the spectral region of interest, without affecting the chemical shifts of the glucose ring protons [16].

Infrared spectroscopy: the equipment used was a BOMEM, MB-102 model. The preparation of the pellets was made with 1 mg of the sample added to 100 mg of KBr.

Crystallinity index: X-ray diffraction was used to determine cellulose acetate crystallinity index, following the same conditions used for cellulose.

3. Results and discussions

3.1. Cellulose characterization

Mercerization process alters the fine structure and morphology of the fiber as well as the conformation of the cellulose chains, hence altering the strength and shine of the fiber and its adsorption properties. During this process, the material swells and the polysaccharide chains are rearranged; the amount of less ordered material in the fiber rises, while the crystalline part contracts. These changes result in higher adsorption, given that mercerization increases the specific surface area of the fiber, making the hydroxyl groups of cellulose macromolecules more accessible [8, 17] considered quite important for reactions occurring in heterogeneous medium, as for instance in the present work.

The degree of polymerization (DP) for untreated sisal was 760 and for mercerized sisal 670, indicating that the mercerization process possibly degraded the cellulose chains breaking some of the glycosidic bonds. For microcrystalline cellulose the DP was 126 [7].

The crystallinity index (I_c) results were 77% for untreated sisal and 65% for mercerized sisal, confirming that mercerization causes reduction in cellulose crystallinity, as a diffusion consequence of NaOH into crystalline domains of cellulose, besides rearrangements that can take place in the crystal packing of the chains, as is well known [8, 18]. The I_c for microcrystalline cellulose was 81%.

3.2. Cellulose acetates characterization

The infrared spectra (Figure 2a) confirm the presence of acetyl groups, due to the absorption bands at 1750 cm^{-1} (νC=O), 1375 cm^{-1} (νC–CH_3) and 1235 cm^{-1} (νC–O). The infrared spectra of the other acetates (figures not shown) have a similar profile to the present ones.

Figure 2b shows the NMR spectrum of acetate 11 (Table 1), DS 3.0. The DS values of the cellulose acetates were calculated by means of the ratio between the area corresponding to the proton resonance of the glucose ring (δ ~ 2.90–5.10 ppm) and the corresponding resonance for the methyl protons of the acetate group (δ ~ 1.70–2.20 ppm) [15].

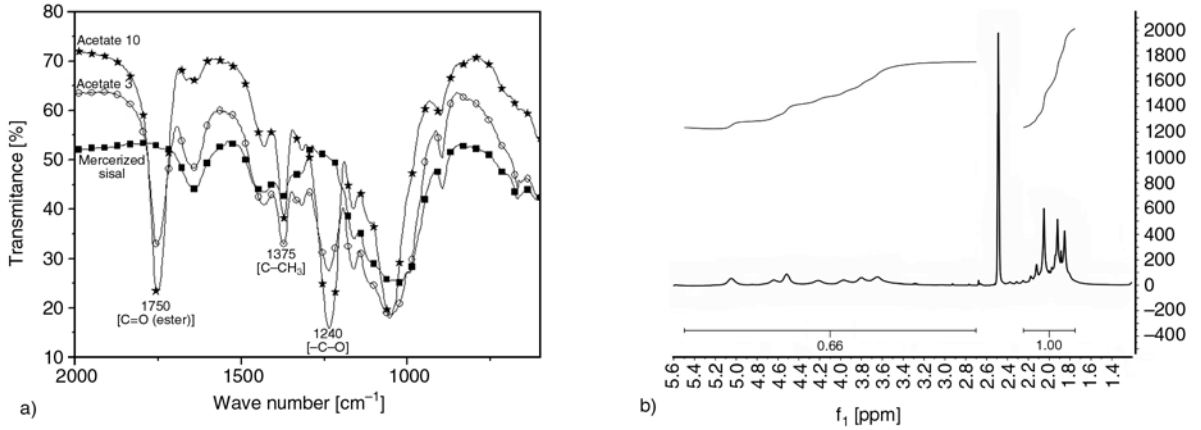

Figure 2. a) Infrared spectra of cellulose and cellulose acetates. Acetate 3 corresponds to DS = 0.5 (reaction time = 30 min; sisal cellulose); acetate 10 corresponds to DS = 2.7 (reaction time = 30 min; microcrystalline cellulose); b) ^{1}H NMR of microcrystalline cellulose acetate (sample 11, DS 3.0)

Other NMR spectra (figures not shown) were similar to that of Figure 2b.

Table 1 presents the reaction time and the corresponding degrees of substitution and crystallinity index (I_c) of the cellulose acetates.

The results (Table 1) show the catalytic effect of iodine, as when there is no catalyst, a very low DS was obtained (0.2, sample 1) for the sisal cellulose, even with a reaction time of 360 min. The presence of iodine led to approximately the same DS with a 10 min reaction (sample 2).

In heterogeneous medium, the accessibility of reagents to hydroxyl groups of the cellulose is dependent on its degree of crystallinity, among other factors. In general lines, the non-crystalline domains are more accessible to reactive agents making the reaction more feasible [8, 16]. The results showed that although mercerized sisal cellulose has less crystalline domains than cellulose microcrystalline, for the same reaction time (compare acetates 2, 3, 4 with 9, 11, 12), microcrystalline cellulose acetylation was considerably faster. This is quite probable due to the typical characteristics of the sisal cellulose, particularly because of its fibrous structure and higher average molar mass [2] that also can influence the accessibility of reagents to hydroxyl groups. Non-fibrous microcrystaline cellulose has organized domains of ca. 100 nm, which is equivalent to the length of a chain of 200 anhydroglucose units, AGU. The penetration of a few reagent molecules into the suspended solid can be sufficient to perturb any long-range structural domains, therefore facilitating the continuity of the reaction. In this case, the DP value plays a more important role than crystallinity. By contrast, fibrous celluloses, as sisal, have high DP and possess organized domains whose length may reach 400 nm. Such celluloses' long chains may be localized either in the non-crystalline or crystalline domains. When compared to microcrystalline cellulose, the destruction of this long-range order is more difficult, this in turn influences the reagents' accessibilities [5, 7].

Table 1. Degree of substitution (DS) and crystallinity index (I_c) of sisal (samples 1–8) and microcrystalline (samples 9–11) cellulose acetates

Acetate sample	Cellulose	Reaction time [min]	DS	I_c [%]
1[a]	Sisal (I_c = 65%)	360	0.2	54
2		10	0.3	54
3		30	0.5	56
4		60	0.9	56
5		90	1.5	63
6		120	1.9	63
7		150	2.3	60
8		180	2.8	58
9	Microcrystalline (I_c = 77%)	10	2.5	73
10		30	2.7	68
11		60	3.0	54

[a]Iodine was not used in this acetylation reaction

Thus, for microcrystalline cellulose, a degree of substitution close to 3.0 is already obtained in a 10 min reaction, while for sisal cellulose the same DS was obtained after 180 min (Table 1). Summarizing, these results show that, in general terms, the lower molar mass of microcrystalline cellulose allied to the fact that this cellulose is not fibered like sisal cellulose, did in fact assist its acetylation. Moreover, it can be considered difficult to eliminate all the hemicellulose in the lignocellulosic fibers, such as wood and sisal, used in the present work. The probable presence of this polysaccharide in sisal cellulose, in spite of the small fraction and considering that the previous mercerization eliminates hemicelluloses, could also exert some influence on the process.

Then, the excellent proposal made by Biswas and collaborators [11, 12] which considers that cellulose acetates with high degrees of substitution can be obtained within short periods of time under iodine catalysis, probably applies easily for not-fibered and low molar mass celluloses. Celluloses from different origins must be studied individually, as for sisal cellulose, studied in the present work. At any rate, iodine proved to be an excellent catalyst for sisal cellulose, as already found by Biswas [11, 12] for other cellulose.

Under the reaction conditions used in the present work, the obtained degree of substitution (DS) for cellulose acetates is linearly correlated with the reaction time (Figure 3), which enables preparing acetates with desired DS using the straight line obtained.

The results show that for sisal cellulose, there is no direct correlation between the degree of substitution (DS) of cellulose acetates and crystallinity index (I_c, Table 1). However, for all reactions, I_c diminished compared to sisal cellulose, in all likelihood due to the higher volume of the acetyl group linked to oxygen, when compared to the hydrogen of hydroxyl groups, which can make difficult the

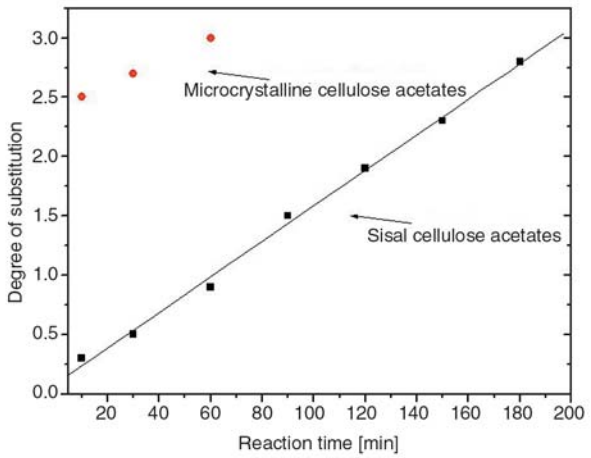

Figure 3. Degree of substitution versus reaction time for sisal and microcrystalline cellulose acetates

packing of chains. For microcrystalline cellulose acetates, the I_c decreases as DS increases (Table 1), probably because acetyl groups were introduced more homogeneously along the short chains, when compared to sisal cellulose, leading then to a certain correlation between the DS values and I_c. However, the interval of DS is too short (2.5–3.0) for definitive conclusions on this subject.

4. Conclusions

The results demonstrate that iodine is an excellent catalyst for the reaction, since in its absence, the degree of acetylation of sisal cellulose is very low, even considering a larger reaction time, when compared to those obtained in the presence of iodine. The reaction is facilitated when lower molar mass and non-fibrous cellulose (microcrystalline) is used, probably due to the easier access of the reagent to the chains. Sisal cellulose acetates were prepared with varying reaction times, leading to products with degrees of substitution within a wide interval (DS between 0.3 and 2.8). Moreover, a linear correlation was observed between DS and reaction time, thus, it is possible to select the necessary conditions to synthesize sisal cellulose acetates with the targeted DS, which is an important finding, considering that cellulose acetates can have different applications, depending on their degree of acetylation.

Acknowledgements

E. F. is grateful to CNPq (National Council of Research, Brazil) for the research productivity fellowship and for financial support, and to FAPESP (The State of São Paulo Research Foundation, Brazil) for financial support.

References

[1] Ass B. A. P., Frollini E.: Aggregation of cellulose during dissolution and acetylation in *N*,*N*-dimethylacetamide/lithium chloride: An introductory study. Anais da Associação Brasileira de Química, **50**, 76–82 (2001).

[2] Ciacco G. T., Ass B. A. P., Ramos L. A., Frollini E.: Acetylation of cellulose under homogeneous reaction conditions. in: 'Natural Polymers and Composites.' (eds.: Mattoso L. H. C., Leão A. L., Frollini E.) EMBRAPA, UNESP, USP, São Paulo, 139–145 (2000).

[3] Marson G. A., El Seoud O. A.: A novel, efficient procedure for acylation of cellulose under homogeneous solution conditions. Journal of Applied Polymer Science, **74**, 1355–1360 (1999).

[4] El Seoud O. A., Marson G. A., Ciacco G. T., Frollini E.: An efficient, one-pot acylation of cellulose under homogeneous reaction conditions. Macromolecular Chemistry and Physics, **201**, 882–889 (2000).

[5] Zhang M. Q.: Polymeric materials from natural resources – Emerging as the times require. Express Polymer Letters, **1**, 406–406 (2007).

[6] El Seoud O. A., Regiani A. M., Frollini E.: Derivatization of cellulose in homogeneous conditions: A brief review. in: 'Natural Polymers and Agrofibers Based Composites' (eds.: Frollini E., Leão A. L., Mattoso L. H. C.) EMBRAPA, UNESP, USP, São Paulo, 73–89 (2000).

[7] Ass B. A. P., Ciacco G. T., Frollini E.: Cellulose acetates from linters and sisal: Correlation between synthesis conditions in DMAc/LiCl and product properties. Bioresource Technology, **96**, 1696–1702 (2005).

[8] Ramos L. A., Assaf M. J., El Seoud A. O., Frollini E.: Influence of the supramolecular structure and physicochemical properties of cellulose on its dissolution in a lithium chloride/*N*,*N*-dimethylacetamide solvent system. Biomacromolecules, **6**, 2638–2647 (2005).

[9] Ass B. A. P., Belgacem M. N., Frollini E.: Mercerized linters cellulose: Characterization and acetylation in *N*,*N*-dimethylacetamide/lithium chloride. Carbohydrate Polymers, **63**, 19–29 (2006).

[10] Castellan A., Ruggiero R., Frollini E., Ramos L. A., Chirat C.: Studies on fluorescence of cellulosics. Holzforschung, **61**, 504–508 (2007).

[11] Biswas A., Shogren R. L., Willet J. L.: Solvent-free process to esterify polysaccharides. Biomacromolecules, **6**, 1843–1845 (2005).

[12] Biswas A., Selling G., Appell M., Woods K. K., Willett J. L., Buchanan C. M.: Iodine catalyzed esterification of cellulose using reduced levels of solvent. Carbohydrate Polymers, **68**, 555–560 (2007).

[13] Mukhopadhyay B., Ravindranathan K. P., Russel D. A., Field R. A.: Streamlined synthesis of per-*O*-acetylated sugars. Glycosyl iodides, or thioglycosides from unprotected reducing sugars. Journal of Organic Chemistry, **69**, 7758–7760 (2004).

[14] Phukan P.: Iodine as an extremely powerful catalyst for the acetylation of alcohols under solvent-free conditions. Tetrahedron Letters, **45**, 4785–4787 (2004).

[15] Buschle-Diller G., Zeronian S. H.: Enhancing the reactivity and strength of cotton fibers. Journal of Applied Polymer Science, **45**, 967–979 (1992).

[16] Edgar K. J., Arnold K. M., Blount W. W., Lawniczak J. E., Lowmann D. W.: Synthesis and properties of cellulose acetoacetates. Macromolecules, **28**, 4122–4128 (1995).

[17] Pušic T., Grancaric A. M., Soljacic I., Ribitsch V.: The effect of mercerisation on the electrokinetic potential of cotton. Journal of the Society of Dyers and Colourists, **115**, 121–124 (1999).

[18] Nishiyama Y., Langan P., Chanzy H.: Crystal structure and hydrogen-bonding system in cellulose I from synchrotron X-ray and neutron fiber diffraction. Journal of American Chemical Society, **124**, 9074–9082 (2002).

eXPRESS Polymer Letters Vol.2, No.6 (2008) 429–439
Available online at www.expresspolymlett.com
DOI: 10.3144/expresspolymlett.2008.52

Oxygen barrier property of polypropylene-polyether treated clay nanocomposite

M. Pannirselvam[1], A. Genovese[2], M. C. Jollands[1], S. N. Bhattacharya[1], R. A. Shanks[2]*

[1]Rheology and Material Processing Centre, School of Civil, Environmental and Chemical Engineering, RMIT University, Melbourne, Australia
[2]School of Applied Sciences, RMIT University, Melbourne, Australia

Received 28 November 2007; accepted in revised form 23 April 2008

Abstract. Polypropylene (PP) nanocomposites were obtained by solution blending of polyether treated montmorillonite and PP, with a coupling agent of maleic anhydride grafted polypropylene (PP-g-MA). The composition of the inorganic clay was varied in 1, 2 and 5 phr (parts of clay per hundred of PP by mass) while films of the composites were obtained via compression molding. Wide-angle X-ray scattering (WAXS) showed nanocomposites in which silicate layers were exfoliated and intercalated with respect to the different clay ratios. The morphology and gas permeability of hybrids prepared with organoclay were compared. Morphological studies using transmission electron microscopy showed most clay layers were dispersed uniformly in the PP matrix. Some tactoids of agglomerated nanoparticles were detected, as clay content increased. The oxygen permeability for all the hybrids for clay loadings were reduced by 30% of the corresponding values for pure PP.

Keywords: *nanocomposites, polyether treated clay, surfactants, oxygen barrier properties, gas tortuous path theory*

1. Introduction

Polypropylene (PP) is one of the fastest growing commercial thermoplastics due to its attractive combination of low density and high heat distortion temperature [1, 2]. There are some limitations in physico-chemical properties that restrict PP applications.

A typical illustration is in packaging, where PP has poor oxygen gas barrier resistance [3, 4]. No single polymer has shown the ideal combination of performance features. PP possesses good water vapour barrier properties, but it is easily permeated by oxygen, carbon dioxide, and hydrocarbons. The necessity of developing more effective barrier polymers has given rise to different strategies to incorporate and optimize the features from several components. Most schemes to improve PP gas barrier properties involve either addition of higher barrier plastics via a multilayer structure (co-extrusion) or by introducing filler with high aspect ratio in the polymer matrix. 1. Co-extrusion allows tailoring of film properties through the use of different materials where each material component maintains its own set of properties, compared with blending of polymers in a mono-extrusion technique. Co-extrusion is used to generate multilayer laminate structures from separately extruded polymer films that are sandwiched together [3, 4]. Resulting films may comprise many layers, such as the PP-adhesive-poly(ethylene-co-vinyl alcohol) (EVOH)-adhesive PP system: EVOH barrier sheet trapped between two layers of moisture resistant PP and two additional adhesive strata. However, by nature co-extrusion is a complex and expensive process.

*Corresponding author, e-mail: muthu.pannirselvam@rmit.edu.au

2. Alternatively, nano-fillers with high aspect ratio can be loaded into the polymer matrix. Polymer nanocomposites are a better choice with significant property increments from clay materials [1–4]. Lange *et al*. mentioned in review that nanocomposite materials are one of the methods for improving gas barrier properties of polyolefins [5]. Recent developments in polymer nanocomposites have attracted attention due to the possibilities offered by this technology to enhance the barrier properties of inexpensive commodity polymers. Many studies have demonstrated improvements in permeability reduction to gases, moisture and organic vapours resulting from the addition of low concentrations of layered clay nanoparticles to various thermoplastic matrices [6–8]. Nanoparticles have been shown to influence the properties of the polymers at low volume fractions [9]. This is mainly due to their nanometer scale particle size and intraparticle distances. The desired properties are usually reached at low filler volume fraction, allowing the nanocomposites to retain macroscopic dispersion and low density of the polymer. The geometrical shape of the particle plays an important role in determining the properties of the composites [10]. There is 40% reduction in oxygen permeability upon the incorporation of 4%·vol organoclay into polyethylene, as reported by Osman *et al*. [8, 9]. Avella *et al.* suggested that the calcium carbonate nanoparticles drastically reduced the permeability of oxygen and carbon dioxide for PP nanocomposites [11]. Yano *et al.* obtained a 10-fold reduction in the water vapour permeability coefficient of a polyimide containing 2% wt mica nanoparticles in comparison with the unfilled polymers [12]. The improved nanocomposite barrier behaviour illustrated by these examples has been explained by the tortuous path model, in which the presence of impermeable clay platelets generates an overlapped structure that hinders penetrant diffusion and thus decreases the permeability of the material [3, 10].

2. Benefits and challenges with smectite clays

Of all dioctahedral smectities, montmorillonite (MMT) is mainly used in nanocomposites. The choice of MMT as a sorbent of organic compounds is influenced by its large surface area to mass (760 m^2/g), its high cation exchange capacity, largely independent of salt concentrations and pH, and the relative ease by which it forms an interlayer complex with a wide variety of organic molecules [13, 14]. Dimorphic clays are formed by condensation in a 1:1 proportion and trimorphic clays (three sheets) are formed by 2:1 condensation, with the octahedral sheet being sandwiched between two sheets of inward-pointing tetrahedra. The challenge with montomorillonite clay is its incompatibility with organic polymers. The silicate layers of the clay are 'incompatible' with organic polymers, due to surface hydroxyl groups; the smectite clays are usually treated to make them hydrophobic by ion-exchange of the sodium interlayer cations with long-chain alkyammonium cations [2, 15]. Instability of ammonium salts at temperatures encountered in melt mixing greater than 200°C leads to discolouration of the polymer matrix [2, 16, 17]. Hoffmann elimination can occur under basic conditions; for instance in the presence of sodium hydroxide, quaternary ammonium salts decompose by Hoffmann elimination, yielding the corresponding trialkyl amine and an alkene [16–18, 26] (Figure 1). Crown ethers and cryptands are more expensive than all other intercalants; however they are stable under higher temperatures up to 200°C [19]. Poly(ethylene glycol) (PEG) is more stable than quaternary ammonium salts, but of lower activity. Polyether compounds as intercalants can act as ligands of these interlayer sodium cations, giving rise to stable complexes. PEG treated clay is thermally stable to 327°C in an inert atmosphere and 275°C in air [20–22]. These above mentioned advantages appeal to the use of poly(ethylene glycol) monolau-

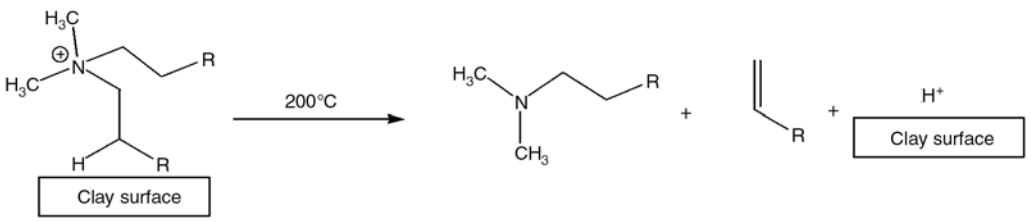

Figure 1. Mechanism of Hoffmann degradation in organoclays

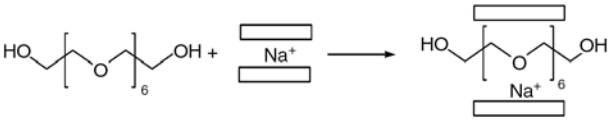

Figure 2. Mechanism of intercalation of poly(ethylene glycol) with sodium montmorillonite

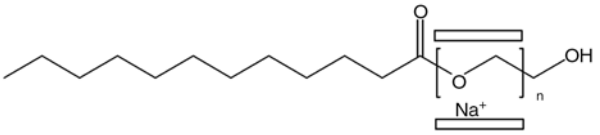

Figure 3. Product of reaction between poly(ethylene glycol) monolaurate and untreated clay

rate (PEG-ML) as an alternative intercalant, to conventional alkyl amine chain for surface treatment of clay. In this research, montmorillonite clay was treated with PEG-ML. Treated clay provided increased d-spacing (1.82 nm) that resulted from complexation between PEG oxygen atoms and sodium ions between the clay platelets (Figure 2).

Clay was treated with various intercalants that provided different d-spacing. The added advantage of treating clay with PEG-ML was its long alkyl chain (Figure 3) that could interact with PP. The effect of reinforcement of PP by layered silicate was determined by at least two important factors: clay dispersion (exfoliation or intercalation) and interaction between clay and PP. Many researchers mentioned that it is difficult for PP or other polyolefins to adhere to polar materials [2, 10, 23]. Interfacial agents play an important role in overcoming this difficulty. In order to overcome this challenge in trial experiments with this treated clay, maleic anhydride grafted polypropylene (PP-g-MA) was used as a compatibilizer [24]. PP-g-MA reacted with –OH groups on the clay surface, increasing the compatibility between clay and PP. The aim of this research is to synthesize PP nanocomposites with PEG-ML treated clay, using a solution blending technique. Oxygen barrier of the nanocomposites and pure PP were compared, in addition to structural characterization to validate the dispersion of clay layers in polymer matrix.

3. Experimental

3.1. Treatment of clay with poly(ethylene glycol) monolaurate

Sodium montmorillonite (Na^+ –MMT) was purchased from Southern Clay Products, Texas, USA. Cation exchange capacity of the clay was 92.6 meq/100 g clay. Poly(ethylene glycol) (M_n = 400 g/mol) monolaurate were purchased from Sigma-Aldrich Chemicals and used as received. Clay was preheated in vacuum oven for 8 h at 70°C for removal of moisture [26]. The nature of solvents is critical to facilitate the insertion of organic materials (in this case: PEG-ML between the silicate layers, the polarity of the medium being a determining factor for intercalations. Preheated clay was dispersed in water at 3% concentration and heated to 75°C for 3 h [19, 25]. The amount of intercalant was calculated according to cation exchange capacity of Na^+ –MMT (cation exchange capacity of clay = 92.6 meq/100 g of clay). After careful addition of intercalants, the contents of the beaker were heated to 70°C for 3 h. The contents were cooled and filtered under vacuum. The filter cake was vacuum dried at 60°C and then the intercalated clay was dried in oven. The dried clay was ground using a mortar and pestle for uniformity in grain size. The treated clay was analysed using wide-angle X-ray scattering (WAXS) and thermogravimetry (TG). Results of WAXS and TG are reported elsewhere [26].

3.2. Preparation of nanocomposites

Clay treated with PEG-ML was added to PP as filler. Clay treated with PEG 400 monolaurate is abbreviated as PEGC. PP {M_w = 250 000 g/mol, T_m = 167°C, density = 0.905 g/cm^3 (ASTM D1505), MFI = 11 dg/min (ASTM D1238)} were obtained from Basell Australia. PP-g-MA {T_m = 152°C, 0.6% wt MA} was supplied by Sigma–Aldrich chemicals. All chemicals and polymers used in this research were commercial products and they were used as received without further purification. The preparation of the nanocomposites was carried out by a solution blending method using o-xylene [27–29]. The amount of treated clay added was 1, 2 and 5 parts per hundred (phr) of the total weight of PP and PP-g-MA. The process of preparation of nanocomposites can be divided into the following three steps:

Step 1: Dispersion of PEGC in o-xylene in order to minimize agglomeration of clay layers and cluster formation. Calculated amounts of treated clay were added to 50 ml of o-xylene solution. This solution was sonicated using a probe sonicator (High Inten-

Table 1. Proportion of PP, PP-g-MA (as compatiblizer), and PEGC for the preparation of nanocomposites

Identification	PP [%·wt]	PP-g-MA [%·wt]	Clay [phr]
PP	100	–	–
PP-PEGC1	90	10	1
PP-PEGC2	90	10	2
PP-PEGC5	90	10	5

sity Ultrasonic Processor, Model: GEX 500) to induce an efficient dispersion of nanoclay.

Step 2: The PP and compatibilizer PP-g-MA were dissolved in o-xylene, composition reported in Table 1. This mixture was stirred continuously for 6 h until the PP dissolved.

Step 3: Thorough dispersion of the solutions prepared in the first and second stages of this process were performed using an Ultraturrax high-shear disperser. The dispersion was carried out at 150°C for 10 min. The product was separated by precipitation in cold methanol. The contents were allowed to dry over night. Finally the material was dried in vacuum oven overnight, to completely remove o-xylene and methanol.

3.3. Composite moulding and annealing

Pure PP and PP nanocomposites sheets were compression moulded between steel plates covered with thin Mylar sheets using a hot press at 200°C for 5 min. The sheets for the barrier performance tests as well as the composites for structural studies were obtained from the above-mentioned method. Cold circulated water was used to cool the platens to ambient temperature while full pressure was maintained. The average thickness of the composites was 1.5 mm for wide-angle X-ray scattering (WAXS) and Transmission Electron Microscopy (TEM) studies, and 0.5 mm for oxygen permeability tests. Peterlin *et al.* have observed that in polyethylene, tortuosity factor increases on annealing at elevated temperatures, despite an increase in crystallinity [30]. Similar results were observed by other authors [31–33]. Kastura *et al.* suggested that on annealing PP, there was a reduction of volume due to increased density [23]. Crystallization can be considered to be associated with the formation of thick lamellas with a high concentration of intralamellar imperfections. The presence of intralamellar defects or voids within the lamellar boundaries will lead to an increase in permeability. In order to standardize the effect of crystallisation on the permeability and to reduce the defects within the lamellar boundaries, all nanocomposites (including pure PP film) studied in this research were annealed at higher temperature. Oxygen permeability test sheets were annealed at 75°C for 8 h and kept at room temperature for 24 h in order to increase the crystallinity.

3.4. Wide-angle X-ray scattering

WAXS is one the methods for characterising the state of intercalation and exfoliation of clay gallery layers [2, 10, 16]. X-ray data on the treated clay composites was collected on a Bruker AXS D8 Advance wide-angle X-ray diffraction instrument at 45 kV and 30 mA. The composite was mounted in a flat-plate specimen holder with exposed surface flattened with a glass microscope slide. Diffraction patterns were measured using a scintillation detector. Scans were taken between 2 and 25° at a speed of 1°/min, a step size of 0.05° and step time of 3 s [26].

3.5. Transmission electron microscopy

The second most common technique for morphological characterisation of nanocomposites is TEM [2, 10, 16]. TEM technique is widely used to study and assess the dispersion of clay in the PP matrix [11, 17]. TEM images were obtained via a Philips CM200UT (FEI Co., Hillsboro, OR) operated at a voltage of 80 kV. The hot pressed films described previously were embedded in an epoxy compound (dried in vacuum oven at 60°C, for 24 h). The embedded films were then thinly sliced (~100 nm) using RMC MTX ultramicrotome (UMT, Boeckeler Instrument Inc., Tucson, AZ). The thickness of the thin slice was automatically controlled to be about 50 nm by ultramicrotome. The thin slice obtained was collected onto a 300 mesh copper grid. Finally, the specimens were characterized by TEM.

3.6. Oxygen permeability measurements

The device employed was a Mocon Ox-Tran 2/21 manufactured by Modern Controls Inc. The method was based on ASTM standard D3985 [1, 3]. It has been widely used to analyse the gas barrier proper-

ties of polymer films [9, 10, 25]. The Modern Controls Inc (Mocon) technical manual explained that Mocon Ox-Tran 2/21 system uses a patented coulometric sensor (coulox) to detect oxygen transmission through both flat materials and packages [34]. The coulox sensor is an intrinsic or absolute sensor that does not require calibration, however the instrument requires calibration using standards provided. The instrument was calibrated at 23°C with National Institute of Standards and Technology (NIST) certified Mylar films of known transport characteristics. A continuous flow of gas was maintained on both sides of the barrier material. Initially nitrogen gas was passed over both surfaces to remove oxygen from the film. The nitrogen on one side was then replaced by oxygen, and the nitrogen flow on the other side then swept the surface to extract any oxygen that diffused through the material. The diffusing oxygen was measured by a detector that is sensitive specifically to oxygen. PP and PP nanocomposites were measured only after checking the accuracy of the standards. Flat films were clamped into the diffusion cell that was purged of residual oxygen using an oxygen-free air carrier gas. The carrier gas was routed to the sensor until a stable zero was established. Pure (99.9%) oxygen was then introduced into the outside chamber of the diffusion cell. Molecules of oxygen diffusing through the film to the inside chamber were conveyed to the sensor by the carrier gas. The test sheets were laminated between two aluminium foil masks to reduce the area of exposure from 100 to 5.4 cm^2. Measurements were conducted at 23°C and 0% RH. Three different films were tested for each proportion of clay.

3.7. Gas tortuous theory

According to this theory, the impermeable inorganic filler in the relatively permeable polymer matrix will create a tortuous path for the diffusing molecules [3, 10, 31, 35, 36]. As a result, the filled polymer demonstrated reduced gas permeability, with the permeability being determined using the Equation (1):

$$\frac{P_f}{P_u} = \frac{\phi_p}{\left[1+\left(\frac{L}{2W}\right)\phi_f\right]} \tag{1}$$

where P_f and P_u are the permeability of the filled and unfilled polymer, ϕ_p and ϕ_f are the volume fraction of the polymer and filler, and L/W is the aspect ratio of the filler. An inverse relationship between aspect ratio of the filler and permeability of the filled polymer exists [3, 10]. An increase in aspect ratio of the filler corresponds to a decrease in the permeability of the filled polymer. Compared with most inorganic fillers, silicate layers of montmorillonite have high aspect ratio. The thickness of a single layer of montmorillonite is of the order of a nanometer, while the length is in the range 200–500 nm. When the layered silicate is fully exfoliated in the polymer matrix, greatly reduced gas permeability can be achieved (Figure 4). So in order to reduce the gas permeability of PP nanocomposite, it is important to exfoliate the silicate layers into PP matrix. However, if the exfoliation of the silicate is not optimal, there will still be reduction in permeability; even increased permeability has been observed in some extreme cases [2].

4. Results and discussion

4.1. Structural morphology

Figure 5 displays the diffraction pattern of pure PP and patterns for 1, 2 and 5 phr clay reinforced PP nanocomposites, respectively. Six films were characterized for each clay proportion in order to obtain

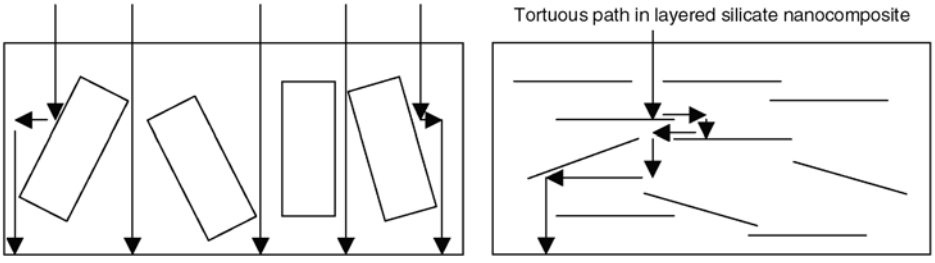

Figure 4. Schematic representation of gas permeation through conventional microcomposite (left) and layered silicate nanocomposite (right)

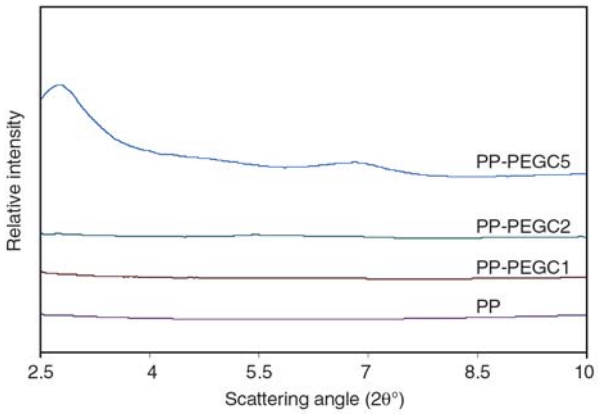

Figure 5. WAXS pattern of pure PP and PP nanocomposites

representative morphological features of the PP and clay state. Of all the six patterns obtained from each composite, the data with maximum intensity and peak formation is shown here. This was to obtain representative view on the composite morphological characteristics and to evaluate attainment of exfoliation (diffraction pattern is featureless in clay sensitive region) or intercalation in the low scattering angle region of 2.5 to 5.5°.

In the current system PEG-ML was used as intercalate for the clay. PEG-ML had molecular weight (M_n = 400 g/mol) that is capable of entering the silicate galleries as demonstrated in Figure 3. The scattering pattern for 1 and 2 phr ratios indicate an exfoliated structure was obtained for the treated clay. This is attributed to the treatment facilitating PP insertion into the silicate galleries promoting delamination of the periodic layered structure of the clay. The phase morphology was correlated with the structure observed by TEM. Figures 6 and 7 show the 1 and 2 phr nanocomposites. The image shows individual silicate layers of thickness in the order of a nanometer with aspect ratio in the range of 100 to 250 nm. The exfoliated morphology was due to a lower filler concentration, high-shear dispersion and compatibilization with PP-g-MA. In the ultimate platelet configuration, the clay was completely dispersed and fully exfoliated, resulting in the specific surface at its maximum. This has been achieved for the 1 and 2 phr nanocomposites. Varela *et al.* suggested that greatest extent of exfoliation was obtained with 40%·wt PP-g-MA, where MA promoted exfoliated morphologies consisting of individual nanometer thick silicate layers suspended in PP matrix (penetration of PP chains

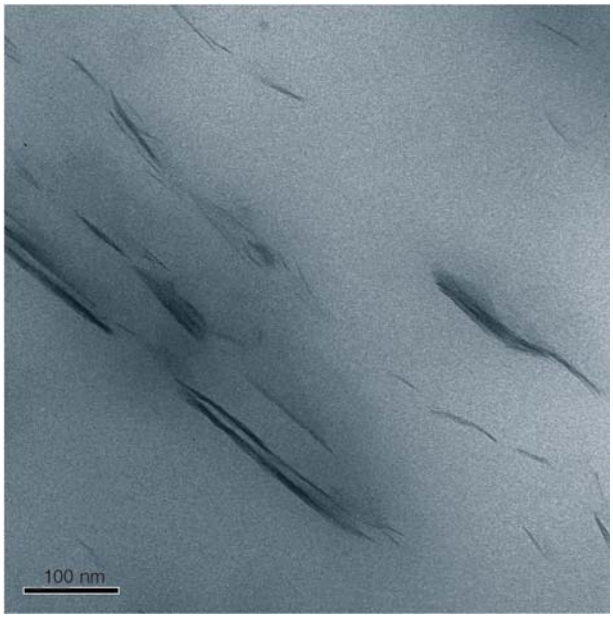

Figure 6. TEM patterns of polypropylene nanocomposites with 1 phr clay

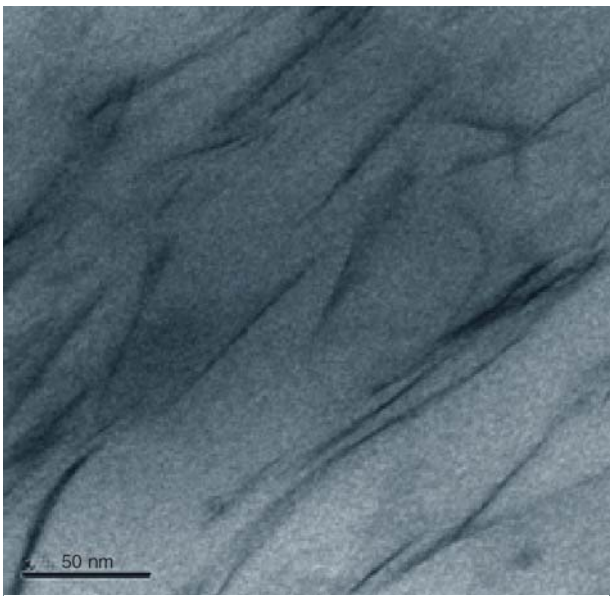

Figure 7. TEM pattern of polypropylene nanocomposites with 2 phr clay

within and delamination of the crystallites) [37]. The interaction between PP and PEGC treated clay was expected to be due to the presence of the long alkyl chain of PEGC and PP-g-MA. A lower (001) diffraction signal intensity was related to a higher extent of platelet exfoliation that occurred during synthesis and processing of the nanocomposite. Sinha Ray *et al.* suggested that polymer intercalation proceeded from the primary clay particle edges towards the particle center [10]. Complete nanolayer separation required favourable polymer-clay

interactions to overcome the penalty of polymer confinement.

At higher clay loading of 5 phr, a small peak was present at 5.5° in the diffraction pattern that was due to the attainment of intercalation rather than exfoliation of clay layers (Figure 5). TEM shows the complex morphological features of the clay state. The appearance of individual clay layers is evident, but there are regions containing platelets that have not separated giving rise to a periodicity in structure and hence a diffraction peak. Although the specimens were prepared with solvent, with ultrasonication to facilitate the intercalation, full exfoliation was not achieved. It was noted that the mass transport of highly viscous resin into the clay galleries presents a limitation. This step is considered as one of the important limiting factors for clay platelet separation. In addition, the relative amount of clay platelet separation and aggregation depended on the mixing technique and surfactant used for modifying the clay. In the case of the 5 phr composite, a combination of effects gave rise to the observed structure, such as limited intercalation at a relatively high content of clay, shearing facilitation to disrupt larger agglomerates and overcome incompatibility of clay tactoids. The size of clay lamella observed for PEG-dispersed PP nanocomposite was a reasonable match for the size dimension obtained previously in TEM studies of nanocomposites [16, 38, 39]. Figures 6 and 7 show the exfoliated lamellae, tactoids composed of a variable number of lamella and aggregates of tactoids. Clay ratios (1 and 2 phr) showed more uniform distribution of silicate layer without clay aggregates. Higher magnification (100 nm) clearly displays that clay layers are homogeneously dispersed in the PP matrix, except for 5 phr clay ratios. For 5 phr clay ratio, the intercalated silicate layers are locally stacked to a hundred nanometres in thickness and from several hundred nanometres to more than one micrometer in length [39]. The aspect ratio of clay inclusions can be inferred from the length and thickness of the dark lines in TEM micrographs at different magnifications. Most clay particles were well dispersed in PP matrix, which was due to good compatibility between PP, PP-g-MA and end alkyl chain of treated clay (monolaurate chain of PEG). Avella *et al.* prepared exfoliated PP based nanocomposites by solution blending [40], similarly from their observations, exfoliation of clay layers

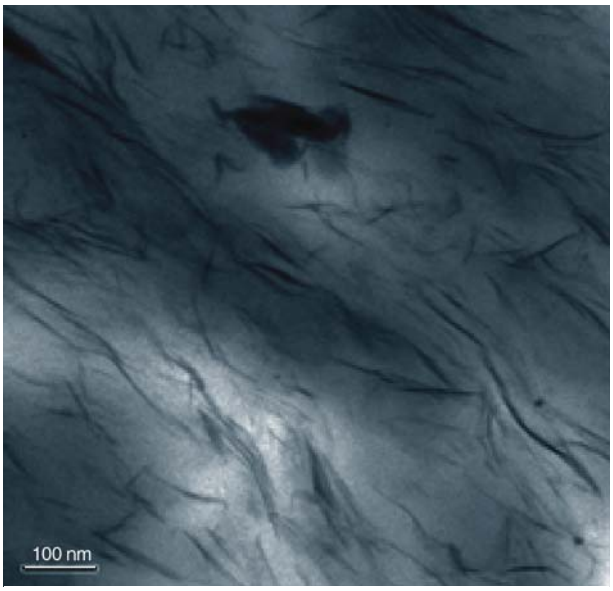

Figure 8. TEM pattern of polypropylene nanocomposites with 5 phr clay

in nanocomposites occurred only at 1 and 3% wt of clay loading, not at 5% wt clay. In the 5% wt nanocomposites (Figure 8). Some clay layers collapsed leading to a tactoid system. Sinha Ray *et al*. suggested that polymer intercalation proceeded from the primary clay particle edges towards particle centres [10]. Mass transport into the primary particles was found to be the limiting step for nanocomposite formation, the degree of constituent mixing was critical for rapid nanocomposite formation. Shear processing, such as with an ultrasonicator, parallel plate rheometer, conventional compounding equipment, high-shear mixer, decrease the nanocomposite formation time by disruption of primary particles and establishment of composite uniformity. Ultraturrax mixing was sufficient to disperse the clay layers. From our previous study utilizing a polyether of higher molecular weight (M_n = 600 g/mol) for clay treatment prior to preparation of nanocomposites using solution blending, we obtained exfoliated structure with 1, 2 and 5 phr clay ratios [39].

Mass transport into the primary particles was found to be a limiting step for nanocomposite formation, with the degree of constituent mixing being critical for rapid nanocomposite formation. Shear processing with ultrasonication or conventional compounding equipment will decrease the nanocomposite formation time by disruption of primary particles and establishing composite uniformity [10]. Disappearance of peaks in clay PP composites sug-

gests two conclusions: 1. Exfoliation – separation of clay lamella into individual clay layers. 2. Agglomeration – clustering of clay gallery layers, undisturbed by shearing action. Moad *et al.* suggested that the clay layers exfoliated in the presence of PEO based surfactants in the preparation of PP nanocomposites [16]. The authors melt intercalated untreated clay with PEO based surfactants for preparation of PP nanocomposites. Shearing action of the extruder assisted exfoliation of clay layers without use of compatibilizer. Chiu *et al.* suggested that Cloisite 30B filled polymer nanocomposites will not exfoliate with PP-g-MA because of the higher polarity of Cloisite 30B [41]. The same authors demonstrated exfoliation with poly(styrene-co-maleic-anhydride) (PS-g-MA) oligomer as compatibilizer instead of PP-g-MA. The higher polarity of PS-g-MA resulted in exfoliation. Clay interlayer expansion depends on compatibility between polymer and organic intercalant and interactions between the two phases [24]. MMT clay is composed of regularly arranged tactoids and galleries. The length of an organic modifier (in this case: the long alkyl chain of monolaurate) and CEC are two parameters that determine how the chains pack between the silicate layers. Montmorillonite has both surface and edge charges [2]. The charges on the edges are easily accessible to modification, but they do not accomplish much improvement in interlaminar separation. These sites represent an opportunity for attachment of functional groups such as maleic anhydride. PP-g-MA increased both the compatibility and chemical interaction between the polymer and treated clay. This was a reason for exfoliation of clay lamella. Ultraturrax high-shear dispersion and PP-g-MA compatibilizer addition along with long alkyl chain for compatibility with PP were reasons for exfoliation of clay layers in the PP matrix. Ultraturrax high-shear dispersion lead to exfoliation of the clay layers, for researchers elsewhere [42, 43].

4.2. Oxygen permeability

Nanocomposites are a multiphase system in which the coexistence of phases with different sorption and diffusion can cause complex transport phenomena [35]. Montmorillonite gives rise to superficial adsorption and specific interactions with some gases and solvents [10, 40]. The presence of silicate layers are expected to cause a decrease in permeability of oxygen because of more tortuous paths for the diffusing molecules that must bypass impenetrable platelets (Figure 4). This phenomenon is significant when the filler is of nanometer size with high aspect ratio. Avella *et al.* suggested that nanofillers (calcium carbonate) reduce the permeability to both oxygen and carbon dioxide, and claimed that the nanofillers were responsible for higher barrier properties improvement [11]. It should be noted that nano-sized calcium carbonate are spherical in shape. MMT clay layers can be exfoliated or delaminated into nanometer platelets with a thickness of about 1 nm and an aspect ratio of 100–1500 and surface areas of 700–800 m^2/g. Each platelet has high strength and stiffness and can be regarded as a rigid inorganic polymer whose molecular weight (10^8 g/mol) is much greater than that of typical polymers. Therefore, low fractions of clays are required to achieve equivalent properties compared with conventional composites (calcium carbonate). It was deduced that with increasing clay content in a nanocomposites, the permeability of gases was reduced. This was the case for the composites in this research.

Table 2 lists the oxygen permeability for nanocomposites while Figure 9 graphically shows the permeability versus clay content. It can be seen that the permeability of oxygen decreased with increase in clay ratio. The 1 phr composition showed marginal reduction (~3%), but 2 phr reduced permeability about 20% compared with the PP matrix. The oxygen permeability of 5 phr clay composite reduced by almost 30%. The clay layers themselves are impervious to oxygen, providing barrier resistance. The volume occupied by the clay and amount of clay influenced the actual three-dimensional arrangement and dispersion. At low concentrations, permeability decrease was not significant indicating there was insufficient platelets to provide resistance to permeability and the torturous path required. The permeability depended on the aspect

Table 2. Oxygen permeability values for PP- PEGC treated clay nanocomposites

PEGC [phr]	Oxygen permeability [$cm^3 \cdot mm/m^2 \cdot day \cdot atm$]				Standard deviation
	Sample 1	Sample 2	Sample 3	Average	
1	90.0	91.1	89.9	90.2	0.8
2	74.0	71.4	75.2	73.5	1.9
5	65.1	70.9	69.8	68.6	3.1

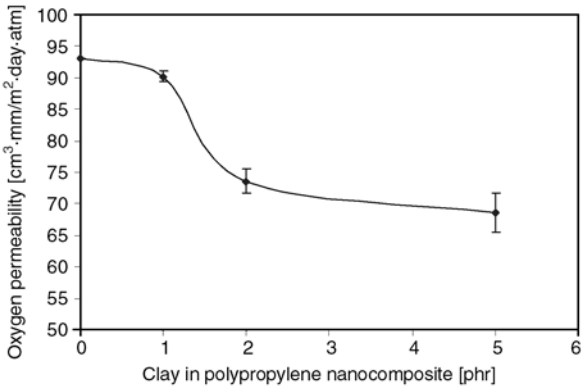

Figure 9. Oxygen permeability of polypropylene nanocomposites with 1, 2 and 5 phr clay

ratio of the clay layers. Dispersion of clay ranged from intercalation, exfoliation and agglomeration of clay layers at 5 phr clay loadings. The effects of nano-filler in a polymer material depend principally on six factors; 1. properties relative to the polymer, 2. concentration (volume fraction), 3. size distribution, 4. shape and distribution of shapes and 5. degree of dispersion 6. adhesion to the polymer matrix. Since there are a number of factors to assess for a polymer nanocomposite, barrier property enhancement in nanocomposites can be applied to validate the dispersion of fillers in a polymer matrix [44]. The change in oxygen permeability of nanocomposites was controlled by the clay content and microstructure. Tactoids at low clay ratios (1 and 2 phr) exfoliated better than those at high clay ratio (5 phr). The deviation of oxygen permeability increased with clay ratios, indirectly supported by the WAXS and TEM results. Lohfink *et al.* suggested that the oxygen permeability of PP-g-MA was greater than pure PP [45], although it should be noted that 10% of PP-g-MA was present in their nanocomposites.

5. Conclusions

The aim was to obtain MMT with a modified surface featuring hydrophobicity and increased affinity with PP. The prospect of developing layered silicates such as MMT as a multifunctional additive for PP at less than 5% wt was satisfactory using solution blending. Nanocomposites prepared using PEG-ML treated clay in ratios of 1, 2 phr exfoliated well in a matrix of PP blended with PP-g-MA, with an exception of agglomerate formation for 5 phr clay loading. Diffraction patterns suggested exfoliation of clay layers in the PP nanocomposites. The diffraction patterns cannot be used alone to adequately describe nanoscale dispersion of the layered silicate. Interpretation of the structure and clay state was validated with morphological observation using TEM. The actual nanoscale dispersion and overall global dispersion of the clay in PP was revealed and nanocomposites with low loading (1 and 2 phr) formed exfoliated clay layers. The 5 phr clay composition, revealed that clay layers dispersed uniformly in the matrix, although some clusters or agglomerated particles were detected leading to the diffraction peaks observed using WAXS. These clusters could be due to clay undisturbed by high-shear dispersion. Clay dispersion increased the barrier properties by creating a tortuous path to limit the progress of oxygen molecules through the PP matrix. While a low loading 1 phr showed an exfoliated structure, the amount was not sufficient to adequately reduce the oxygen permeability. The 2 phr provided improved resistance by increasing the barriers for oxygen molecules to diffuse around. This suggested a threshold was obtained with exfoliated structures. At 5 phr, the conditions employed to prepare the nanocomposites or the volume fraction of clay particles was insufficient to allow efficient exfoliation and dispersion of the clay. Oxygen permeability for hybrids with clay loadings to 5 phr was less than the corresponding values for pure PP, indicating that platelet structure and dispersion were important in obtaining permeability reduction.

Acknowledgements

Authors would like to thank Mr. Ashfaqar Rahaman, Mr. Frank Antolasic, Mr. Karl Lang, Ms. Nadia Zartack, and Dr. Mohammed Al Kobaisi of RMIT University for their valuable suggestions.

References

[1] Massey L.: Permeability properties of plastics and elastomers. William Andrew Publishing/Plastics Design Library, New York (2003).

[2] Utracki L. A., Sepehr M., Boccaleri E.: Synthetic, layered nanoparticles for polymeric nanocomposites (PNCs). Polymers for Advanced Technologies, **18**, 1–37 (2007).

[3] Karian H. G.: Handbook of polypropylene and polypropylene composites. Marcel Dekker, New York (2003).

[4] Vasile C.: Handbook of polyolefins. Marcel Dekker, New York (2000).
[5] Lange J., Wyser Y.: Recent innovations in barrier technologies for plastic packaging- A review. Packaging Technology and Science, **16**, 149–158 (2003).
[6] Osborn K. R., Jenkins W. A.: Plastic films: Technology and packaging applications. CRC Press, Boca Raton (1992).
[7] Faisant J., Ait-Kadi A., Bousmina M., Deschenes L.: Morphology, thermomechanical and barrier properties of polypropylene-ethylene vinyl alcohol blends. Polymer, **39**, 533–545 (1998).
[8] Osman M. A., Mittal V., Lusti H. R.: The aspect ratio and gas permeation in polymer-layered silicate nanocomposites. Macromolecular Rapid Communications, **25**, 1145–1149 (2004).
[9] Osman M. A., Atallah A.: High-density polyethylene micro- and nanocomposites: Effect of particle shape, size and surface treatment on polymer crystallinity and gas permeability. Macromolecular Rapid Communications, **25**, 1540–1544 (2004).
[10] Sinha Ray S., Okamoto M.: Polymer/layered silicate nanocomposites: A review from preparation to processing. Progress in Polymer Science, **28**, 1539–1641 (2003).
[11] Avella M., Cosco S., Di Lorenzo M., Di Pace E., Gentile G., Errico M.: iPP based nanocomposites filled with calcium carbonate nanoparticles: Structure/properties relationships. Macromolecular Symposia, **234**, 156–162 (2006).
[12] Yano K., Usuki A., Okada A.: Synthesis and properties of polyimide-clay hybrid films. Journal of Polymer Science, Part A: Polymer Chemistry, **35**, 2289–2294 (1997).
[13] Grim R. E.: Clay mineralogy. McGraw-Hill, New York (1953).
[14] Theng B. K. G.: The Chemistry of clay-organic reactions. John Wiley and Sons, New York (1974).
[15] Ton-That T-M., Perrin-Sarazin F., Cole K. C., Bureau M. N., Denault J.: Polyolefin nanocomposites: Formulation and development. Polymer Engineering and Science, **44**, 1212–1219 (2004).
[16] Moad G., Dean K., Edmond L., Kukaleva N., Li G., Mayadunne R. T. A., Pfaendner R., Schneider A., Simon G. P., Wermter H.: Non-ionic, poly(ethylene oxide)-based surfactants as intercalants/dispersants/exfoliants for poly(propylene)-clay nanocomposites. Macromolecular Materials and Engineering, **291**, 37–52 (2006).
[17] Kooli F., Magusin P. C. M. M.: Adsorption of cetyltrimethylammonium ions on an acid-activated smectite and their thermal stability. Clay Minerals, **40**, 233–243 (2005).
[18] Pannirselvam M., Gupta R. K., Shanks R. A., Bhattacharya S. N.: Polypropylene clay nanocomposites prepared with polyether intercalated clay. in 'Proceedings of PPS-23, El Savador, Brazil', paper number: 087 (2007).
[19] Yao H., Zhu J., Morgan A. B., Wilkie C. A.: Crown ether-modified clays and their polystyrene nanocomposites. Polymer Engineering and Science, **42**, 1808–1814 (2002).
[20] Aranda P., Ruiz-Hitzky E.: Poly (ethylene oxide)-silicate intercalation materials. Chemistry of Materials, **4**, 1395–1403 (1992).
[21] Ruiz-Hitzky E., Aranda P.: Polymer-salt intercalation complexes in layer silicates. Advanced Materials, **2**, 545–547 (1990).
[22] Tunney J. J., Detellier C.: Aluminosilicate nanocomposite materials. Poly(ethylene glycol)-kaolinite intercalates. Chemistry of Materials, **8**, 927–935 (1996).
[23] Katsura T., Kamal M. R., Utracki L. A.: Some properties of polypropylene filled with metal fibers. Polymer Composites, **6**, 282–295 (1985).
[24] Velasco J. I., Ardanuy M., Realinho V., Antunes A. I., Fernández J. I., González-Peña M. A., Rodríguez-Pérez J. A.: Polypropylene/clay nanocomposites: Combined effects of clay treatment and compatibilizer polymers on the structure and properties. Journal of Applied Polymer Science, **102**, 1213–1223 (2006).
[25] Leuteritz A., Pospiech D., Kretzschmar B., Willeke M., Jehnichen D., Jentzsch U., Grundke K., Janke A.: Progress in polypropylene nanocomposite development. Advanced Engineering Materials, **5**, 678–681 (2003).
[26] Pannirselvam M., Gupta R. K., Bhattacharya S. N., Shanks R. A.: Intercalation of montmorillonite by interlayer adsorption and complex formation. Advance Materials Research, **29–30**, 295–298 (2007).
[27] Lee E. C., Mielewski D. F., Baird R. J.: Exfoliation and dispersion enhancement in polypropylene nanocomposites by in-situ melt phase ultrasonication. Polymer Engineering and Science, **44**, 1773–1782 (2004).
[28] Zhang Y-Q., Lee J-H., Jang H-J., Nah C-W.: Preparing PP/clay nanocomposites using a swelling agent. Composites, Part B: Engineering, **35**, 133–138 (2004).
[29] Manias E., Touny A., Wu L., Strawhecker K., Lu B., Chung T. C.: Polypropylene/montmorillonite nanocomposites. Review of the synthetic routes and materials properties. Chemistry of Materials, **13**, 3516–3523 (2001).
[30] Peterlin A.: Dependence of diffusive transport on morphology of crystalline polymers. Journal of Macromolecular Science, Part B: Physics, **11**, 57–87 (1975).
[31] Vieth W.: Diffusion in and through polymers: Principles and applications. Hanser, New York (1991).
[32] Vittoria V., Perullo A.: Effect of quenching temperature on the structure of isotactic polypropylene films. Journal of Macromolecular Science, Part B: Physics, **25**, 267–281 (1986).
[33] Vieth W., Wuerth W. F.: Transport properties and their correlation with the morphology of thermally conditioned polypropylene. Journal of Applied Polymer Science, **13**, 685–712 (1969).
[34] Modern Controls Inc.: Technical manual for Ox-Tran, **2/21**, 1–11 (2006).

[35] Gorrasi G., Tammaro L., Mariarosaria T., Vittoria V., Kaempfer D., Reichert P., Mülhaupt R.: Transport properties of organic vapors in nanocomposites of isotactic polypropylene. Journal of Polymer Science, Part B: Polymer Physics, **41**, 1798–1805 (2003).

[36] Meille S., Bruckner S., Porzio W.: Isotactic polypropylene. A structure with nonparallel chain axes. Macromolecules, **23**, 4114–4121 (1990).

[37] Varela C. R., Rosales C., Perera R., Matos M., Poirier T., Blunda A., Rojas H.: Functionalized polypropylenes in the compatibilization and dispersion of clay nanocomposites. Polymer Composites, **27**, 451–460 (2006).

[38] Pannirselvam M., Gupta R. K., Shanks R. A., Bhattacharya S. N.: Synthesis of a novel compatibilizer for polypropylene clay nanocomposites. in 'Proceedings of Chemeca-2007, Melbourne, Australia', 1705–1711 (2007).

[39] Pannirselvam M., Ivanov I., Shanks R. A., Bhattacharya S. N.: Composition and mechanical properties of polypropylene polyether treated clay nanocomposites. in 'Proceedings of Chemeca-2007, Melbourne, Australia', 130–135 (2007).

[40] Avella M., Simona C., Gaetano D. V., Errico M. E.: Crystallization behavior and properties of exfoliated isotactic polypropylene/organoclay nanocomposites. Advances in Polymer Technology, **24**, 132–144 (2005).

[41] Chiu F-C., Lai S-M., Chen J-W., Chu J-W.: Combined effects of clay modifications and compatibilizers on the formation and physical properties of melt-mixed polypropylene/clay nanocomposites. Journal of Polymer Science, Part B: Polymer Physics, **42**, 4139–4150 (2004).

[42] Rhoney I., Brown S., Hudson N. E., Pethrick R. A.: Influence of processing method on the exfoliation process for organically modified clay systems. I. Polyurethanes. Journal of Applied Polymer Science, **91**, 1335–1343 (2004).

[43] IJdo W. L., Kemnetz S., Benderly D.: An infrared method to assess organoclay delamination and orientation in organoclay polymer nanocomposites. Polymer Engineering and Science, **46**, 1031–1039 (2006).

[44] Bhattacharya S. N., Gupta R. K., Kamal M. R.: Polymer nanocomposites: Theory and practice. Hanser Gardner, Munich (2007).

[45] Lohfink G. W., Kamal M. R.: Morphology and permeability in extruded polypropylene/ethylene vinyl-alcohol copolymer blends. Polymer Engineering and Science, **33**, 1404–1420 (1993).

eXPRESS Polymer Letters Vol.2, No.6 (2008) 440–448
Available online at www.expresspolymlett.com
DOI: 10.3144/expresspolymlett.2008.53

Synthesis of a series of soluble main-chain chiral nonracemic poly(alkyl-aryl ketone)

P. Wei[1], *D. Wang*[1], *Z. Wu*[1], *X. Bi*[2*]

[1]Department of Chemistry, University of Missouri-Kansas City, Kansas City, MO 64110, USA
[2]Department of Physical Sciences, Charleston Southern University, Charleston, SC 29406, USA

Received 5 March 2008; accepted in revised form 26 April 2008

Abstract. A series of main-chain chiral polyketones have been synthesized through condensation polymerization of a dihalide and a diketone with optically pure binaphthyl moiety as linkage in the polymer backbone. The solubility of the polymers can be easily enhanced by substituents at the alpha position next to the carbonyl groups. Reducing the steric hindrance of the substituents in the monomers increases the reactivity of the polymerization. The chiral polymers exhibit large optical rotations. Circular Dichroism (CD) spectra of the polymers are similar to those of the corresponding monomers. The novel synthetic strategy may have great impact on future development of palladium catalyzed condensation polymerizations. The highly soluble chiral polymers synthesized allow for preparation of materials in the form of thin films and have potentials applications in various areas such as chiral separation and recognition.

Keywords: *polymer synthesis, molecular engineering, main-chain chiral polyketone, polycondensation*

1. Introduction

Main-chain chiral polymers are of great interest because of their important applications in chiral separation and recognition [1–4]. In order to achieve such goals materials must be stable and possess functional groups. Considerable attention has been focused on the synthesis of optically active polymers with chirality in the main-chain because the polymers typically exist or have the tendency to form helical and rigid-rod configuration, which offers enhanced capability in chiral applications [5–8]. Although it has constantly been great synthetic challenges in constructing main-chain chiral polymers, there are a number of strategies developed to build chirality into the polymer backbones. These include the polymerization of chiral monomers and asymmetric polymerization of achiral monomers using chiral catalysts [3, 9–16]. The asymmetric polymerization requires a careful design of catalysts and laborious screening for the right chiral ligands. Direct polymerization of chiral monomers usually results in polymers of decreased processibility, which has been overcome by attaching long alkyl substituents [5, 6]. The drawback is the alteration of rheological behavior of the polymers.

Polyketones are a class of high performance materials that have attracted a great deal of attention due to their high thermal stability, which is a result of the incorporation of thermally stable carbonyl and/or aromatic groups in the polymer backbones [17–19]. These polymers typically exhibit high glass transition temperatures and high melting points [17], which makes them ideal candidates for use as stationary phase in chromatography applications. Aromatic polyketones are synthesized by Friedel-Crafts or nucleophilic aromatic substitution reactions [20–25]. The materials are usually insolu-

*Corresponding author, e-mail: xbi@csuniv.edu

ble and intractable. Aliphatic polyketones have been prepared through the copolymerization of carbon monoxide with ethylene or α-olefins [9, 26–29]. Previously we have developed a new polymerization route for the construction of aromatic alkyl polyketones using palladium phosphine complexes [30]. To further extend our research in new polymer synthesis, we have developed the strategy of synthesizing main-chain chiral polyketones using palladium catalyzed condensation polymerization. The chirality of the polyketone main chain is achieved by utilizing chiral binaphthyl moiety, which has been previously reported as chiral monomer for other polymer synthesis [31–37]. The synthesized chiral polyketones have been extensively characterized by ^{1}H and ^{13}C NMR, gel permeation chromatography (GPC), polarimeter, UV-Vis spectrometry and circular dichroism (CD). To the best our knowledge, this is the first time that soluble main-chain chiral aliphatic aromatic polyketones are reported.

2. Experimental section

2.1. Materials and methods

Solvents (hexane, benzene, diethyl ether) were predried using 3 Å molecular sieves, degassed and stirred over benzophenone ketyl. The dried and degassed solvents were vacuum-transferred into a flame-dried flask equipped with a Teflon valve and stored under N_2. Other solvents were distilled from either CaH_2 or P_2O_5 before use. All the chemicals used were purchased from either the Aldrich Chemical Company or ACROS Organics. Optically pure binaphthol was resolved according to literature procedures [38]. Optical rotation was measured on a Rudolph Autopol III polarimeter and a JASCO-J-720 circular dichroism spectroscopy. ^{1}H NMR spectra were measured with a Bruker AM 250 (250 MHz) spectrometer. ^{13}C NMR spectra were recorded at 62.9 MHz on a Brucker AM 250 spectrometer. Molecular weights were determined by gel permeation chromatography (GPC) equipped with a Waters 410-differential refractometer. A flow rate of 1.0 ml/min was used and samples were prepared in THF. Polystyrene standards were used for calibration.

2.2. Synthesis

*Synthesis of (R)-(+)-6,6′-dibromo-2,2′-dihydroxy-1,1′-binaphthyl (**1**)*

This compound was synthesized in 97.5% yield (mp 208–209°C) from optically pure (*R*)-(+)-2,2′-dihydroxy-1,1′-binaphthyl following a reported procedure [39]. Characterizations by ^{1}H NMR are consistent with reported data.

*Synthesis of (R)-(+)-6,6′-dibromo-2,2′-dimethoxy-1,1′-binaphthyl (**2**)*

(*R*)-(+)-6,6′-dibromo-2,2′-dihydroxy-1,1′-binaphthyl (3.99 g, 8.49 mmol) and anhydrous K_2CO_3 (3.5 g, 27.3 mmol) were added in dry CH_3CN (50 ml) followed by a slow addition of CH_3I (1.56 ml, 25 mmol). The mixture was refluxed for two days and cooled to room temperature before poured into 200 ml of water. The mixture was filtered and recrystallized from methylene chloride-benzene (1:1 mixture) to give the desired product (3.8 g, yield 89.5%). ^{1}H NMR ($CDCl_3$): δ 4.12 (s, OCH_3, 6 H), 7.30 (d, 2 H), 7.64 (d, 2 H), 7.83 (d, 2 H), 8.26 (d, 2 H), 8.36 (s, 2 H). ^{13}C NMR ($CDCl_3$): δ 56.62, 114.8, 117.3, 118.9, 126.8, 128.7, 129.7, 129.8, 130.1, 132.3, 155.1.

*Synthesis of (R)-(+)-6,6′-diiodo-2,2′-dimethoxy-binaphthyl (**3**)*

A solution of (*R*)-(+)-6,6′-dibromo-2,2′-dimethoxy-binaphthol (4.72 g, 0.01 mol) and KI (16.6 g, 0.1 mol) in DMF (80 ml) was prepared and brought to reflux. While the solution was still warm, $NiBr_2$ (1.4 g, 6.48 mmol) and tri-*n*-butyl phosphine (1.0 ml, 4.0 mmol) was added. Refluxing was continued overnight. Upon cooling, the solution was diluted with 200 ml of benzene, and washed with several portions of water and dried over $MgSO_4$. The solvent was evaporated and the solid was recrystallized thrice from CH_2Cl_2/Et_2O solvent mixture (1:1) to give a yellowish powder (yield 78%). ^{1}H NMR ($CDCl_3$): δ 4.11 (s, OCH_3, 6 H), 7.30 (d, 2 H), 7.63 (d, 2 H), 7.83 (d, 2 H), 8.25 (d, 2 H), 8.36 (s, 2 H). ^{13}C NMR ($CDCl_3$): δ 56.9, 88.8, 114.9, 119.1, 127.1, 128.9, 131.0, 132.9, 135.1, 136.8, 155.5. Element analysis: Calculated: C 46.67%, H 2.85%. Found: C 46.23%, H 2.82%.

*Synthesis of (R)-(–)-6,6′-dipropionoyl-2,2′-dimethoxy-1,1′-binaphthyl (**4**)*

To a Schlenk flask was charged with (*R*)-(+)-6,6′-dibromo-2,2′-dimethoxy-1,1′-binaphthyl (1.89 g, 4.0 mmol) and dry THF (50 ml). The solution was cooled to –78°C in a dry ice-acetone bath and a hexane solution of BuLi (1.6 M, 5.52 ml, 8.8 mmol) was added slowly. After the mixture was stirred for 2 hours, N,N′-dimethylpropionamide (1.1 ml, 10 mmol) was added dropwise via a syringe. The solution was allowed to warm to room temperature overnight and was quenched by adding 10% HCl (50 ml) solution. The organic layer was separated, dried over $MgSO_4$ and evaporated. The residue was purified by flash chromatography on silica gel using benzene-ethyl acetate (15:1) as eluent to give pure product 0.935 g (yield 54.9%). ^{1}H NMR ($CDCl_3$): δ 1.27 (t, CH_3, 6 H), 3.09 (q, CH_2, 4 H), 3.81 (s, OCH_3, 6 H), 7.13 (d, 2 H), 7.55 (d, 2 H), 7.81 (d, 2 H), 8.16 (d, 2 H), 8.55 (s, 2 H). ^{13}C NMR ($CDCl_3$): δ 8.6, 31.9, 56.7, 114.5, 118.9, 124.7, 125.5, 128.2, 130.2, 131.8, 132.3, 136.3, 157.1, 200.8. Element analysis: Calculated: C 78.85%, H 6.14% Found: C 78.43%, H 6.05%.

*Synthesis of (S)-(–)-2,2′-dimethoxy-1,1′-binaphthyl (**5**)*

The optically pure (*S*)-(–)-2,2′-dimethoxy-1,1′-binaphthyl was prepared by the reaction of (*S*)-(–)-2,2′-dihydroxy-1,1′-binaphthyl with CH_3I using the similar procedure as described in the preparation of (*R*)-(+)-6,6′-dibromo-2,2′-dimethoxy-1,1′-binaphthyl.

*Synthesis of (S)-(–)-3,3′-dipropionoyl-2,2′-dimethoxy-1,1′-binaphthyl (**7**)*

To a Schlenk flask was charged with (*S*)-(–)-2,2′-dimethoxy-1,1′-binaphthyl (1.57 g, 5 mmol), TMEDA (1.6 ml, 10.5 mmol) and dry ether (75 ml). A hexane solution of *n*-butyl lithium (1.6 M, 7.1 ml, 11.3 mmol) was added dropwise. The mixture was stirred for 3 hours at room temperature, and cooled to –78°C. Propionaldehyde (1.04 ml, 15 mmol) was added over a period of 10 minutes. The solution was stirred for 2 hr at –78°C and then warmed to room temperature and stirred for another 3 hours. The reaction was quenched by addition of an aqueous solution of HCl (10%). After evaporating the solvent, the residue was redissolved in acetone (50 ml), and Jones reagent was added dropwise into the solution. The color changed from red to green and then to red again. The reaction was stopped when the red color persisted. Evaporating the solvent gave an oil-like substance. The material was purified using flash chromatography on silica gel using dichloromethane-hexane (3:1, with 1% ethyl acetate) as eluent to give a white crystal 0.965 g (yield 45%). ^{1}H NMR ($CDCl_3$): δ 1.27 (t, CH_3, 6 H), 3.14 (q, CH_2, 4 H), 3.39 (s, OCH_3, 6 H), 7.14 (d, 2 H), 7.33 (t, 2 H), 7.45 (t, 2 H), 7.98 (d, 2 H), 8.19 (d, 2 H). ^{13}C NMR ($CDCl_3$) δ 8.9, 36.7, 62.2, 125.4, 125.8, 125.9, 128.5, 129.5, 130.2, 130.9, 134.4, 135.6, 153.9, 205.3. Element analysis: Calculated: C 78.85%, H 6.14% Found: C 78.68%, H 6.15%.

*Synthesis of (S)-(+)-6,6′-dipropionoyl-2,2′-dimethoxy-1,1′-binaphthyl (**8**)*

This compound was prepared from commercial (*S*)-(+)-6,6′-dibromo-2,2′-dimethoxy-1,1′-binaphthyl (steoroisomer of **2**) following the same procedures as described in compound **4**. The ^{1}H NMR and ^{13}C NMR characterization resembles that for **4**.

General procedure for the polymerization

To an oven-dried flask equipped with a Teflon valve containing a spin-bar was charged with $Pd(OAc)_2$ (6.7 mg, 0.0299 mmol), P(*t*-Bu)$_3$ (3.3 mg, 0.0163 mmol) and *t*-BuONa (100 mg, 1.04 mmol). The Schlenk tube was degassed and refilled with nitrogen. Arene dihalide (0.5 mmol), diketone (0.5 mmol) and THF (2 ml) were added. The resulting mixture was heated under nitrogen to 70°C for 24 hr. The mixture was cooled to room temperature and precipitated into methanol. The polymer obtained was redissolved in THF and reprecipitated several times to yield an off-white powder. The yields range from 60–92%. **Poly-(*R*)-(+)-9** and **poly-(*R*)-(–)-10** were synthesized by the reaction of **4** with 1,4-phenylene and 4,4′-biphenylene, respectively. **Poly-(*S*)-(+)-11** and **poly-(*S*)-(–)-12** were synthesized by the reaction of **7** with 1,4-phenylene and 4,4′-biphenylene, respectively. **Poly-(*R*)-(+)-9**. ^{1}H NMR ($CDCl_3$): δ 1.47 (CH_3, 6 H), 3.70 (OCH_3, 6 H), 4.75 (CH, 2 H), 6.99–8.49 (H–Ar, 14 H). ^{13}C NMR ($CDCl_3$): δ 19.8, 47.2, 56.7, 114.3, 118.7,

125.4, 128.1, 128.6, 131.3, 131.8, 132.0, 136.2, 140.3, 157.2, 200.2. **Poly-(*R*)-(–)-10**. ^{1}H NMR ($CDCl_3$): δ 1.57 (CH3, 6 H), 3.71 (OCH_3, 6 H), 4.82 (CH, 2 H), 7.03–8.55 (H–Ar, 18 H). ^{13}C NMR ($CDCl_3$): δ 19.6, 47.2, 56.4, 114.1, 118.5, 125.2, 127.5, 127.8, 128.1, 131.0, 131.5, 131.7, 135.9, 139.1, 140.6, 156.9, 199.8. **Poly-(*S*)-(+)-11**. ^{1}H NMR ($CDCl_3$): δ 1.54 (CH_3, 6 H), 3.25 (OCH_3, m, 6 H), 4.69 (CH, 2 H), 6.90–8.19 (H–Ar, 14 H). **Poly-(*S*)-(–)-12**. ^{1}H NMR (CDCl3): δ 1.62 (CH_3, 6 H), 3.25 (OCH_3, m, 6 H), 4.81 (CH, 2 H), 6.98–8.19 (H–Ar, 18 H). ^{13}C NMR ($CDCl_3$): δ 18.6, 51.8, 62.4, 124.8, 125.2, 125.7, 127.3, 128.3, 128.9, 129.4, 130.0, 131.1, 134.3, 135.3, 139.4, 140.0, 153.4, 205.2. **Poly-(*S*)-(+)-10** was synthesized by reaction of 8 with 4,4′-biphenylene with the ^{1}H NMR characterization the same as for **poly-(*R*)-(–)-10**.

3. Results and discussion

Previously a facile synthesis of polyketones by cross-coupling condensation polymerization has been reported by our research group [30]. To further synthesize optically-active chiral polyketones, the initial attempt involved the reaction of (*R*)-(+)-6,6′-dibromo-2,2′-dimethoxy-1,1′-binaphthyl (**2**) with 1,4-diacetylbenzene under the reported cross-coupling conditions. The reaction took place readily to yield a solid which was insoluble in any organic solvents. Therefore, it has been difficult to process and characterize the resulted polymer using solution techniques. We reasoned that the infusibility might be attributed to the rigid polymer backbone structures. In order to prepare soluble chiral polyketones, a model reaction of compound **2** with 1,4-dipentanoylbenzene (Figure 2) was conducted and surprisingly the resulting polymer product was completely soluble in common organic solvents including methylene chloride, chloroform, THF and DMF. We believed that the solubility was enhanced by the asymmetric center introduced in the polymer backbone. The structures of the polymers were studied by ^{1}H NMR spectroscopy. The peaks at δ 4.75 ppm in ^{1}H NMR and at δ 200 ppm in ^{13}C NMR corresponded to methine and carbonyl resonances in the polymer, respectively. The molecular weight of the polymers was however low as revealed by GPC (M_w = 7900). It was speculated that the low molecular weight might associate with the relative low oxidative addition activity of carbon-bromide bond with palladium complexes. To test this thought, a further experiment was carried out by polymerization of 1,4-dipentanoylbenzene with 6,6′-diiodo-2,2′-dimethoxy-1,1′-binaphthyl (**3**), which was synthesized with 83% yield by nickel-catalyzed exchange reaction of **2** with KI following a reported procedure [40] (Figure 1). The

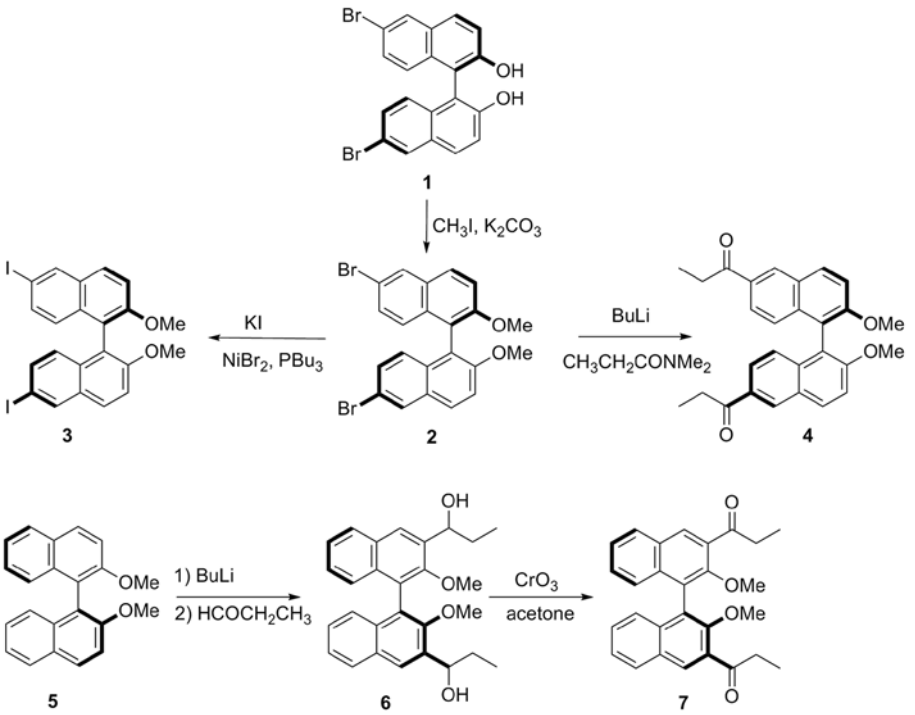

Figure 1. Synthesis of optically active monomers

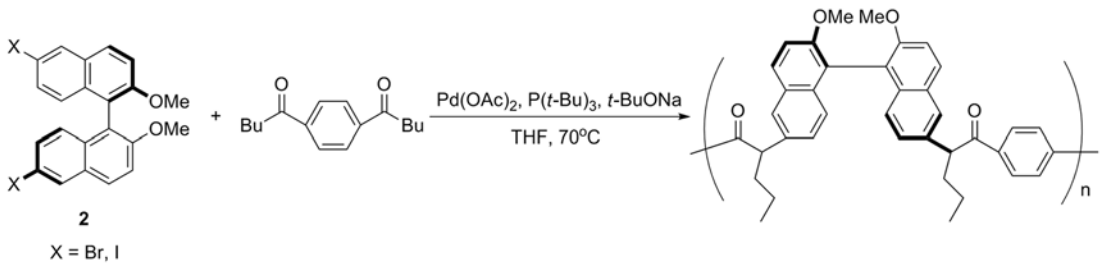

Figure 2. Palladium catalyzed polymerization of **2** with 1,4-dipentanoylbenzene

product can be easily isolated and purified by recrystallization. The substitution of both bromides by iodides was confirmed by the disappearance of quaternary aromatic carbon resonance next to the bromide at δ 117.3 ppm and the appearance of a peak at 88.8 ppm corresponding to the quaternary aromatic carbon resonance adjacent to iodide in ^{13}C NMR spectra. The driving force for such a reaction is the formation of thermodynamically more stable KBr. Indeed, the condensation polymerization of **3** and 1,4-dipentanoylbenzene yielded polymers with slightly higher molecular weights (M_w = 8900).

By studying the structures of the monomers, it was noticed that compounds **2** and **3** possessed sterically bulky binaphthyl rings, which might hamper the subsequent displacement of the bromides or iodides in the intermediates formed from the oxidative addition of palladium complexes. To reduce the steric hindrance, we looked into the polymerization of (*R*)-(+)-6,6′-dialkanoyl-2,2′-dimethoxy-1,1′-binaphthyl (**4**) with 1,4-dihalobenzene or 4,4′-dihalobiphenyl, where the alkanoyl groups were directly connected onto the binaphthyl rings and the halides were attached to the less hindered phenyl groups. Compound **4** was synthesized in good yield by first treating **2** with BuLi to generate 6,6′-dilithio-2,2′-dimethoxy-1,1′-binaphthyl, which further reacted with N,N-dimethylpropionamide. The products were characterized by both ^{1}H and ^{13}C NMR spectroscopy. The polymerization was carried out by condensation reaction of **4** and 1,4-dibromobenzene to yield main-chain chiral polymers (Figure 3). A significant increase in the molecular weight was observed (Table 1). This supports our rationale that steric hindrance has

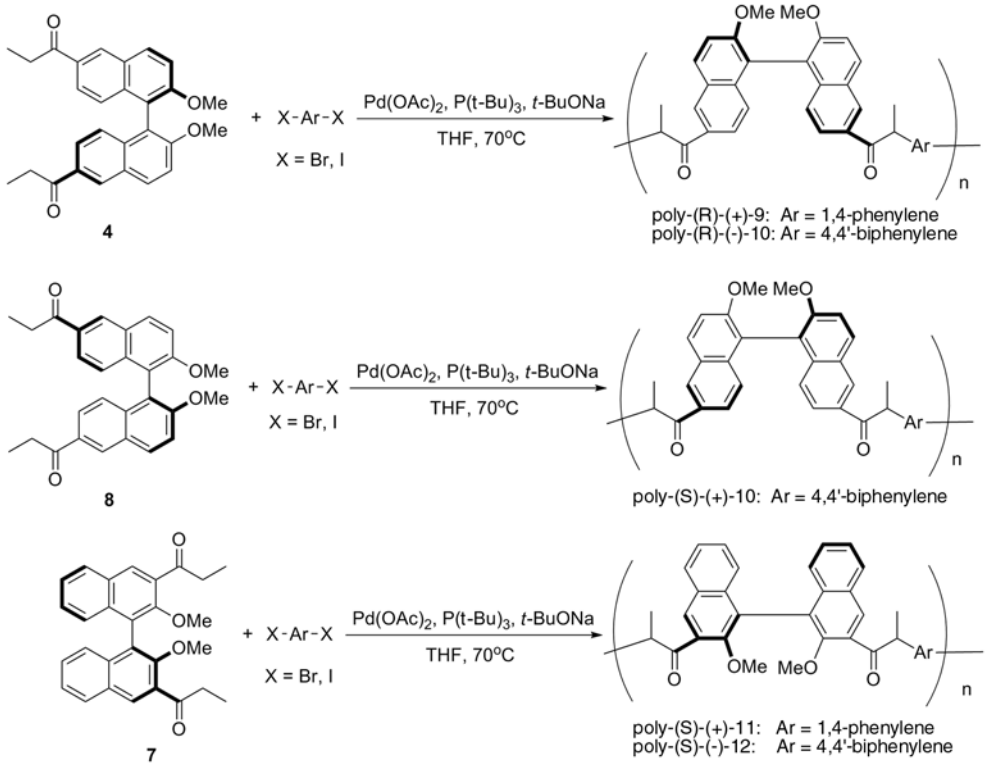

Figure 3. Construction of optically active main-chain polymers

Table 1. Polymerization results, optical rotation, and solubility

Entry[a]	M_w	PDI	$[\alpha]_D$	Soluble in
poly-(*R*)-(+)-9[b]	16 800	2.44	1.65	$CHCl_3$, CH_2Cl_2, THF, DMF, partially in Bz
poly-(*R*)-(–)-10[c]	19 400	2.77	–108.30	$CHCl_3$, CH_2Cl_2, THF, DMF, partially in Bz
poly-(*S*)-(+)-10[c]	21 200	2.61	78.10	$CHCl_3$, CH_2Cl_2, THF, DMF, partially in Bz
poly-(*S*)-(+)-11[b]	8 260	2.36	5.78	$CHCl_3$, CH_2Cl_2, THF, DMF, Bz
poly-(*S*)-(–)-12[c]	10 800	2.24	–60.10	$CHCl_3$, CH_2Cl_2, THF, DMF, Bz

[a]*R* and *S* denote the stereoconfigurations of the optically active monomers
[b]the linker between the chiral binaphthyls is 1,4-phenylene
[c]the linker between the chiral binaphthyls is 4,4′-biphenylene

played a significant role in effecting the outcome of this type of polymerization. Similarly, reaction of 4,4′-dihalobiphenyl with **4** under the same conditions also yielded polymers with enhanced molecular weights.

To prepare other type of chiral polymers, the reactions of (*S*)-(–)-3,3′-dihalo-2,2′-dimethoxy-binaphthyl with 1,4-dipropionylbenzene was also investigated. However, only oligomers were obtained and the products could not be clearly identified. This might be a combination effect of deactivation of the palladium intermediate and the steric hindrance of binaphthyl rings. Similarly, the polymerization of (*S*)-(–)-3,3′-dipropionyl-2,2′-dimethoxybinaphthyl (**7**) was also studied, where halides are not directly bound to the bulky binaphthyl ring. In contrast to the synthesis of **4**, the reaction of (*S*)-(–)-3,3′-dihalo-2,2′-dimethoxy-binaphthyl with BuLi and subsequent treatment of the resulting product with N,N-dimethylpropinylamide was sluggish and yielded no desired products, which was attributed to the stabilization of the lithium ion imposed from the adjacent methoxy and less electrophilic nature of the amide. This has been confirmed by the readily reaction of 3,3′-dilithio-2,2′-dimethoxybinaphthyl with propionaldehyde to produce an alcohol intermediate **6** in high yield. Compound **6** was easily oxidized by Jones agent to give **7** in good yield (Figure 1). The condensation polymerization of **7** with 1,4-dihalobenzene and 4,4′-dihalobiphenylene proceeded smoothly yielding main-chain chiral polymers with molecular weights up to 11 000 (Figure 3). The experimental result supports our analysis on the reactivity of this type of polymerization reactions.

The structures of the resulting polymers were characterized by both ^1H and ^{13}C NMR spectroscopy. Chiral optical properties were studied by polarimeter and circular dichroism (CD) spectroscopy. Figure 4 shows the UV-Vis and CD spectrum of **poly-(*R*)-(–)-10** and its corresponding monomer (**4**). The UV absorptions of the chiral polymer and monomer are nearly identical. The CD spectrum of **poly-(*R*)-(–)-10** exhibits slightly hypsochromic shift as compared to that of **4**. Large optical rotations were observed for chiral polymer **poly-(*R*)-(–)-10** ($[\alpha]_D = -108.3$) comparable to those of the pure monomer **4** ($[\alpha]_D = -112.7$). As a comparison, **poly-(*S*)-(+)-10** exhibited a large optical rotation of $[\alpha]_D = 78.1$. The different optical activity for **poly-(*R*)-(–)-10** and **poly-(*S*)-(+)-10** was further evidenced by circular dichroism (Figure 5). It is interesting to note that the substitutents can alter the direction of the polarized light. For polymers with *R* stereoconfiguration, more rigid linker such as biphenylene between the two chirality generating binaphthyl groups give polymers with large negative optical rotations ($[\alpha]_D = -108.3$, Table 1) indicating that the binaphthyl chiral environment is not disturbed. When shorter bridge such as 1,4-phenylene is used, the sign of the optical rotation has reversed to slightly positive ($[\alpha]_D = 1.65$, Table 1), an indication of the change of configuration of the polymer chain. CD spectra of the poly-

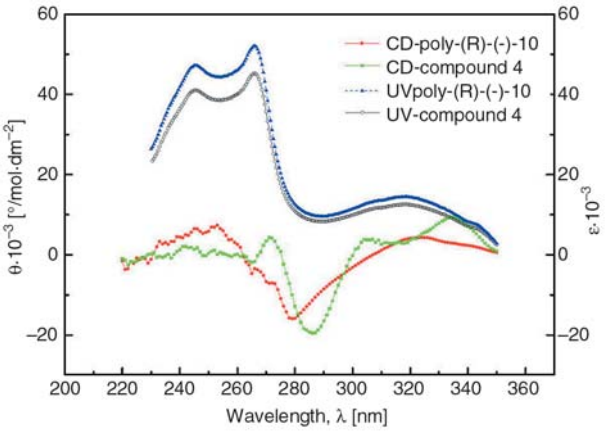

Figure 4. UV-Vis and CD spectra of **poly-(*R*)-(–)-10** and monomer **4**

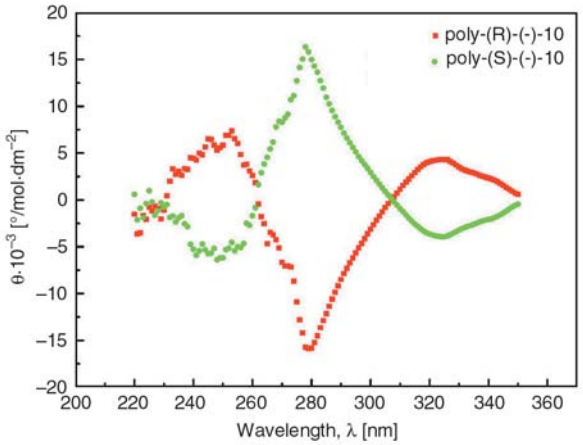

Figure 5. CD spectra of **poly-(*R*)-(–)-10** and **poly-(*S*)-(+)-10**

mers are similar to those of the monomers, suggesting little formation of secondary chiral conformations, and polymers maintain their original rigidity. It is important to note that the configuration of the newly created chiral centers in the chiral polymers might be important to the properties of the resulting main-chain chiral polymers. Further investigations on the stereochemistry of the chiral polymers and its effect on properties of chiral polymers will be conducted to delineate the structure-property relationship. Solubility tests indicate that the synthesized polymers are readily soluble in organic solvents such as chloroform, methylene chloride, benzene, DMF and THF (Table 1). Thermal properties of the synthesized polymers such as measurements of glass transition temperatures (T_g), thermal decomposition experiments (T_d) and other measurements on physical properties are currently in progress and will be reported in due time.

4. Conclusions

A simple route for the synthesis of the first soluble optically active main-chain chiral polyketones has been demonstrated using palladium catalyzed condensation reactions of dihalide and diketones. The reactivity of the monomers can be tuned by exchanging the positions of halide and alkanoyl substituents on the aryl rings. Higher molecular weight polymers can be obtained by reacting binaphthyl alkyl ketones with 1,4-dihalobenzene or 4,4′-dihalobiphenyl. Optical rotation and CD data indicate that the polymers adopt little helical configuration. The high solubility of the synthesized main-chain chiral aliphatic aromatic polyketones allows for materials to be made in the form of thin films and will expand potential applications of polyketones in various areas including chiral separation and recognition. Further measurements on thermal properties of the synthesized materials and synthetic strategy development of higher molecular weight poly(alkyl-aryl ketone) are currently under investigation.

References

[1] Teraguchi M., Mottate K., Kim S-Y., Aoki T., Kaneko T., Hadano S., Masuda T.: Synthesis of chiral helical poly(hydroxyl-containing phenylacetylene) membranes by in-situ depinanylsilylation and their enantioselective permeabilities. Macromolecules, **38**, 6367–6373 (2005).

[2] Nakano T., Satoh Y., Okamoto Y.: Synthesis and chiral recognition ability of a cross-linked polymer gel prepared by a molecular imprint method using chiral helical polymers as templates. Macromolecules, **34**, 2405–2407 (2001).

[3] Itsuno S.: Chiral polymer synthesis by means of repeated asymmetric reaction. Progress in Polymer Science, **30**, 540–558 (2005).

[4] Teraguchi M., Masuda T.: Poly(diphenylacetylene) membranes with high gas permeability and remarkable chiral memory. Macromolecules, **35**, 1149–1151 (2002).

[5] Pu L.: 1,1′-Binaphthyl dimers, oligomers, and polymers: Molecular recognition, asymmetric catalysis, and new materials. Chemical Reviews, **98**, 2405–2494 (1998).

[6] Wulff G.: Hauptkettenchiralität und optische Aktivität von Polymeren aus C-C-Ketten. Angewandte Chemie, **101**, 22–38 (1989).

[7] Xue Q. B., Kimura T., Fukuda T., Shimada S., Matsuda H.: Synthesis and lyotropic liquid crystal properties of chiral helical polycarbodiimides. Liquid Crystals, **31**, 137–143 (2004).

[8] van Beijnen A. J. M., Nolte R. J. M., Naaktgeboren A. J., Zwikker J. W., Drenth W., Hezemans A. M. F.: Helical configuration of poly(iminomethylenes). Synthesis and CD spectra of polymers derived from optically active isocyanides. Macromolecules, **16**, 1679–1689 (1983).

[9] Nozaki K.: Asymmetric catalytic synthesis of polyketones and polycarbonates. Pure and Applied Chemistry, **76**, 541–546 (2004).

[10] Kakuchi T., Obata M.: Synthesis and mechanism of a main-chain chiral polymer based on asymmetric cyclopolymerization. Macromolecular Rapid Communications, **23**, 395–406 (2002).

[11] Touchard F., Fache F., Lemaire M.: Polythioureas: Main chain chiral polymers in hydride transfer hydrogenation. European Journal of Organic Chemistry, **2000**, 3787–3792 (2000).

[12] Nozaki K., Sato N., Takaya H.: Highly enantioselective alternating copolymerization of propene with carbon monoxide catalyzed by a chiral phosphine-phosphite-palladium(II) complex. Journal of American Chemical Society, **117**, 9911–9912 (1995).

[13] Sperrle M., Consiglio G.: Diastereo- and enantioselectivity in the co-oligomerization of propene and carbon monoxide to dimethyl-4-oxoheptanedioates. Journal American Chemical Society, **117**, 12130–12136 (1995).

[14] Nazaki K., Sato N., Tonomura Y., Yasutomi M., Takaya H., Hiyama T., Matsubara T., Koga N.: Mechanistic aspects of the alternating copolymerization of propene with carbon monoxide catalyzed by Pd(II) complexes of unsymmetrical phosphine-phosphite ligands. Journal of American Chemical Society, **119**, 12779–12795 (1997).

[15] Buese M. A., Hogen-Esch T. E.: Oligomerization of vinyl monomers. 17. Stereoselective methylation of 1-lithio-1,3-bis(phenylsulfinyl)butane. Kinetic vs. thermodynamic control in the formation of diastereomeric ion pairs. Journal of American Chemical Society, **107**, 4509–4513 (1985).

[16] Yamaguchi H., Iwama T., Hayashi T., Doiuchi T.: Asymmetric induction polymerization of monomer salts prepared from 1,3-butadiene-1-carboxylic acid and optically active amines. Die Makromolekulare Chemie, **191**, 1243–1251 (1990).

[17] Odian G.: Principles of polymerization. Wiley, New York (1991).

[18] Colquhoun H. M., Paoloni F. P. V., Drew M. G. B., Hodge P.: Dithioacetalisation of PEEK: A general technique for the solubilisation and characterization of semi-crystalline aromatic polyketones. Chemical Communications, **32**, 3365–3367 (2007).

[19] Liu X. B., Du R. H., Hao L. L., Wang S., Cao G. P., Jiang H.: Synthesis, characterization and rheological property of biphenyl-based polyarylene ether nitrile copolymers. Express Polymer Letters, **1**, 499–505 (2007).

[20] Ozarslan Ö., Yildiz E., Yilmaz T., Güngör A., Kuyulu A.: Novel poly(arylene ether ketone ketone)s synthesized by Friedel-Crafts acylation. Macromolecular Chemistry and Physics, **199**, 1887–1893 (1998).

[21] Johnson R. N., Farnham A. G., Clendinning R. A., Hale W. F., Meriiam C. N.: Poly(aryl ethers) by nucleophilic aromatic substitution. I. Synthesis and properties. Journal of Polymer Science Part A-1: Polymer Chemistry, **5**, 2375–2398 (1967).

[22] Bonner W. H.: Aromatic polyketones. US Patent 3065205, USA (1962).

[23] Yu Y. K., Xiao F., Cai M. Z.: Synthesis and properties of poly(aryl ether ketone ketone)/poly(aryl ether ether ketone ketone) copolymers with pendant cyano groups. Journal of Applied Polymer Science, **104**, 3601–3606 (2007).

[24] Chiechi R. C., Sonmez G., Wudl F.: A robust electroactive n-dopable aromatic polyketone. Advanced Functional Materials, **15**, 427–432 (2005).

[25] Guo Q., Bo S., Chen T.: Synthesis of macrocyclic arylene ketone oligomers containing the phthaloyl moiety by Friedel-Crafts acylation reaction. Chemistry Letters, **33**, 414–415 (2004).

[26] Danforth R. L., Machado J. M., Jordaan J. C. M.: Aliphatic polyketones – A new family of engineering thermoplastics. Plastic Engineering, **52**, 77–79 (1996).

[27] Jiang Z., Sen A.: Palladium(II)-catalyzed isospecific alternating copolymerization of aliphatic alpha-olefins with carbon monoxide and isospecific alternating isomerization cooligomerization of a 1,2-disubstituted olefin with carbon monoxide. Synthesis of novel, optically active, isotactic 1,4- and 1,5-polyketones. Journal of American Chemical Society, **117**, 4455–4467 (1995).

[28] Nozaki K., Kosaka N., Graubner V. M., Hiyama T.: Methylenation of an optically active γ polyketone: Synthesis of a new class of hydrocarbon polymers with main-chain chirality. Macromolecules, **34**, 6167–6168 (2001).

[29] Guo J., Wang B., Zhu C.: Copolymerization of carbon monoxide and styrene catalyzed by resin-supported palladium polymer. Express Polymer Letters, **1**, 69–76 (2007).

[30] Wang D., Wei P., Wu Z.: A new polymerization reaction: Synthesis of soluble polyketones and poly(arylenevinylene)s. Macromolecules, **33**, 6896–6898 (2000).

[31] Pu L.: The study of chiral conjugated polymers. Acta Polymerica, **48**, 116-141 (1997).

[32] Hu Q. S., Huang W. S., Pu L.: A new approach to highly enantioselective polymeric chiral catalysts. Journal of Organic Chemistry, **63**, 2798–2799 (1998).

[33] Hu Q-S., Huang W-S., Vitharana D., Zheng X-F., Pu L.: Functionalized major-groove and minor-groove chiral polybinaphthyls: Application in the asymmetric reaction of aldehydes with diethylzinc. Journal of American Chemical Society, **119**, 12454–12464 (1997).

[34] Liu Y., Zhang S., Miao Q., Zheng L., Zong L., Cheng Y.: Fluorescent chemosensory conjugated polymers based on optically active polybinaphthyls and 2,2′-bipyridyl units. Macromolecules, **40**, 4839–4847 (2007).

[35] Jaycox G. D.: Stimuli-responsive polymers. VII. Photomodulated chiroptical switches: Periodic copolyaramides containing azobenzene, phenylene, and chiral binaphthylene main-chain linkages. Journal of Polymer Science, Part A: Polymer Chemistry, **42**, 566–577 (2004).

[36] Hu Q-S., Vitharana D., Liu G. Y., Jain V., Wagaman M. W., Zhang L., Lee R. T., Pu L.: Conjugated polymers with main chain chirality. 1. Synthesis of an optically active poly(arylenevinylene). Macromolecules, **29**, 1082–1084 (1996).

[37] Pu L.: Recent developments in asymmetric catalysis using synthetic polymers with main chain chirality. Tetrahedron: Asymmetry, **9**, 1457–1477 (1998).

[38] Toda F., Tanaka K., Stein Z., Goldberg I.: Optical resolution of binaphthyl and biphenanthryl diols by inclusion crystallization with N-alkylcinchonidium halides. Structural characterization of the resolved materials. Journal of Organic Chemistry, **59**, 5748–5751 (1994).

[39] Minatti A., Dötz K. H.: Quinoid BINOL-type compounds as a novel class of chiral ligands. Tetrahedron: Asymmetry, **16**, 3256–3267 (2005).

[40] Meyer G., Rollin Y., Perichon J.: Electrocatalysis by nickel complexes, of the synthesis of aromatic or vinylic from corresponding brominated derivatives (in French). Tetrahedron Letters, **27**, 3497–5000 (1986).

eXPRESS Polymer Letters Vol.2, No.6 (2008) 449–459
Available online at www.expresspolymlett.com
DOI: 10.3144/expresspolymlett.2008.54

Synthesis and characterization of hybrid cured poly(ether-urethane)acrylate/titania microcomposites formed from tetraalkoxytitanate precursor

A. L. Tolstov[1*], *V. F. Matyushov*[1], *D. O. Klymchuk*[2]

[1]Institute of Macromolecular Chemistry, National Academy of Sciences of Ukraine
48 Kharkivske shose, 02160 Kyiv, Ukraine
[2]N.G. Kholodny Institute of Botany, National Academy of Sciences of Ukraine
2 Tereshchenkivska str., 01601 Kyiv, Ukraine

Received 17 March 2008; accepted in revised form 26 April 2008

Abstract. Hybrid poly(ether-urethane)acrylate (PEUA)/titania (TiO_2) microcomposites were prepared using a novel method that includes a swelling of different photo-crosslinked PEUA networks in concentrated tetraisopropoxytitanate ($Ti(OiC_3H_7)_4$ or TIPT) precursor solution in organic media followed by the hydrolysis of covalently bonded polyalkoxytitanate ($[–OTi(OC_3H_7)_2–]_n$) chains and their aggregation to amorphous micro- and nano-scale sized TiO_2 particles. A formation of polymer/titania hybrids was confirmed by complex investigations of the hybrids using infrared (IR) spectroscopy, small angle X-ray scattering (SAXS) analysis, scanning electron microscopy (SEM) and gravimetry. The dependence of titania phase formation behavior *versus* functionality of the poly(ether-urethane)acrylate network was discussed. The presence of reactive groups in the organic network promotes the formation of surface-bonded ball-shaped type TiO_2 inclusions as well as provides transparency to the hybrid film samples. The results obtained in this work can be applied for the development of polymer/TiO_2 composite materials for multipurpose optical application and advanced sealants.

Keywords: *polymer composites, hybrids, titania, material testing*

1. Introduction

Nowadays a great interest of many leading scientists in the world is attracted by perspective high-performance hybrid organo-inorganic polymer composite materials because of their multiple applications. Typically, for the composites (including hybrid composites) preparation the different dispersed substances, like metals (Ag, Au, Cu, Pt) [1, 2], carbon [3], clays [4], $CaCO_3$ [5], alumina [1], silica [1, 6, 7], titania (TiO_2) [1, 8–14] and others could be used. The polymer/titania composites are one of the most widespread due to their multifarious application fields, such as adhesives and sealants [8], high-refractive thin films [9], photocatalysts [11], composite solid polymer electrolytes for Li-batteries [13] or solar cells [14, 15]. Basic methods of the polymer/titania composites preparation could be presented as follows: (1) formation of polymer materials with introduced fine-dispersed commercial TiO_2 [8] or commercially available stabilized titania suspension [16], (2) self-made relatively stable TiO_2 sol preparation followed by incorporation into polymer matrix [10, 17, 18], or (3) condensation of different functional organotitanium monomers followed by their polymerization until the linear TiO_2-containing oligomers or polymer networks are formed [19].

*Corresponding author, e-mail: tolstov.aleksandr@rambler.ru

Here another perspective way was proposed for the preparation of hybrid poly(ether-urethane)acrylate (PEUA)/titania microcomposites. Photo-cured poly(ether-urethane)acrylates were swollen in concentrated tetraisopropoxytitanate ($Ti(OiC_3H_7)_4$ or TIPT) solutions in organic media followed by exhaustive hydrolysis of the covalently bonded precursor into titania aggregates. The microcomposites prepared were studied thoroughly using infrared (IR) spectroscopy, small angle X-ray scattering (SAXS) technique, scanning electron microscopy (SEM), gravimetry.

2. Experimental section

2.1. Materials

Oligooxypropylenes (OOP) with different functionalities (hydroxyl-terminated) having molecular weights of 2000 (bifunctional) and 5000 (trifunctional) ($OOP^{2000\text{-}2}$ and $OOP^{5000\text{-}3}$, correspondingly) were taken as the oligoether component of the poly(ether-urethane)acrylates and were used as received. Commercial toluene diisocyanate (TDI) (mixture of 2,4- and 2,6-isomers with 80/20 ratio), hexamethylene diisocyanate (HMDI), ethylene glycol monomethacrylic ester (MEG), acrylic acid (AA), methyl methacrylate (MMA) and tertaisopropoxytitanate, $Ti(OiC_3H_7)_4$, (all from Aldrich Chemicals) were additionally purified by distillation at reduced pressure. Dicyclohexyl ketone (DCHK) has been used as a photoinitiator for PEUA curing without any purification. As solvents and swelling agents the chemical grade 2-propanol (2-P) or 1,4-dioxane (1,4-D) were used. As an extractive solvent for gel fraction determination pure acetone has been applied.

2.2. Preparation of poly(ether-urethane)acrylates

Poly(ether-urethane)acrylates of different structures, functionalities (terminal acrylic unsaturation) and molecular weights based on corresponding oligoethers, TDI or HMDI and MEG were synthesized using a method that is similar with one described in [20]. Composition and main characteristics of the PEUA prepared are summarized in Table 1. Schematically the PEUA macromolecules architecture and their definite terminal acrylic functionality were presented in Figure 1.

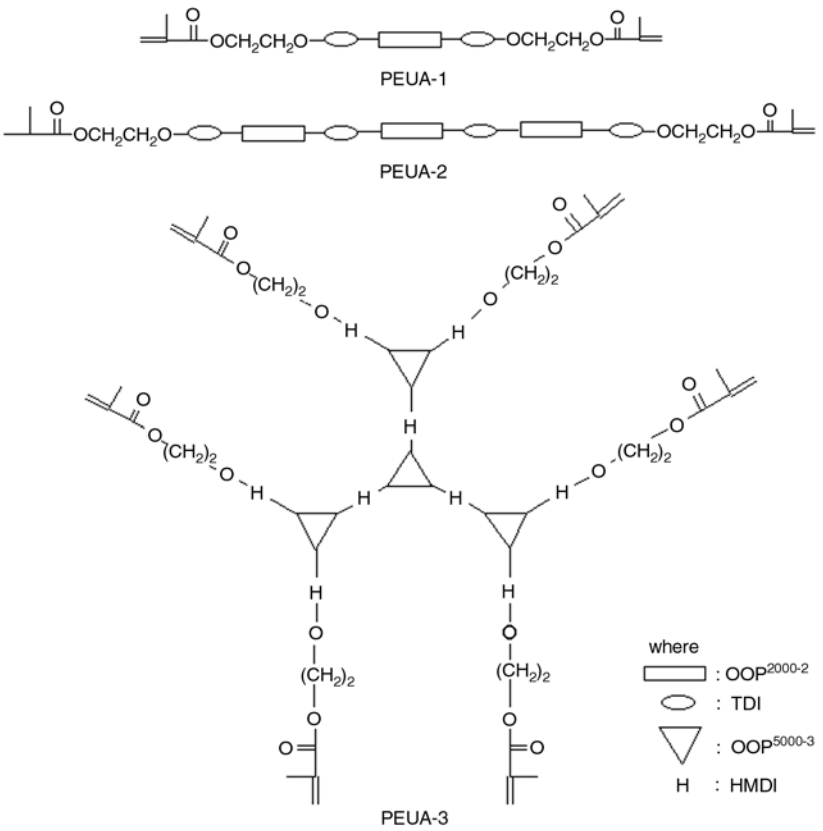

Figure 1. Schematic molecular architecture of PEUA synthesized

Table 1. Composition and basic characteristics of uncured poly(ether-urethane)acrylates synthesized

Sample	Composition	Molar components ratio	M_w (viscosimetry)	Molecular structure
PEUA-1	$OOP^{2000\text{-}2}$/TDI/MEG	1/2/2	2500	linear
PEUA-2	$OOP^{2000\text{-}2}$/TDI/MEG	3/4/2	7000	linear
PEUA-3	$OOP^{5000\text{-}3}$/HMDI/MEG	4/9/6	–	hyper-branched

2.3. Photo-curing PEUA

Functionalized poly(ether-urethane)acrylate networks were synthesized from corresponding PEUA, AA and MMA by typical photo-initiated copolymerization process [21] using DCHK photoinitiator and film samples of 0.5 mm thickness were obtained. The components ratio of the PEUA/AA/MAA composite samples was 60/10/30 (by weight). The free pendant COOH groups (presence is caused by AA constituent) in the poly(ether-urethane)acrylate networks are necessary to be the covalent junction points between organic poly(ether-urethane)acrylate constituent and inorganic titania component of the composites prepared. As a comparative non-functionalized (without free pendant carboxyl groups) sample the PEUA/MAA = 60/40 (by weight) was also prepared.

2.4. Preparation of polymer/titania hybrids

For preparation of hybrid polymer/titania microcomposites the poly(ether-urethane)acrylate networks were swollen in 50% (by weight) TIPT solution in 2-propanol or 1,4-dioxane at ambient temperature for definite time. Swelling ratio values for each PEUA network sample were calculated by Equation (1):

$$SR = \left(\frac{100 m_s}{m_0 q} - 1 \right) \cdot 100\% \tag{1}$$

where SR, m_0 and m_s are the swelling ratio [%], film weight before swelling [g] and swollen film weight [g], respectively, q is a gel fraction content of initial PEUA network (values varied in the range of 95.2–97.3 for different PEUA networks).

Swollen samples have been dried at appropriate conditions on air at ambient temperature followed by heating in oven at 90°C for 3 hrs. The scheme of possible interactions (according to literature data [22]) between $Ti(OiC_3H_7)_4$ precursor and functionalized polymer network is presented below (Figure 2). Water traces (in the PEUA network or in the solvents used) induces the condensation processes between grafted (onto PEUA chains) and/or 'free' $Ti(OiC_3H_7)_4$ molecules that always result in polyalkoxytitanate chains bonded with main organic chains of PEUA network.

Hydrolysis of polyalkoxytitanate ($[–OTi(OC_3H_7)_2–]_n$) chains covalently joined with poly(ether-urethane)acrylate network was performed in boiling water for an appropriate time (experimentally determined) followed by drying in oven at 110°C to constant weight. The samples composition and their main characteristics are summarized in Table 2. Quantity of TiO_2 adsorbed by PEUA network was determined by Equation (2):

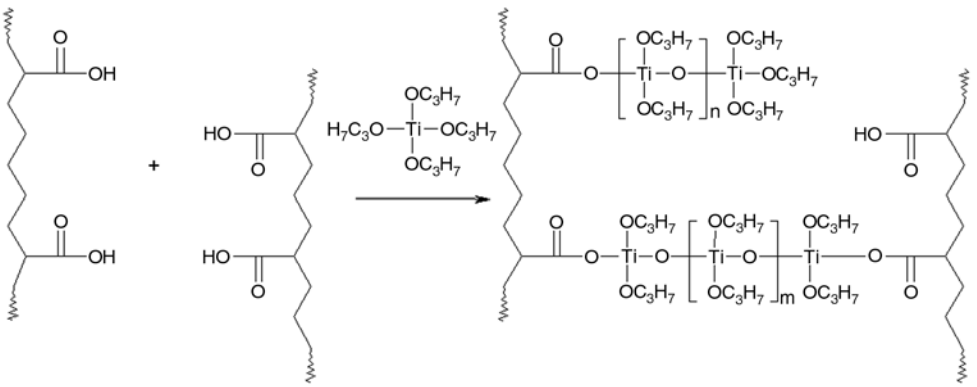

Figure 2. Reaction between COOH-functionalized polymer network (A1–A6 samples) and TIPT precursor

Table 2. Composition and characteristics of hybrids prepared

Sample code	Composition	Gel content [%]	Treatment conditions	Swelling ratio, SR [%]	TiO_2 content [wt%]	TIPT adsorbed[a] [mg]	Molar AA/TIPT ratio	Trans-parency[b]
A1	PEUA-1/AA/MMA	95	TIPT/2-P; 2 hrs	12	3.8	139.5	1/0.35	T
A2			TIPT/2-P; 24 hrs	55	10.4	411.0	1/1.04	S
A3			TIPT/1,4-D; 24 hrs	120	13.6	560.8	1/1.42	S
A4	PEUA-2/AA/MMA	96	TIPT/1,4-D; 24 hrs	250	22.7	1046.6	1/2.65	S
A5			TIPT/1,4-D; 72 hrs	300	30.8	1587.1	1/4.02	S
A6	PEUA-3/AA/MMA	97	TIPT/1,4-D; 24 hrs	153	19.4	854.0	1/2.16	S
A7	PEUA-2/MAA	95	TIPT/1,4-D; 24 hrs	203	16.8	719.9	–	N

[a]Quantity of adsorbed TIPT [mg] per unit weight [1 g] of PEUA network

[b]T – transparent; S – semitransparent; N – non-transparent; before swelling the polymer networks are fully transparent

$$w_{TiO_2abs} = \left(\frac{100 m_c}{m_0 q} - 1 \right) \cdot 100\% \qquad (2)$$

where w_{TiO_2abs} and m_c are the quantity of TiO_2 adsorbed [wt%] and final composite film weight after complex treatment (swelling → drying → hydrolysis → drying) [g], respectively. Quantity of TIPT adsorbed was calculated by Equation (3):

$$m_{TIPTads} = \frac{1000 \cdot w_{TiO_2abs} \cdot M_{TIPT}}{(100 - w_{TiO_2abs}) \cdot M_{TiO_2}} \qquad (3)$$

where $m_{TIPTads}$ is the $Ti(OiC_3H_7)_4$ weight of chemically adsorbed (bonded) by PEUA network [mg], M_{TIPT} and M_{TiO_2} are the molecular weights of TIPT and TiO_2, correspondingly.

During hydrolysis of polyalkoxytitanate chains the condensation and aggregation processes are carried out and hybrid polymer/titania composites with incorporated amorphous TiO_2 micro- and nano-sized structures and, correspondingly, defined level of heterogeneity are formed [22, 23].

2.5. Samples characterization

Chemical changes during synthesis of hybrid poly(ether-urethane)acrylate/titania microcomposites were identified via infrared spectral studies of the film samples using Bruker Tensor™ 37 FTIR analyzer in the spectral region of 4000–600 cm^{-1}.

For phase heterogeneity (at nano-scale level) characterization a small angle X-ray scattering, SAXS, of the hybrid samples were carried out by slit collimated small angle X-ray camera KRM-1 according to Kratky technique over the scattering angle 2Θ = 0.08–3.5° using Ni-filtered Cu-K_α radiation (λ = 0.154 nm). Geometrical adjectives of collimation system satisfied the requirements of the infinite high of X-ray beam [24]. Accomplishment of collimation amendment procedure was performed by Schmidt method [25]. Relative parameters of microheterogeneity, like local heterogeneity range, l_p [26], and relative heterogeneity parameter (Porod invariant), Q [27] were determined.

In order to characterize micro- and nano-scale heterogeneity the morphology studies of the composites prepared were performed by JEOL JSM 6060 LA Scanning Electron Microscope (Tokyo, Japan) at an accelerating voltage of 30 kV. Before measurements the samples were sputter-coated with gold film of 5–10 nm thickness. Microscopy technique was combined with image analysis in order to quantify the distribution size of the particles (two-dimension analysis).

3. Results and discussion

3.1. Swelling behavior and gravimetry analysis

Studies of hybrid PEUA/titania materials were carried out using swelling characterization, gravimetry analysis, IR spectroscopy, SAXS and SEM combined with image analysis. Visual observations of the initial polymer networks and their hybrid composite analogues (after TIPT treatment and hydrolysis) were carried out and certain changes are identified. As it was observed the initial polymer networks are fully transparent for visible light, whereas their treated (with TIPT solutions) analogues are characterized by slight transparency reduction. It is important that the aforementioned changes are characteristic of the samples with pen-

dant carboxylic functionality of the networks, while the A7 composite (based on non-functionalized polymer network) became deep-brown and non-transparent. Apparently, it is connected with enlarged linear dimensions of TiO_2 inclusions formed during hydrolysis of physically adsorbed tetraisopropoxytitanate agent within non-functionalized poly(ether-urethane)acrylate network compared to the other samples (based on COOH-containing networks). A quite intensive dyeing of the A7 sample film could be due to redox processes that lead to partial oxidation of organic network and corresponding reduction of Ti^{4+} into Ti^{3+}. It should be noted that for the other samples (A2–A6) these processes are slightly pronounced.

The basic characteristics of initial polymer networks and composites obtained were determined and the results were summarized and analyzed (see data presented in Table 2). As it was found, all initial poly(ether-urethane)acrylate networks show quite similar level of gel fraction content values in the range of 95.2–97.3%. At the same time swelling values of these film in different organic solvents (2-P or 1,4-D) are different (from 120% for PEUA-1/AA/MMA to 250% for PEUA-2/AA/MMA samples at the same treatment conditions), however clear correlation between the swelling ratio and chemical structure or composition was not determined. As it was found the TiO_2 content values for all composites range are varied from 3.8 to 30.8 wt%. It is clearly seen, the quantity of TiO_2 adsorbed depends on treatment time (in 50% TIPT solution in different organic media), as presented in Figure 3. In full compliance with the data presented the poly(ether-urethane)acrylate networks shows adequately high level of TIPT adsorption (especially the A5 sample having a maximum treatment time in TIPT solution). It should be noted that relatively low level of TIPT adsorption and TiO_2 content in A1 and A2 composites is due to low swelling level of poly(ether-urethane)acrylate networks in 2-P solvent compared to 1,4-D medium (for A1 sample a complex influence of poor swelling agent (2-P) as well as lowest treatment time are found).

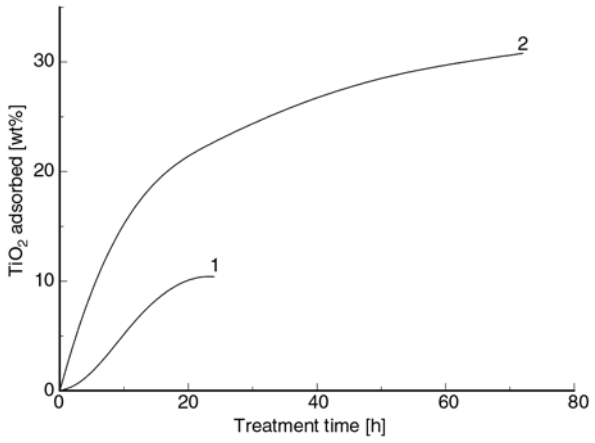

Figure 3. TiO_2 content versus treatment time (50% TIPT solution in different organic media) for microcomposite samples: (1) A1–A2 in 2-propanol, (2) A4–A5 in 1,4-dioxane

Analysis of adsorbed TIPT content and molar AA/TIPT ratio data in the hybrid microcomposites shows their direct correlation with treatment time. Clearly, the increasing treatment time of PEUA networks increases the quantity of TIPT adsorbed, probably, due to increasing of $Ti(OiC_3H_7)_4$ bonded with PEUA networks and extended into grafted $[–OTi(OiC_3H_7)_2–]_n$ chains. Highest molar AA/TIPT ratios (2.65 and 4.02 mol of adsorbed $Ti(OiC_3H_7)_4$ per 1 mol of acrylic acid in poly(ether-urethane) crylate network) in full range of hybrid composite prepared were found for A4 (the best result among the composites after 24 hrs treatment in TIPT solution) and A5 (maximum (72 hrs) treatment time) compositions. Additionally, an evidence of grafting and condensation (transformation of single TIPT grafts into polyalkoxytitanate chains) processes of TIPT component is the absence of $Ti(OiC_3H_7)_4$ sweating (formation of moisture-initiated surface thin coating of whitish TIPT hydrolysis products) onto film sample surface during first stage drying process. Moreover, the presence of isopropyl alcohol in the 1,4-D spent solution (after separation from the TIPT agent) was also determined, but quantitative (chromatography or titration) analysis was not carried out. Thus, on the base of the results presented it can be supposed that a creation of single $–Ti(OC_3H_7)_3$ grafts onto organic PEUA network chains, their subsequent extension into $[–OTi(OC_3H_7)_2–]_n$ chains, as well as exhaustive hydrolysis and aggregation into spatial $–[O–Ti(O–)_2–]_n$ structures of amorphous TiO_2 domains occurred. For confirmation of aforementioned facts of hybrid microcomposites formation the spectral and phase investigations, using IR spectroscopy, SAXS and SEM techniques were carried out.

3.2. IR characterization of the composites

IR spectra of initial polymer network (before treatment) and the hybrids prepared (after full treatment cycle; see *2.4. Preparation of polymer/titania hybrids*) are presented in Figure 4. Beforehand, it must be noticed that chemical composition and structures of initial poly(ether-urethane)acrylates and photo-cured ones are quite similar in respect of IR spectroscopy analysis. IR spectrum of initial COOH-functionalized PEUA network of A4 (A5) composition before TIPT treatment was presented and used as a reference curve. The IR spectra of the hybrid composites (A2, A3 and A4) were obtained and analyzed.

As it can be seen the initial polymer network (Figure 4, curve 1) has typical characteristic bands of well-known and well-described in literature poly(ether-urethane)s (poly(ether-urethane)acrylates) [28]. For detailed analysis the most characteristic (for these compositions) bands of O–H (N–H) stretching vibrations in the region of 3500–3200 cm^{-1} and C=O stretching vibration at 1730–1700 cm^{-1} have been clearly selected. Here the Gaussian peaks decomposition technique was applied for analysis of relative bands of the spectra to determine any chemical changes of the components during the composites preparation. Additionally, several other characteristic bands in the spectral regions of 3000–2850, 1500–1400 and ~1000 cm^{-1} were also found.

Detailed Gaussian peaks decomposition analysis of the complex O–H (N–H) and C=O bands shows the following. The main constitution of O–H (N–H) band of initial PEUA network corresponds to H-bonded N–H stretching vibration of urethane component centered at 3321 cm^{-1}. Low intensity stretching vibration of 'free' N–H groups and/or O–H groups of carboxyls at 3456 cm^{-1} was also observed [29]. Complex C=O band could be divided at least on two peaks centered at 1711 cm^{-1} (C=O stretch of free COOH groups) and at 1729 cm^{-1} (C=O stretch of urethane/(meth)acrylates ester groups). It should be noted that relative intensity ratio of characteristic bands of 'free' carboxyls C=O and urethane/(meth)acrylate ester C=O ($I_{C=Oc}/I_{C=Ou/a}$), as well as relative intensity ratio of O–H and N–H groups (I_{O-H}/I_{N-H}) were used for qualitative analysis of chemical changes within hybrids formed. Other bands of the functional groups having a secondary importance for current IR spectra analysis have been also detected in the IR spectrum of initial PEUA. Namely, the sharp medium intensity bands at 2970 and 2870 cm^{-1} are attributed to C–H stretching vibration of methylene groups of oligoether segments. Aromatic constituent of the polyurethane is revealed by multiple weak bands at 1473 and 1450 cm^{-1} (C–C bonds), as well as at 1273 and 1007 cm^{-1} (C–H bonds). The high intensity band at 1083 cm^{-1} was attributed to C–O–C ether linkage of oligoether constituent of poly(ether-urethane)acrylate network.

In IR spectra of the TiO_2-containing hybrid composites (Figure 4, curves 2–4) well-defined changes can be seen related to the presence of dispersed TiO_2 inclusions formed inside polymer network. Analysis of IR spectra of hybrid composites shows the definite changes of absorption bands of the initial PEUA network. First of all, a significant intensity increasing and wavenumber position shifts of N–H (by 2–12 cm^{-1}) and O–H bands (by 7–19 cm^{-1}) were found because of redistribution of the proper H-bonds network of the pure PEUA component when the inorganic (TiO_2) component introduced as well as an appearance of other functional groups (like O–H groups on titania surface that play a definite role in O–H band intensity) of new inorganic component was determined. The band corresponds to O–H groups of the 'free' carboxyls disappeared (at 3456 cm^{-1}) and new characteristic band of O–H having another nature (at ~3445–3450 cm^{-1}) observed. The increasing I_{O-H}/I_{N-H} ratio in the range initial PEUA → hybrid compos-

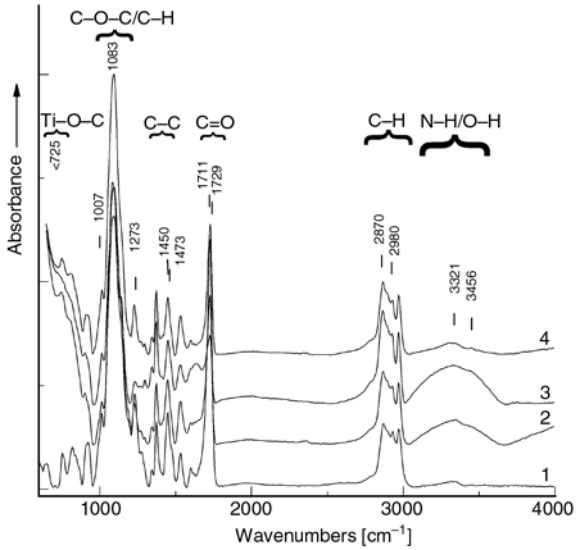

Figure 4. Infrared spectra of initial polymer and the composites prepared: (1) initial A4, (2) A2, (3) A3, (4) A4

Table 3. FTIR analysis (Gaussian) of complex O–H (N–H) and C=O bands of the hybrid composites

Sample	C=O				$I_{C=Oc}/I_{C=Ou/a}$	N–H		O–H		I_{O-H}/I_{N-H}
	[carboxyl]		[urethane/acrylate]							
	position [cm^{-1}]	relative intensity, $I_{C=Oc}$ [a.u.]	position [cm^{-1}]	relative intensity, $I_{C=Ou/a}$ [a.u.]		position [cm^{-1}]	relative intensity, I_{N-H} [a.u.]	position [cm^{-1}]	relative intensity, I_{O-H} [a.u.]	
Initial A[a]	1711	0.147	1729	0.230	0.64	3321	0.006	3456	0.002	0.33
A2	1710	0.095	1729	0.156	0.61	3323	0.036	3437	0.027	0.75
A3	1712	0.043	1730	0.077	0.56	3331	0.056	3346	0.048	0.85
A4	1711	0.068	1729	0.141	0.48	3333	0.016	3449	0.008	0.50

[a]pure PEUA network

ites evidenced of organic-inorganic hybrids formation. One can supposed an abnormally high intensity of O–H band can be evidenced of incomplete isopropyl alcohol elimination from relatively dense organic-inorganic network of A2 and A3 composites compared to initial PEUA network. Similar conclusions can be drawn when the analysis of complex C=O characteristic bands was carried out. As it was found the position of corresponding C=O bands is practically the same while their intensity substantially changed. Actually, the relative intensity $I_{C=Oc}/I_{C=Ou/a}$ ratio is gradually decreased when the TiO_2 content in the range of initial PEUA → A2 → A3 → A4 is increased. It is an evidence of decreasing 'free' COOH content in the composites prepared due to their participation in chemical interactions with initial inorganic constituent ($Ti(OiC_3H_7)_4$). Additionally, the appearance of a new broad and high intensity Ti–O stretch in the wavenumber region of lower 725 cm^{-1} (a shoulder of the mentioned peak is presented in Figure 4, curves 2–4) in the composite samples was observed. The shifts or redistribution of the intensities of other functional groups of organic constituent, namely aliphatic and aromatic C–C and C–H, C–O–C ether, etc., which do not take part in any interactions during hybrid composites formation practically were not observed. Thus, detailed IR analysis of the microcomposites prepared allowed to confidently concluded that the chemical interactions between carboxyl groups of poly(ether-urethane)acrylate networks and $Ti(OiC_3H_7)_4$ precursor are carried out and formation of the organic-inorganic hybrids occurred.

3.3. SAXS measurements

To investigate the microheterogeneity level of the hybrid composites prepared SAXS measurements were carried out on initial PEUA, samples with higher TiO_2 inclusions contents as well as pure amorphous TiO_2 prepared using standard sol-gel technique [30], and the results are reported in Figure 5 and Table 4. Clearly, the diffractogram presented shows that the initial components and hybrid

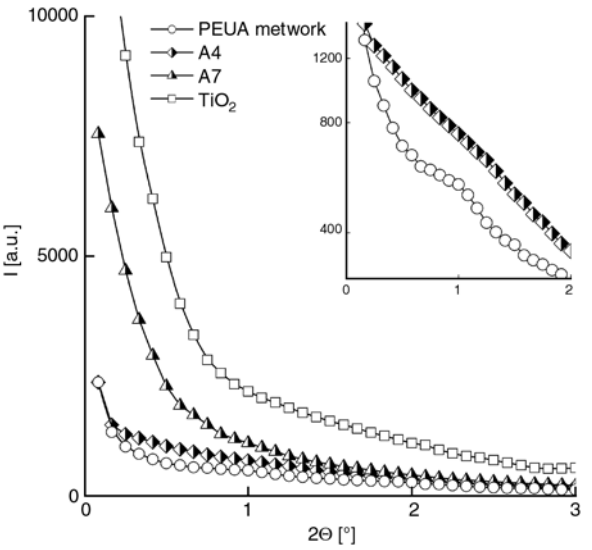

Figure 5. SAXS diffractograms of initial components and selected polymer/titania hybrids

Table 4. SAXS and SEM data of initial PEUA and hybrid A4 and A7 microcomposites

Sample	SAXS		SEM; particle size [μm]		
	l_p [nm]	Q [a.u.]	min	max	main fraction
Initial PEUA network	8.4	9.8	–	–	–
A4	5.0	11.2	0.17	2.50[a]	0.90–1.71
A7	3.5	14.6	0.11	7.02	0.11–7.02

[a] a presence of TiO_2 particle with size of ~2.9 μm was detected as anomalous

composite samples obtained exhibit a strongly pronounced level of heterogeneity. As it can be seen the SAXS diffractograms obtained have a typical exponential dependence for the composites with relatively high polydispersity level of heterogeneous regions in nano-scale level. Clearly, that amorphous TiO_2 has typical (for low-molecular substances) high scattering intensity level in full 2Θ range and does not have any peaks on the SAXS curve due to absence of well-defined nano-scaled structural features. Otherwise, for initial PEUA network as well as for the hybrid composites the some similar peculiarities were found. Detailed analysis of SAXS curves of initial PEUA network and A4 hybrid at high resolution condition (Figure 5, high resolution supplement) shows a broad flat peak centered at $2\Theta \approx 1°$. For A7 sample an existence of this peak is also considered (at a little higher 2Θ) but it is not so appreciable. It can be evidence of slight predominance of one closely-sized nanoheterogeneous regions over the other ones. Mathematical treatment of these plots is allowed to calculate a characteristic size of nanoheterogeneity regions, l_p, for the samples. Specifically, l_p values for A4 and A7 composites was found as 5.0 and 3.5 nm, respectively, compared to 8.4 nm for initial PEUA network. As it will be shown below (SEM measurements) these values do not reflect a real heterogeneity of the hybrid composites and characterize exceptionally nano-scale heterogeneity (phase separation) level of typical poly(ether-urethane)acrylates. Another method of heterogeneity characterization was also applied and described using Porod invariant. Actually, as it was calculated, the Porod invariant values, Q, for initial PEUA network, A4 and A7 hybrids were about 9.8, 11.2 and 14.6 relative units, respectively. Thus, A7 hybrid composition (based on non-functionalized poly(ether-urethane)acrylate) has a higher heterogeneity level compared to the A4 hybrid, and, correspondingly, pure PEUA network (Table 4). Additionally, it should be noted that the A7 composite sample has a higher intensity of scattering compared to A4 composite in the full range of 2Θ scale (up to $2\Theta = 3°$) that can be also due to higher heterogeneous regions content.

Summarizing the foregoing facts it can be concluded that the microcomposite samples prepared are characterized by well-defined nanoheterogeneity level. Increasing phase separation processes and formation of smaller nano-scaled heterogeneous regions occur while the amorphous TiO_2 agglomerates are formed inside organic PEUA network. An evidence of heterogeneous character of the hybrid composites in micro-scale level will be shown below using their morphology studies by SEM.

3.4. Morphology characterization

The surface morphology of the aforementioned hybrid composites was investigated and SEM microphotographs and basic heterogeneity characteristics were presented in Figures 6, 7 and Table 4, correspondingly. First, as it could be seen from Figure 6, a–d formation of the hybrid composites is accompanied by partial fracturing of the samples because of internal tension excess during formation and enlargement of inorganic TiO_2 inclusions. The morphology analysis of A4 composite (Figure 6a–6b; Figure 7, curve 1) shows relatively low polydispersity level of dispersed phase with TiO_2 particle size from 2.50 to 0.17 μm and, probably, even lower (as an evidence of significant sample transparency). The dominant TiO_2 fraction dispersed in polymer network was about 0.90–1.70 μm, whereas the presence of large particles with linear dimension at ~3 μm is atypical (see Table 4; Figure 7, curve 1). It should be noted that for A4 hybrid relatively uniform TiO_2 aggregates distribution in the sample volume was found. As an interesting fact of SEM studies, the ball-shaped dispersed titania particles (single or aggregates) were mainly observed for this composition (Figure 6a–6b).

Otherwise, A7 hybrid (Figure 6c–6d) is characterized by uniform TiO_2 particles distribution with particle linear dimension size in the range of 0.1–7.0 μm (Table 4; Figure 7, curve 2). It is important that there are no any possibilities to determine the dominant fraction of TiO_2 inclusions in A7 hybrid sample due to quite broad particle size range. Moreover, irregular shape types of titania inclusions are typical for this composite based on non-functionalized organic poly(ether-urethane) acrylate constituent. It could be also seen that volume distribution of TiO_2 aggregates formed in A7 composition is mainly random (Figure 6c–6d).

Thus, it can be concluded that typical hybrid polymer/titania composites using a swelling approach for hybrids synthesis were prepared and the samples obtained were studied in details. Carboxyl

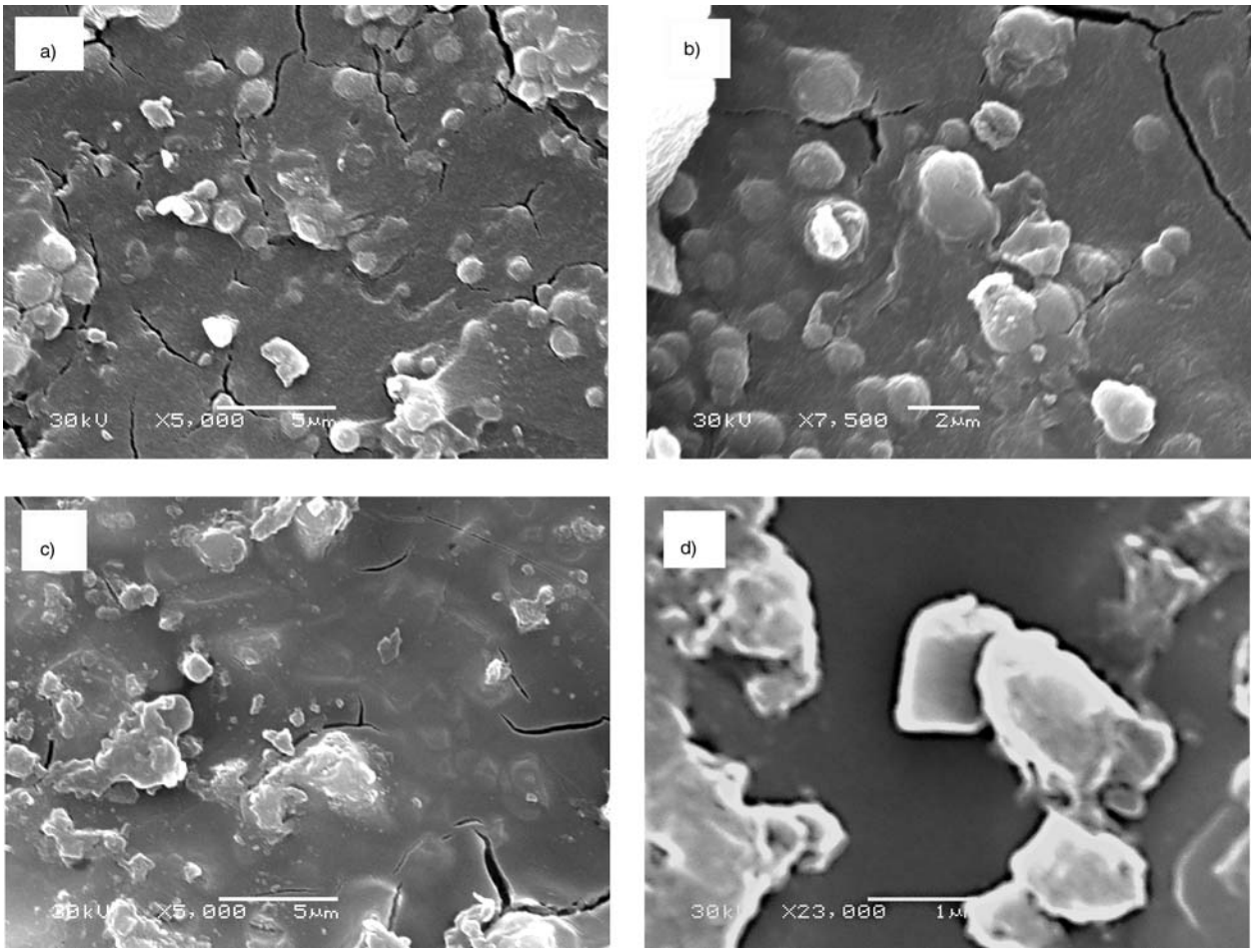

Figure 6. SEM microphotographs of hybrid composites prepared: (a, b) A4; (c, d) A7

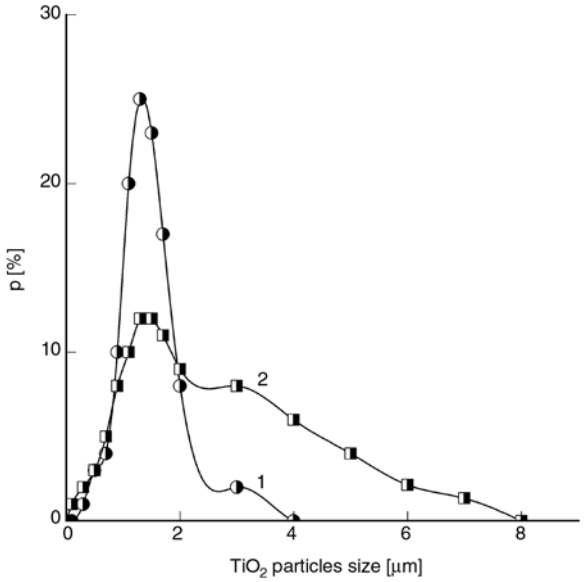

Figure 7. TiO_2 particles size distribution for microcomposites based on COOH-functionalized (1; A4 sample) and non-functionalized (2; A7 sample) networks

functionality of polymer chain playing a role of covalent bonding sites for inorganic $Ti(OiC_3H_7)_4$ component and organic PEUA chains has a significant influence on inorganic aggregates distribution in the film samples as well as on TiO_2 particles shape. Additionally, the samples with pendant COOH functional groups are characterized by narrow titania particles size distribution.

4. Conclusions

Summarizing of the experimental results presented in this work is allowed to conclude the follow. Synthesis of polymer/titania hybrid microcomposites via swelling of poly(ether-urethane)acrylate polymer network in concentrated solution of tetraisopropoxytitanate in 2-propanol or, that was found as more effective, 1,4-dioxane organic media were carried out. The composites prepared were characterized via IR, SAXS and SEM techniques, as well as their gravimetric parameters and swelling behavior in details. Gravimetric analysis shown that TiO_2 content in the most polymer composites prepared was found in the range of 3.8–30.8 wt%. SAXS

studies are evidenced of nano-sized (3.5–5 nm) heterogeneity of the polymer/TiO_2 composites prepared, that is typical for initial PEUA network. Using IR studies the formation of the hybrid microcomposites via chemical interactions of high reactive carboxylic groups of poly(ether-urethane) acrylate constituent and $Ti(O\textit{i}C_3H_7)_4$ precursor was clearly confirmed. Thus, the presence of functional (pendant COOH) groups in photo-cured polymer (PEUA) matrix exerts primary influence on a formation of the hybrids. Functionality of initial poly(ether-urethane)acrylate networks in relation with tetraalkoxytitanate precursor has a direct influence on both microscopic (TiO_2 particles size distribution, shape of the TiO_2 aggregates) and macroscopic (transparency) properties of the composites obtained. The ball-shaped dispersed titania particles (separated or aggregated) were mainly observed for composition based on carboxyl-functionalized poly(ether-urethane)acrylate network. Moreover, a relatively wide TiO_2 particles size distribution (in the range of 0.1–7.0 μm) for non-functionalized network and narrower TiO_2 particles size distribution (0.9–1.71 μm; main fraction) for COOH-functionalized polymer network were found for the microcomposites obtained.

Finally, the experimental data obtained in this work could be used for elaboration of high-loaded transparent or semitransparent TiO_2-filled hybrid polymer materials for multipurpose optical uses or advanced sealants.

References

[1] Armelao L., Barreca D., Bottaro G., Gasparotto A., Gross S., Maragno C., Tondello E.: Recent trends on nanocomposites based on Cu, Ag and Au clusters: A closer look. Coordination Chemistry Reviews, **250**, 1294–1314 (2006).

[2] Li W., Jia Q. X., Wang H-L.: Facile synthesis of metal nanoparticles using conducting polymer colloids. Polymer, **47**, 23–26 (2006).

[3] García-Gutiérrez M. C., Nogales A., Rueda D. R., Domingo C., García-Ramos J. V., Broza G., Roslaniec Z., Schulte K., Davies R. J., Ezquerra T. A.: Templating of crystallization and shear-induced self-assembly of single-wall carbon nanotubes in a polymer-nanocomposite. Polymer, **47**, 341–345 (2006).

[4] Peeterbroeck S., Alexandre M., Jerome R., Dubois P.: Poly(ethylene-*co*-vinyl acetate)/clay nanocomposites: Effect of clay nature and organic modifiers on morphology, mechanical and thermal properties. Polymer Degradation and Stability, **90**, 288–294 (2005).

[5] Dangtungee R., Yun J., Supaphol P.: Melt rheology and extrudate swell of calcium carbonate nanoparticle-filled isotactic polypropylene. Polymer Testing, **24**, 2–11 (2005).

[6] Wu L., Chen P., Zhang J., He J.: Inhibited transesterification and enhanced fibrillation of TLCP by nano-SiO_2 in polycarbonate matrix. Polymer, **47**, 448–456 (2006).

[7] Kudaibergenov S. E., Tatykhanova G. S., Arinov B. Zh., Kozhakhmetov S. K., Aseyev V. O.: Hybrid inorganic-organic nano- and microcomposites based on silica sols and synthetic polyelectrolytes. Express Polymer Letters, **2**, 101–110 (2008).

[8] Bauer F., Decker U., Ernst H., Findeisen M., Langguth H., Mehnert R., Sauerland V., Hinterwaldner R.: Functionalized inorganic/organic nanocomposites as new basic raw materials for adhesives and sealants. Part 2. International Journal of Adhesion and Adhesives, **26**, 567–570 (2006).

[9] Chang C-C., Chen W-C.: High-refractive-index thin films prepared from aminoalkoxysilane-capped pyromellitic dianhydride-titania hybrid materials. Journal of Polymer Science Part A: Polymer Chemistry, **39**, 3419–3427 (2001).

[10] Coutinho C. A., Gupta V. K.: Formation and properties of composites based on microgels of a responsive polymer and TiO_2 nanoparticles. Journal of Colloid and Interface Science, **315**, 116–122 (2007).

[11] Iketani K., Sun R-D., Toki M., Hirota K., Yamaguchi O.: Sol-gel-derived TiO_2/poly(dimethylsiloxane) hybrid films and their photocatalytic activities. Journal of Physics and Chemistry of Solids, **64**, 507–513 (2003).

[12] Xiong M., You B., Zhou S., Wu L.: Study on acrylic resin/titania organic-inorganic hybrid materials prepared by the sol-gel process. Polymer, **45**, 2967–2976 (2004).

[13] Syzdek J., Borkowska R., Perzyna K., Tarascon J. M., Wieczorek W.: Novel composite polymeric electrolytes with surface-modified inorganic fillers. Journal of Power Sources, **173**, 712–720 (2007).

[14] Katsaros G., Stergiopoulos T., Arabatzis I. M., Papadokostaki K. G., Falaras P.: A solvent-free composite polymer/inorganic oxide electrolyte for high efficiency solid-state dye-sensitized solar cells. Journal of Photochemistry and Photobiology A: Chemistry, **149**, 191–198 (2002).

[15] Chatzivasiloglou E., Stergiopoulos T., Spyrellis N., Falaras P.: Solid-state sensitized solar cells, using $[Ru(dcbpyH_2)_2Cl_2]\cdot 2H_2O$ as the dye and PEO/titania/I^-/I_3^- as the redox electrolyte. Journal of Materials Processing Technology, **161**, 234–240 (2005).

[16] Hattori H.: Two-step assembly technique for preparation of polymer-particle composite films. Thin Solid Films, **385**, 302–306 (2001).

[17] Chau J. L. H., Lin Y-M., Li A-K., Su W-F., Chang K-S., Hsu S. L-C., Li T-L.: Transparent high refractive index nanocomposite thin films. Materials Letters, **61**, 2908–2910 (2007).

[18] Kizilkaya C., Karataş S., Kayaman-Apohan N., Güngör A.: Preparation and characterization of sol-gel derived UV-curable organo-silica-titania hybrid coatings. Progress in Organic Coatings, **60**, 140–147 (2007).

[19] Luo X., Zha C., Luther-Davies B.: Preparation and optical properties of titania-doped hybrid polymer via anhydrous sol-gel process. Journal of Non-Crystalline Solids, **351**, 29–34 (2005).

[20] Naylor S., Bras W., Derbyshire G., Mant G. R., Bogg D., Ryan A. J.: Simultaneous time-resolved synchrotron X-ray scattering studies on block copoly(ether-urethane) phase behaviour. Nuclear Instruments and Methods in Physics Research, Section B: Beam Interactions, **97**, 253–256 (1995).

[21] Ferrer G. G., Pradas M. M., Ribelles J. L. G.: Thermodynamics of water sorption in acrylic homonetworks and IPNs. Die Makromolekulare Chemie, Macromolecular Symposia, **200**, 217–225 (2003).

[22] Feld R., Cowe P. L.: The organic chemistry of titanium. Butterworths, London (1965).

[23] Deshpande S. B., Potdar H. S., Khollam Y. B., Patil K. R., Pasricha R., Jacob N. E.: Room temperature synthesis of mesoporous aggregates of anatase TiO_2 nanoparticles. Materials Chemistry and Physics, **97**, 207–212 (2006).

[24] Kratky O., Pilz I., Schmitz P. J.: Absolute intensity measurement of small-angle X-ray scattering by means of a standard sample. Journal of Colloid and Interface Science, **21**, 24–34 (1966).

[25] Schmidt P. W., Hight R. J.: Slit height corrections in small angle X-ray scattering. Acta Crystallographica, **13**, 480–483 (1960).

[26] Perret R., Ruland W.: Eine verbesserte Auswertungsmethode fur die Röntgenkleine-winkelstreuung von Hochpolymeren. Kolloid-Zeitschrift und Zeitschrift für Polymere, **247**, 835–843 (1971).

[27] Guinier A., Fourner G.: Small angle scattering of X-rays. John Wiley and Sons, New York (1955).

[28] Tsai Y-M., Yu T-L., Tseng Y-H.: Physical properties of crosslinked polyurethane. Polymer International, **47**, 445–450 (1998).

[29] Chen K. S., Yu T. L., Tseng Y. H.: Effect of polyester zigzag structure on the phase segregation of polyester-based polyurethanes. Journal of Polymer Science, Part A: Polymer Chemistry, **37**, 2095–2104 (1999).

[30] Kartini I., Meredith P., Diniz da Costa J. C., Lu G. Q.: A novel route to the synthesis of mesoporous titania with full anatase nanocrystalline domains. Journal of Sol-Gel Science and Technology, **31**, 185–189 (2004).